CFD MODELLING OF AIR FLOW AND HEAT TRANSFER IN A VENTILATED CARTON

QIAN ZOU

1998

CFD MODELLING OF AIR FLOW AND HEAT TRANSFER IN A VENTILATED CARTON

A thesis presented in partial fulfilment of the requirements for the Degree of
Master of Applied Science in Agricultural Engineering
at Massey University

Qian Zou

1998

ABSTRACT

Forced-air cooling is widely adopted for cooling fresh produce in ventilated packages. Air distribution inside the package is therefore an important factor for efficient cooling, since the heat transfer between product and air is largely affected by air motions. Computational fluid dynamics (CFD) provides a sophisticated but economic tool for modelling air flow.

A CFD-based mathematical model was developed to simulate air flow patterns in a ventilated apple carton during precooling. The model took account of both laminar and turbulent situations. In the model, air mass, momentum and energy conservation, as well as energy conservation of apples and packaging materials were described by a set of partial differential equations (PDEs) plus boundary conditions. For the turbulent flow a Lam and Bremhorst Low-Reynolds-number k-ε model was introduced to calculate local turbulent eddy viscosity.

Two modelling strategies were adopted. In the first approach, the air flow was assumed to be steady-state while the buoyancy force due to natural convention was neglected. Steady-state Navier-Stokes equations were solved first, and the outputs of fluid velocity were then used as input data to solve energy equations. For the second approach, all transport equations were solved simultaneously with consideration of the effect of natural convection on air flow patterns. All together, three air flow scenarios were considered: steady-state laminar flow, steady-state turbulent flow, and unsteady-state laminar flow.

The CFD package PHOENICS (CHAM, UK Ltd) was used to solve the set of PDEs. The curvilinear Body-Fitted Coordinates (BFC) grid system was used for mesh generation. The entire grid system had 19964 cells. Five sets of PHOENICS codes were written for the three different flow situations. An additional PHOENICS programme was also used to calculate the heat transfer coefficients on the carton external surfaces. It took much longer time to reach convergence for unsteady-state laminar flow (91 hours) than for steady-state laminar flow (9-14 hours).

The predicted flow patterns and temperature profiles were very similar for steady-state laminar and turbulent flows under 0.5 m/s inlet velocity. By comparing predictions for steady-state and unsteady-state laminar flows, effects of natural convection were considered negligible in unsteady-state laminar flow. Thus it was reasonable to adopt the programme for steady-state laminar flow instead of unsteady-state laminar flow because of much less computing time in solving steady-state flow.

A trial of apple precooling was conducted in which temperature in the centres of apples in various positions were measured. Good agreement between model predictions and experimental data was obtained in most locations, but fairly large errors were found in the apples near carton inlets and outlets. Further work is required to refine the model and to validate air temperature and velocity predictions.

ACKNOWLEDGEMENTS

I would like to thank my chief supervisor, Dr. Linus U. Opara (Institute of Technology and Engineering) and my co-supervisor, Professor Robert McKibbin (Institute of Fundamental Science), and Associate Professor Cliff Studman (Institute of Technology and Engineering) for their advice and assistance during the course of this project.

I would also like to express my appreciation to all the technical staff (former Agricultural Engineering Department), especially Mr Gerard Harrigan and Mr Leo Bolter who assisted with much of the experimental work.

I would like to acknowledge the following persons for their help and advice: Mr Yun Lu (graduate student, Institute of Technology and Engineering), Mr Phil Etheridge (Institute of Fundamental Science) and Mr David Tanner (PhD student, Department of Food Technology).

TABLE OF CONTENTS

LIST OF TABLES

LIST OF FIGURE

CHAPTER 1: INTRODUCTION

The fresh fruit industries make significant contributions to the New Zealand economy. For instance, in the last decade there has been a rapid growth in horticultural exports from New Zealand, and fresh fruit export has been a major contributor to this development. Fruit export earnings are forecasted to more than double between 1992 and the year 2000 (The Enterprise New Zealand Trust, 1993). Apple is one of the most important fresh food commodities in New Zealand, which along with Kiwifruit have led the growth in fruit exports. In 1996 a total of 18 million cartons of class I and II apples and pears was exported, an increase of 7% on the previous year. The total revenue from fresh pipfruit (mainly apples) export was over NZ$ 631.6 million (NZAPMB, 1996).

Effective control of environmental factors is essential to maintain product quality and to prolong the shell life. These factors include temperature, vapour pressure deficit, relative humidity, and atmospheric composition. Temperature has pronounced effects on the metabolic rate of harvested crops. Their ripening-related processes, e.g. respiration and ethylene production, could be accelerated by increased environmental temperature. The length of time for which crops can be kept in sound conditions usually varies inversely with temperature (Kays, 1993). Good temperature management depends on achieving good contact between the product and the external environment. The removal of field heat from produce prior to transportation and marketing has long been recognised as a crucial step in postharvest temperature management. The term 'precooling' is commonly used to describe this rapid cooling operation.

Packaging system can significantly affect the environment around products. The successful development of a package is based on the requirements of the product within the frame work of the handling and marketing system. The optimal package is inexpensive, recyclable, adaptable for high volume; protects the commodity from mechanical damages and excessive water loss; and facilitates both the precooling and the maintenance of low storage temperature. A package needs to be carefully evaluated before implementation to ensure that product quality is maintained throughout storage and the entire handling system. Ventilated packaging has been adopted by New Zealand fresh fruit industries for a

long time. Both ENZAFruit (the marketing arm of the New Zealand Apple and Pear Marketing Board, NZAPMB) and Zespris International (Kiwifruit marketing) utilise a range of ventilated cartons for fruit export.

Forced-air cooling is the most widely adaptable method for the cooling of product in ventilated containers. The system creates a slight pressure gradient to force air through container vents, achieving rapid cooling through the intimate contact between cold air and warm product. Air distribution inside the package is therefore an important factor for efficient cooling of fruit, since the heat transfer between product and cooling medium (air) is largely affected by air motions. Air flow pattern plays a crucial role in product weight loss due to its influence on water vapour mass transfer between fruit and air. Other important quality-related factors, such as the concentrations of gases (oxygen, nitrogen, carbon dioxide, ethylene, etc.) in the storage atmosphere and inside produce, are also affected by air movement around produce. The understanding of airflow patterns is therefore essential for efficient design of fruit packages and operation of coolstores.

The experimental study of air flow is usually considered expensive, time-consuming and situation-specific. It may be difficult to achieve complete understanding of the phenomena behind a large amount of experimental data. Mathematical modelling is cost-effective to predict the air flow patterns inside packages, and to further assess the effects of the package on the product cooling process. The mathematical model should be capable of simulating air momentum transfer, heat and mass transfer within and between product, packaging materials and air.

Computational fluid dynamics (CFD) provides a sophisticated but economic tool for modelling air flow. CFD employs numerical methods to solve fundamental fluid transport equations which are derived from the laws of conservation of mass, momentum and energy. The increasing computing capacity of modern computers and the decreasing cost of software have made the application of CFD modelling more and more popular. The development and availability of CFD software have therefore enabled researchers to solve flow problems with moderate understanding of the detailed mathematical solution procedures. Current application of CFD in agricultural and food engineering research is

limited, but the potentials are considerable (Opara and Zou, 1998). The next chapter reviews the concepts of CFD and discusses current applications in modelling air flows in a range of areas.

CHAPTER 2: LITERATURE REVIEW

During the last couple of decades, there has been a rapid increase in computer applications in the study of fresh food packaging and storage. Increased computational power means that analyses for research and design purposes can be much more detailed than in the past if well-established models are available. Mathematical modelling provides a very economical and handy tool for the design of packaging and coolstores for fresh produce. The important physical phenomena which were investigated in this project included heat transfer within and between fruit, packaging materials and air flow, and momentum transfer of air flow. Thus, the review will focus on the mathematical modelling of air flows and heat transfer processes which take place in the forced-air cooling of fresh produce. Since velocity of air flow used for cooling is relatively low (Mach number[1] $<<1$), the modelling of air flow in high-Mach-number ranges, such as in the area of aerospace, was excluded. Four classes of relevant literature were reviewed. The first is the literature on general modelling methodology; the second is basic principles of computational fluid dynamics; the third is mathematical modelling of air flow; the fourth is modelling of heat transfer during produce cooling.

2.1 MODELLING METHODOLOGY

Mathematical equations which simulate real world situations are called models, since they behave in a manner analogous to the actual situations (Harper & Wanninger, 1969). A mathematical model of a process was also defined as 'a system of equations whose solution, given specified input data, is representative of the response of the process to a corresponding set of inputs' (Levine, 1997). Mathematical models usually exhibit concise, quantitative, and descriptive relationships between variables and are powerful tools for effective descriptions of processes. Due to its simplicity in expression, modelling helps users to better understand physical phenomena and to find universal rules hidden behind them. Application of mathematical models reduces the scope and cost of experimentation, as modelling allows more alternatives to be considered which may be difficult, or expensive to test.

---

[1]Mach Number = Fluid velocity/Local speed of sound.

2.1.1 Modelling Procedure

The starting steps in a modelling process are to examine the real world system to be modelled, and to identify the problems to be solved. These would enable the modeller to decide on the objectives of modelling, the required accuracy, and the type and size of computer envisaged (Touber, 1984). Cleland (1990) introduced a general system for equation development (Figure 2.1), suitable for modelling in refrigeration systems.

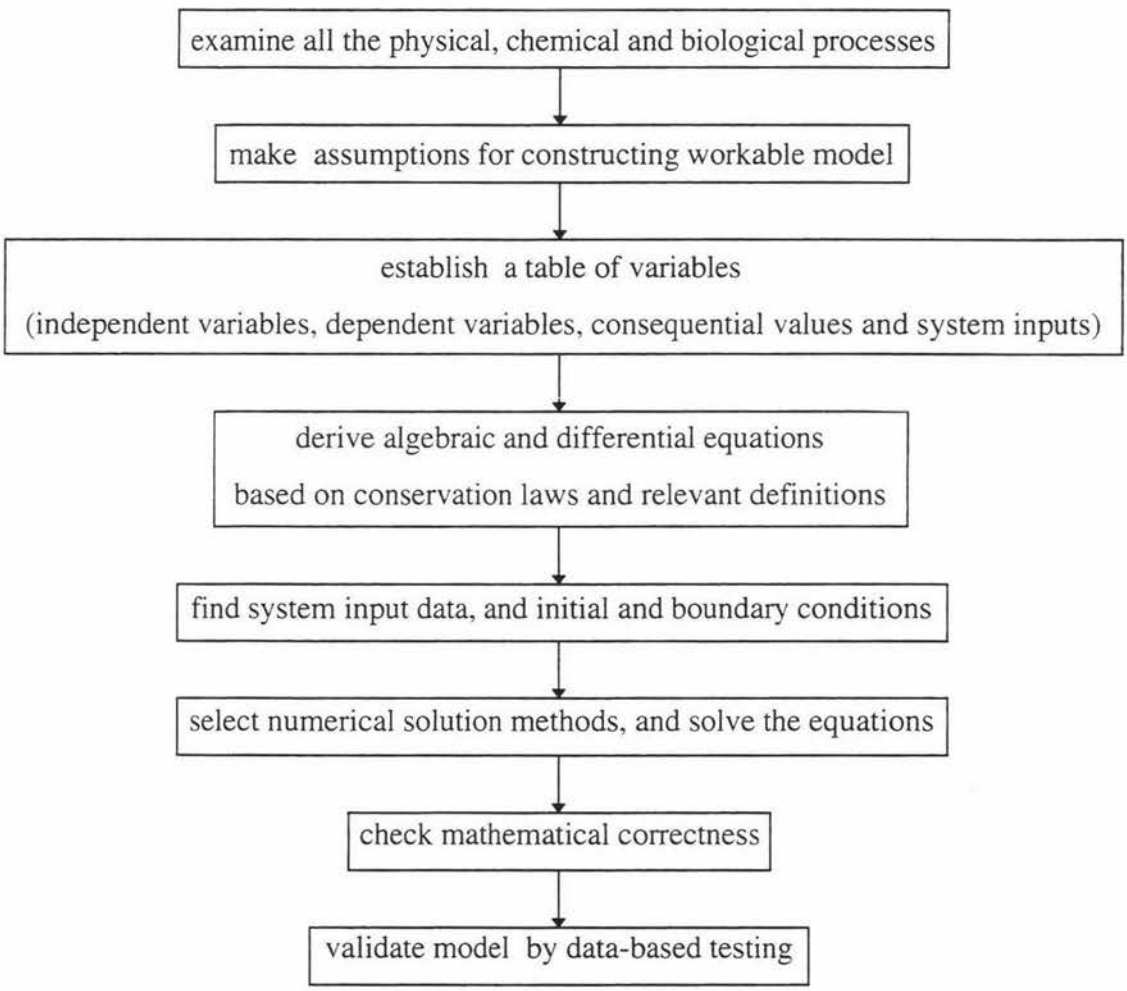

Figure 2.1 Modelling procedure suitable in the area of refrigeration

2.1.2 Types of Models

Two major types of models used in refrigeration and food engineering are mechanistic and empirical models. The mechanistic models, also called deductive models or white box

models, are theoretically based and derived analytically by making use of a series of progressively more specific concepts such as laws, structures and parameters. The most important laws include the principles of conservation of mass, energy and momentum. By using equations suggested by applicable mechanisms it is possible to get a good insight into the true factors affecting a process. Results outside the regions of operation may be predicted by a theoretical model. Problems with forming theoretically based models can arise. The theory may be incomplete, and many mechanisms may occur simultaneously, making it hard to define the interrelationships. Mathematical complexity of some models may cause difficulties in computation (Harper & Winninger, 1970a). These problems make it necessary to introduce empirical methods.

For empirical (inductive or black box) models, the essential steps are to find a form of mathematical relation for output variables as functions of input variables, and to estimate or determine the numerical values of the parameters appearing in this relationship (Touber, 1984). Depending on data it may be best to use empirical equations which may contain linear, quadratic, exponential, or other types of mathematical forms to obtain reasonable fit. The fitted equations may be used for interpolation within the region of experimental data if the data gathered are consistent. However empirical equations should not be extrapolated. Most practically used models are the combinations of empirical and mechanistic ones. For instance, pertinent coefficients in theoretical equations are often estimated by experimental data. The deductive models may be applied to predict performance of alternative systems, whereas inductive models are generally only suitable for one or two systems under the certain range of conditions. For this reason, it is often desirable to carry deduction as far as possible and rely on system observations only where absolutely necessary (Touber, 1984; Amos, 1995).

2.1.3 Time Discretisation

According to the variation of the modelled system with time, models can be classified as steady-state and dynamic (unsteady-state).

2.1.3.1 Steady-state model

Steady-state models are suitable for modelling systems whose major parameters do not change with time. Steady-state models are also used to assess the performance of a system under a set of different operating conditions. For example, the steady-state approach is applied to calculate typical heat loads under the worst environmental conditions for the design and optimisation of refrigeration systems (Touber, 1984). The steady-state modelling may be applied to describe time-average behaviour of a transient system, while heat and mass accumulation in the system is negligible. Steady-state models generally demand less computational time and a small amount of input data, as the time-variability in system parameters is not considered.

2.1.3.2 Dynamic models

Dynamic models are applied to assess how the time-variable effects, such as heat load, environmental conditions and start-up transients, influence normal system operation; accordingly advanced control strategy or detailed controller may be developed (Cleland & Cleland, 1989). Dynamic models are usually closer to real word, but require more detailed data and more computational time. Consequently they are more complex than steady-state models (Amos,1995). Because of rapid increase in computational capacity of modern computers, dynamic modelling is getting more and more popular.

2.1.4 Space Discretisation

Based on the approaches for modelling positional variability of conditions, models are divided into zoned and fully distributed models.

2.1.4.1 Zoned models

In zoned models, the space to be modelled is divided into several zones. If occupied by fluid, the fluid in each zone is assumed to be perfectly mixed; if occupied by solid, the position-variability within each zone is also neglected. Thus, for each zone an ordinary

differential equation is adequate for each variable as the conditions within the zone are assumed as uniform. Movement of fluid flow may be defined by a plug-flow pathway; the positions of zones are arranged along the flow pathway through the system in a sequential fashion (Amos,1995). Only temperature and fluid concentration are solved in zoned models; fluid velocity is previously defined, possibly using experimental data, instead of being solved through momentum conversation. A single-zoned model is the simplest case in which the whole calculation region is treated as uniform.

2.1.4.2 Fully distributed models

Fully distributed models are also called fluid dynamic models which use partial differential equations (PDEs) to formulate the full position-variability. These PDEs describe heat, mass and momentum conservation within the considered region. This approach is usually able to simulate the real world more accurately than the zoned models, since much less assumptions are needed to develop a fully distributed model formed with fundamental transport equations. The space is discretised by a grid system which is dependent on numerical means applied to solve the PDEs. Finite-difference and finite-volume methods are the most commonly used numerical tools. Fully distributed modelling requires much larger computer memory and computational time than zoned modelling. In recent years there has been increased application of the fully distributed approach mainly due to increased computational capacity and decreased cost. In addition to specific problem programmes, many generalised codes are also available.

2.1.5 Modelling Complexity

Depending on the purpose of model, the appropriate level of model complexity is a compromise between cost and accuracy. To obtain reasonably accurate predictions, a model must take account of all important physical processes. However, if too many details are incorporated, a model may be too complicated or costly to be solved, or the required input data may be too much and too expensive to be measured. It is thus inefficient to use a more detailed model than is necessary (Cleland, 1990; Amos, 1995). The level of model complexity is associated with time and space discretisation. As already mentioned, the

finer the time and space discretisation, the larger the number of variables is considered, and the more complex will be the overall model obtained.

2.2 PRINCIPLES OF COMPUTATIONAL FLUID DYNAMICS

Computational fluid dynamics (CFD) modelling is the process of representing a fluid flow problem by mathematical equations based on the fundamental laws of physics, and then solving those equations using computer to predict the variation of the relevant parameters within the flow field (Jones & Whittle, 1992). The origins of CFD can be found in automotive, aerospace and nuclear industries (Fletcher, 1988), and the technique has been applied in a wide range of areas such as food processing (Scott and Richardson, 1997) and environmental analysis (Jones and Whittle, 1992). The use of CFD in research and solution of industrial problems involves three main steps: the definition of problems, its solution, and analysis of the results. In the definition of problems, three discrete elements have to be taken into account. The first is derivation of the transport equations that describe fluid flow. The second is geometrical representation of the system being studied. The final component is the numerical procedure used to solve the transport equations in the geometry of interest (Scott & Richardson, 1997).

2.2.1 Fundamental Fluid Transport Equations

A knowledge of the fundamental equations of fluid dynamics and the characteristics of the transport phenomena is required in order to develop a computer-based mathematical model of fluid flow. These important fluid transport mechanisms are reviewed in the following sections.

2.2.1.1 General transport equations

The general equations directly related to fluid velocity and pressure are the Navier-Stokes equations which are derived form conservation of fluid momentum, and the continuity equation which represents the conservation of mass. By solving these equations the fluid velocity can be predicted. When temperature prediction is necessary, an equation for the

conservation of energy has to be solved. If an additional variable, for instance, water vapour concentration in air, is required to be calculated, the solution of an additional equation must be obtained for this variable (Peyret & Taylor, 1983). All the conservation equations, also known as field equations, represent the variation of solution variables in space and time. These basic equations for ideal gases and liquids are presented as follows (Yuan, 1967):

(a) Continuity equations (mass conservation equation)

$$\frac{\partial \rho}{\partial t} + \sum_{i=1}^{3} \frac{\partial (\rho u_i)}{\partial x_i} = 0 \qquad (2.1)$$

Where:

t	=	time (s).
ρ	=	density ($kg \cdot m^{-3}$).
i	=	index of axes in Cartesian coordinates.
x_i	=	spatial positions in Cartesian coordinates (m).
u_i	=	component of velocity in x_i direction ($m \cdot s^{-1}$).

(b) Navier-Stokes equations (momentum conservation equations)

$$\frac{\partial (\rho u_i)}{\partial t} + \sum_{j=1}^{3} \frac{\partial (\rho u_j u_i)}{\partial x_j} - \sum_{j=1}^{3} \frac{\partial}{\partial x_j} (\mu \frac{\partial u_i}{\partial x_j}) = X_i - \frac{\partial p}{\partial x_i} \qquad (2.2)$$

Where:

x_j	=	spatial positions in Cartesian coordinates (m).
u_j	=	component of velocity in x_j direction ($m \cdot s^{-1}$).
X_i	=	components of body force per unit mass along x_i direction ($N \cdot m^{-3}$).
p	=	pressure ($N \cdot m^{-2}$).
μ	=	dynamic viscosity ($N \cdot s \cdot m^{-2}$).

(c) Equation for energy conservation

$$C_p \frac{\partial(\rho T)}{\partial t} + \sum_{j=1}^{3} C_P \frac{\partial(\rho u_j T)}{\partial x_j} - \sum_{j=1}^{3} \frac{\partial}{\partial x_j}(K \frac{\partial T}{\partial x_j}) = S_E \qquad (2.3)$$

Where:

T	=	temperature (K).
C_p	=	specific heat at constant pressure ($J \cdot kg^{-1} \cdot K^{-1}$).
K	=	thermal conductivity ($W \cdot m^{-1} \cdot K^{-1}$).
S_E	=	source term of energy equations ($W \cdot m^{-3}$).

2.2.1.2 Modelling turbulent flow

Flow can be described as being either laminar or turbulent, or transitional. Laminar flow is characterised by a smooth progression of particles of fluid along with main convection flow. At the onset of transition this smooth flow begins to break up and to fluctuate, and eddies start to develop. While turbulence occurs an apparently random fluctuation of fluid movement develops which becomes superimposed on the mean flow (Tenneks & Lumley, 1973).

In principle no special treatments for turbulent flow are needed, for the Navier-Stokes equations apply equally to a turbulent motion as well as to a laminar motion. However, as the turbulent flow is unsteady, and its length-scales range from the dimensions of fluid field to small eddies responsible for the decay of turbulence (typically about 0.1 mm), a huge amount of computational time and memory is needed for a direct simulation (DS) which has to resolve all relevant scales. The accurate numerical representation of these tiny fluctuations may need millions of cells and very substantial CPU (Central Processing Unit) time on supercomputers even for problems with very small characteristic length (Launder & Spalding, 1972). For this reason, DS is restricted to very small and simple flows which are studied due to theoretical interest. It is likely to be many years before DS approach can be adopted to solve real engineering problems (Collins & Ciofalo, 1991).

A method which retains many features of DS, but requires less computational capacity, is called Large-Eddy Simulation (LES). This method involves the solution of 3-D time-dependent Navier-Stokes equations which formulate the large-scale anisotropic flow, while using a sub-grid model for the statistics of the small-scale motion. By introducing a space-filtering procedure, the instantaneous field of solved variable (velocity or pressure or temperature) can be decomposed into a filtered field which is directly resolved, and a small-scale residual fluctuation which is treated by the sub-grid model (Peyret & Taylor, 1983). The large-scale eddies determine the characteristics of an individual flow, but they are hard to model in any universal way. Using LES, the large eddies are simulated directly, and so no universal model is needed for them. Since small-scale turbulence is much more universal in character, and it has little effect on the large-scale properties of the flow, the small eddies can be modelled more easily. LES is largely free from arbitrary closure assumptions, and has promise as a universal method for predicting turbulent flows. However, the applications of LES to practical problems have been very limited because of its prohibitive expense at high-Reynolds-number ranges and the difficulties in specifying initial and boundary conditions (Collins & Ciofalo, 1991).

For applications of practical interest, the most common approach to turbulent flow prediction is still based on the time-averaging transport equations associated with Osborne Reynolds (Rodi, 1979; Yuan, 1967). All instantaneous fields are decomposed into time-average and fluctuating components:

$$u_i = \overline{u_i} + u_i' \tag{2.4}$$

$$p = \overline{p} + p' \tag{2.5}$$

$$T = \overline{T} + T \tag{2.6}$$

Where:

$\overline{u_i}$ = mean value of velocity component u_i ($m \cdot s^{-1}$).

u_i' = turbulent fluctuation of velocity components u_i($m \cdot s^{-1}$).

$\overline{p}$ = mean value of pressure ($N \cdot m^{-2}$).

p' = turbulent fluctuation of pressure ($N \cdot m^{-2}$).

$\overline{T}$ = mean value of temperature (K).

T' = turbulent fluctuation of temperature (K).

Substituting above equations into equations (2.1)-(2.3), and neglecting the fluctuation in fluid density, the time-average flow and energy equations were obtained (Yuan, 1967; Rodi, 1979):

$$\frac{\partial \rho}{\partial t} + \sum_{i=1}^{3} \frac{\partial (\rho \overline{u_i})}{\partial x_i} = 0 \tag{2.7}$$

$$\rho \frac{\partial \overline{u_i}}{\partial t} + \sum_{j=1}^{3} \rho \overline{u}_j \frac{\partial \overline{u_i}}{\partial x_j} - \sum_{j=1}^{3} \frac{\partial}{\partial x_j} (\mu \frac{\partial \overline{u_i}}{\partial x_j} - \rho \overline{u_i' u_j'}) = \overline{X}_i - \frac{\partial \overline{p}}{\partial x_i} \tag{2.8}$$

$$C_p \frac{\partial (\rho \overline{T})}{\partial t} + \sum_{j=1}^{3} C_P \frac{\partial (\rho \overline{u}_j \overline{T})}{\partial x_j} - \sum_{j=1}^{3} \frac{\partial}{\partial x_j} (K \frac{\partial \overline{T}}{\partial x_j} - \rho C_P \overline{T' u'_j}) = \overline{S}_E \tag{2.9}$$

Where:

$\overline{S_E}$ = time-average source term of energy equations ($W \cdot m^{-3}$).

Time-average equations are very similar to the original flow equations, but have the averaged quantities as unknowns, and the double correlated fluctuation quantities in diffusion terms, $-\rho \overline{u_i' u_j'}$ and $-\rho C_P \overline{T' u'_j}$, which are called Reynolds stresses and fluxes. If the Reynolds terms can be expressed as functions of the mean fields, turbulence modelling then becomes a closure problem. By the methods of handling the Reynolds terms, turbulence models are classified as eddy-viscosity and Reynolds-stress models (CHAM, 1995; Rodi, 1979).

The eddy-viscosity models employ the eddy, or turbulent, viscosity concept to determine the Reynolds stresses from:

$$-\rho\overline{u_i'u_j'} = \mu_t\left(\frac{\partial\overline{u}_i}{\partial x_j} + \frac{\partial\overline{u}_j}{\partial x_i}\right) - \frac{2}{3}\rho k\delta_{ij} \tag{2.10}$$

Where:

μ_t = turbulent eddy viscosity ($N\cdot s\cdot m^{-2}$).

k = turbulent kinetic energy ($J\cdot kg^{-1}$).

δ_{ij} = Kronecker delta (δ_{ij} =1 if i=j, and 0 otherwise).

Moreover, a turbulent diffusion coefficient, which is usually assumed to be proportional to eddy viscosity through turbulent Prandtl number, is used to relate the Reynolds fluxes to the average temperature field:

$$-\rho C_P\overline{T'u'_j} = \Gamma_t\frac{\partial\overline{T}}{\partial x_j} \tag{2.11}$$

$$\mathrm{Pr}_t = \frac{C_p\mu_t}{\Gamma_t} \tag{2.12}$$

Where:

Γ_t = turbulent diffusion coefficient ($W\cdot m^{-1}\cdot K^{-1}$).

Pr_t = turbulent Prandtl number.

Eddy viscosity may be calculated from several turbulence quantities, such as the Prandtl 'mixing length' l (microscale of turbulence), the turbulent kinetic energy k and its dissipation rate ε. Based on the methods used to obtain the eddy viscosity, the eddy-viscosity models are categorised as follow.

(a) Zero-equation models

Zero-equation models use only the transport equations for the mean flow. Thus, no transport equations are employed for turbulence quantities which somehow are algebraically prescribed throughout the flow field (Launder & Spalding, 1972; Rodi,

1979). The simplest turbulence model is the constant viscosity model which set the μ_t to a suitable value by the following formula (Launder & Spalding, 1972):

$$\mu_t = C\rho V_s L_s \tag{2.13}$$

Where:

V_s = typical turbulence velocity scale ($m \cdot s^{-1}$).

L_s = typical turbulence length scale (m)

C = constant.

Constant viscosity model may only be used as a starting point for investigating convergence of numerical solutions. Another zero-equation model is Prandtl's mixing-length model which takes velocity scale to be the product of the mixing length l and the local mean-velocity gradient, and the length scale is prescribed empirically. The Prandtl's mixing-length model is only valid for boundary flow, and unsuitable for complex flows because of difficulties in estimating the distribution of the mixing length (CHAM, 1995; Launder & Spalding, 1972; Rodi, 1979).

(b) One-equation models

In one-equation models the Prandtl's mixing length l or turbulent energy dissipation rate ε is prescribed, while the turbulence kinetic energy k is computed by solving a transport equation:

$$\rho \frac{\partial k}{\partial t} + \sum_{j=1}^{3} \rho u_j \frac{\partial k}{\partial x_j} - \sum_{j=1}^{3} \frac{\partial}{\partial x_i}[(\mu + \frac{\mu_t}{\sigma_k})\frac{\partial k}{\partial x_j}] = \sum_{i=1}^{3}\sum_{j=1}^{3} \mu_t (\frac{\partial \overline{u}_i}{\partial x_j} + \frac{\partial \overline{u}_j}{\partial x_i})\frac{\partial \overline{u}_i}{\partial x_j} - \rho\varepsilon + S_k \tag{2.14}$$

Where:

σ_k = constant (σ_k=1.0).

S_k = buoyancy force production term in k equation ($J \cdot m^{-3} \cdot s^{-1}$).

Since the transport effect of the turbulent velocity scale is taken into account, the one-equation models are superior to the zero-equations when this transport is important. However, these models may be not suitable for complex flows as it is difficult to prescribe the length scale for complex flows (CHAM, 1995; Launder & Spalding, 1972; Rodi, 1979).

(c) Two-equation models

Except for the transport equation for k, two-equation models use another transport equation for a second turbulent property related to a turbulence length scale. The most popular two-equation model is the k-ε model, in which a transport equation for turbulence kinetic energy dissipation rate ε is employed in addition to equation (2.14).

$$\rho\frac{\partial \varepsilon}{\partial t}+\sum_{j=1}^{3}\rho u_j\frac{\partial \varepsilon}{\partial x_j}-\sum_{j=1}^{3}\frac{\partial}{\partial x_i}[(\mu+\frac{\mu_t}{\sigma_\varepsilon})\frac{\partial \varepsilon}{\partial x_j}]=\sum_{i=1}^{3}\sum_{j=1}^{3}\frac{C_1\mu_t\varepsilon}{k}(\frac{\partial \overline{u}_i}{\partial x_j}+\frac{\partial \overline{u}_j}{\partial x_i})\frac{\partial \overline{u}_i}{\partial x_j}-\frac{C_2\rho\varepsilon^2}{k}+S_\varepsilon \tag{2.15}$$

Where:

σ_ε = constant (σ_ε=1.3).

C_1 = constant (C_1=1.44).

C_2 = constant (C_2=1.92).

S_ε = buoyancy force production term in ε equation ($J\cdot m^{-3}\cdot s^{-2}$).

Two-equation models have been well documented by Launder and Spalding (1974). These models are the most widely used method for representing turbulence, because they usually present good balance between the requirements on computational capacity and modelling accuracy. However, their performance may not be acceptable in modelling certain flow situations such as re-attaching flows, flows with strong streamline curvature, transitional flows, and non-isotropic flows (Jones & Whettle, 1992).

The Reynolds-stress models, also called second-moment closure models, drop the concept of eddy viscosity, and directly relate the Reynolds stresses to mean flow variables. This class of models can be subdivided into two groups:

(a) Reynolds-stress-transport models

Reynolds-stress-transport models (RSM) represent a step much closer to the fundamental equations than eddy-viscosity models, as the Reynolds stresses are directly solved from transport equations. For a three-dimensional flow, six transport equations for Reynolds stresses and one for ε are added to the mean flow equations. The details about RSM have been well documented by Rodi (1979) and Leschziner (1990). The RSMs account for shear-stress sensitivity to anisotropy, and they behave better than eddy-viscosity models for complex strain field associated with curvature, rotation, swirl and buoyancy. The major disadvantage is the requirement for much larger computational capacity as five more PDEs have to be solved compared with the k-ε models. Stress models are also less computationally stable than eddy-viscosity models, particularly with higher-order discretization schemes (CHAM, 1995).

(b) Algebraic stress models

As a compromise, algebraic stress models (ASM) relate the individual Reynolds stresses to k and ε via algebraic equations, instead of solving separate transport equations. Therefore turbulence motion is modelled by transport equations for mean flow variables, k and ε, plus a group of algebraic equations. The transport of stresses is assumed to be proportional to that of turbulence kinetic energy k (Rodi, 1979; Collins & Ciofalo, 1991). Algebraic stress models have been applied successfully to represent the effect of body forces (buoyancy, swirl, rotation), but were considered unsuitable for flows too far removed from equilibrium (CHAM, 1995). The applications of ASM for industrial flows were reported to be at least as accurate as k-ε models and more accurate in many cases, but also result in an increase of computational time of between 50% and 150% (Jones and Whittle, 1992).

2.2.1.3 Boundary conditions

All transport phenomena of interest in agricultural and food processes may be described by the same set of equations. Differences in results stem from boundary conditions of the

problem. Since the boundary conditions are unique to a particular flow situation, these conditions should be accurately represented for achieving a reliable solution. The boundaries which are commonly encountered in practical flows are inlet, outlet and wall boundaries (Awbi, 1989).

Generally the longitudinal velocity V, temperature T, kinetic energy of turbulence k and the energy distribution rate ε can be assumed to distribute uniformly over the inlet boundary. Pressure is usually set to ensure a certain mass flow through the inlet. The other two velocity components are taken as zero. It is better to obtain the inlet conditions from experimental data than to use assumed values. For the outlet boundary the longitudinal velocity may be derived from mass conservation for the whole flow field, or may be set to keep the pressure to be fixed at a certain value, say, atmospheric pressure for some air flow situations. The exit temperature can be calculated from the energy conservation of the entire domain of interest while heat transfer across all boundaries is taken into account (Awbi, 1989; CHAM, 1995).

No-slip boundary condition is used to specify the fluid velocity on a wall, i.e., the fluid moves at the same velocity as the wall. If the turbulence models are used, special treatments are needed for modelling flow in the near-wall regions where laminar viscosity becomes more significant than turbulence viscosity. Therefore, turbulence models which are developed on the assumption of fully turbulent flow, have to be modified. One approach is to recast the transport equations for turbulence quantities so that they are also valid for the low-turbulence regions, and the near-wall layer is resolved with a fine computational grid. In the context of k-ε models, Jones and Launder (1972) firstly proposed a Low-Reynolds-number k-ε model, which was modified by several other authors such as Lam and Bremhorst (1981). Another method is to employ wall functions to describe the viscous region down to the wall while the standard high-Reynolds-number model is used. The wall functions specify the universal linear-logarithmic profiles of velocity and dimensionless length scalar from the wall, which are derived from the mixing length theory and experimental data. In this case, the grid has to be chosen so that the first near-wall point lies outside the viscous sublayer (Launder & Spalding, 1974).

2.2.2 Numerical Solution Methods

The transport equations are of partial differential form, and are highly non-linear, so they can not be solved analytically except in some very simple cases. Numerical methods have to be applied to discretise the PDEs into a set of algebraic equations in terms of space and time, which are then solved to find the values of the dependent variables in a finite number of locations over the calculation domain. The commonly used numerical approaches for engineering flows are finite element and finite difference methods. The more usual form of the finite difference methods is called finite volume approach. In both methods the equations are solved on a grid (also known as a mesh) which defines an element in the finite element method, or control volume in the finite volume method (Patankar, 1980). The solution accuracy and computational efficiency (computing time and required computer memory) are major criteria for choosing a numerical method.

2.2.2.1 Finite element method

The finite element method used in CFD has been well documented by Fletcher (1988a) and Peyret and Taylor (1983). In general a finite element method (FEM) divides the calculation domain into a number of non-overlapping segments. A finite number of points (called nodes) are used to refer to these segments. The solution of a PDE can be expressed approximately in terms of the nodal values and interpolation functions within the segments. Piecewise polynomials of relatively low orders or splines are used as the interpolation functions. The small segments with these associated nodes and interpolation functions are called the finite elements. A system of algebraic equations, called element equations, are derived from each element based either on a weighted-residual (Galerkin) or on a variational (Rayleigh-Ritz) approach.

Finite element method was reported to be more capable of handling complex geometry and high non-uniform grids, and to provide more accurate solution on a given mesh than the finite volume method. However, the finite element approach is significantly more intensive in computing requirements; and it can be cumbersome while applying high-order schemes or changing model input data (Collins & Ciofalo, 1991).

2.2.2.2 Finite volume method

The finite volume method (FVM) was firstly proposed by Patankar and Spalding (1972). The details about this method were introduced by Patankar (1980). In the FVM a computational field is divided into a number of non-overlapping control volumes (also known as cells) such that each control volume surrounds each grid point. The PDEs are integrated over each control volume, and the Gauss theorem is then invoked, and the resulting convective and diffusion fluxes across the volume's faces are approximated by the piece-wise profiles expressing the variation of dependent variables between the grid points. The discretisation equations obtained in this manner represent the conservation principle for the dependent variables over the control volume. The same algebraic equations can be derived by directly discretising the differential operators in the transport equations, that is the finite difference version (Patankar, 1980).

The FVM is far more popular than the finite element methods, mainly because its discretisation equations maintain a close link with the original PDEs, making it easier to carry out model changes and to evaluate the modelling results. The ability of the FVM in handling complex geometry has been improved by the introduction of sophisticated meshes such as body-fitted and structured grids.

2.2.2.3 Computational grids

Proper generation of meshes is essential for the application of CFD modelling. The important aspects of computational grid were well discussed by Jones and Whittle (1992). Small cells or elements and the resulting overall fine grid provide more details on the variation of the variables over a calculation domain, and also ensure greater accuracy of solution. Theoretically, grids should be fine enough to generate accurate results with an appropriate level of detail. However, computational costs would be prohibitive in order to generate so-called 'grid independent results', particularly for three-dimensional buoyant flows (Jones and Whittle, 1992). It is advisable to initially generate a relatively coarse grid to produce solution without too much computational efforts, then after gaining some confidence in modelling assumptions and the approach being taken, to refine the grid for

further improvement in resolution and accuracy. Fine grids should be applied in the areas where the solution variables have large space gradients, such as inlets, outlets and near-wall regions. Too coarse grids may lead to convergence difficulties and inaccuracy resulting from false diffusion, particularly when the local flow direction is inclined to the grid directions (Patankar, 1980; CHAM, 1995). The commonly used grids are: rectilinear (Cartesian), curvilinear (body-fitted coordinates), block-structured, and unstructured grids.

The cells in the rectilinear grid are formed by rectangles. The grid has a so-called I, J, K structure in which the location of each cell is specified by I, J, K notations in three grid-wise directions. While defining a grid, the cell aspect ratios have to be kept as close to unity as possible. Aspect ratios greater than about 5:1 could affect the rate of convergence. The rate of expansion of cell size between adjacent grid lines also should be limited for the sake of accuracy (Jones and Whittle, 1992). The advantages of the Cartesian grid include easy generation of grid and efficient calculation by the finite volume method. Its main disadvantage is the difficulty in representing irregularly shaped flow fields.

A curvilinear grid (BFC) can be thought of as a distorted Cartesian grid. Each cell retains six faces, and the cells originally in contact remain so. BFC cells are specified in terms of cell-corner coordinates in a Cartesian space. The BFC grids allow much large flexibility in handling geometrically complex calculation domains than the Cartesian grids, although greater CPU time and larger computer memory are required (Patankar, 1980; CHAM, 1995).

A block-structured grid is made up of a number of blocks, each of which is an individual BFC mesh. The block-structured grid can correct the badly distorted cells, and ensure satisfactory orthogonality to avoid the occurrence of severe false diffusion (Jones and Whittle, 1992). An unstrustured mesh may contain triangular elements, wedges as well as four- and six-sided cells. The unstructured meshes are previously applied in the finite-element methods. Newly developed algorithms may allow this type of meshes to be applied in the finite-volume formulation (Jones and Whittle, 1992).

2.2.3 Presentation and Verification of CFD Results

CFD results are usually examined in two ways. In traditional method, a data file provides all relevant information which includes the spatial co-ordinates defining the computational mesh and the values of solved variables (velocity components, temperature, pressure, concentrations) for each cell or element. For a large CFD problem, it is obviously inconvenient to interpret the results from a huge amount of data in the output file. The second method (often called post-processing) allows the user to visualise the calculated results. A post-processor is used to process the data in the output file and display them graphically on the computer screen. There are three commonly used graphical presentation methods: vector plot, contour plot and iso-surface plot (CHAM, 1995; Jones and Wittle, 1992; Scott and Richardson, 1997).

The validity of a CFD model has to assessed by comparison with experiment results. Two types of experiments are often conducted to verify CFD predictions. One is experimental flow visualisation which can qualitatively verify the flow patterns predicted by the CFD models. Methods for visualisation of air flow include smoke-tube, helium-bubble, tufts and interferometer approaches (Bradshaw, 1970; Goldstein, 1983; Mueller, 1983). The second type of experiments is to measure the values of variables in different positions of the flow field. The measured variables may be velocity, temperature, pressure, concentrations, turbulence quantities. Air velocity can be measured by pitot tube, chronophotograph, propeller and vane anemometer, thermal anemometer, ultrasonic anemometer, and laser Dopple anemometer (Bradshwa, 1970; Cheremisinoff and Cheremisinoff, 1988; Fingerson and Freymuth, 1983; Somerscales, 1981).

2.2.4 Commercial CFD Codes

A few general-purpose CFD codes are commercially available that provide solutions for a wide range of flow and heat transfer problems. The CFD codes are generally made up of three modules. Firstly, a pre-processor converts input programmes, which describe the problems and are written in high-level language, into FORTRAN statements; secondly, a solver discretises the flow transport equations and performs solution; finally, a post-

processor is used to display the results in easily visualised forms (Collins and Ciofalo, 1991). Some of these codes are listed in the Table 2.1. The main features of these codes were summarised in the Table 2.2. Originally all CFD codes had to be run in workstation and mainframe computer facilities due to the intensive requirement of computing capacity. Recent developments in PC technology have allowed some of the CFD codes to be applied in PC-based systems, although difficulties remain for the applications of PC in solving the flow problems in large and complex domains.

Table 2.1 Some general-purpose commercial CFD codes

CFD code	Solution method	Grid	Developer
TEACH	FD/FV	Structured	Imperial College of Science and Technology, UK
PHOENICS	FD/FV	Structured	CHAM Ltd, UK
FLOW3D	FD/FV	Structured	AEA Technology, Harwell,UK
STAR-CD	FD/FV	Unstructured	Computational Dynamics Ltd, UK
ASTEC	FD/FV	Unstructured	AEA Technology, Thurso, UK
FLUENT	FD/FV	Unstructured	CREARE Inc, USA
FEAT	FE	Unstructured	Berkeley Nuclear Laboratories, UK
FIDAP	FE	Unstructured	Fluid Dynamics International, USA

2.3 MODELLING AIR FLOWS IN CONTROLLED ENVIRONMENT

Traditionally, air flow patterns were studied mainly by using physical models due to computational costs of CFD modelling. The data measured from a physical model were thus used to justify a proposed air distribution method. Modifications to the model may be made to achieve the required conditions. If the physical models can not be constructed at full scale, reduced scale models have to be built with geometrical similarity. Experiments carried out in a model should have dynamic and thermal similarity if they are not applied to the full scale. This requires the equality of some dimensionless parameters, such as Reynolds number and Archimmedes number, between the physical models and their prototypes.

Table 2.2 Summary of the main types of fluid flow problems that general-purpose CFD codes can solve (Scott and Richardson, 1997).

Types of Flow	Modes of heat transfer	Types of materials	Co-ordinate systems
Steady-state or transient Viscous or inviscid Laminar and turbulent Compressible and incompressible Subsonic, ultrasonic or supersonic Two-phase (continuous or particles) Chemical reaction Combustion Swirling Non-Newtonian (inelastic)	Convection Conduction Radiation	Liquid Gas Solid (homogeneous or porous)	Cartesian Body-fitted Cylindrical Moving Rotating

Physical models are usually costly and time consuming, and similarity may not be possible to achieve under some situations. Nowadays, physical models are largely used to provide data for the validation of CFD-based models, or to find inputs for some simplified models. CFD has become a very powerful tool for studying air flows in a wide range of areas. In agricultural and food engineering areas, CFD models have been used to simulate the air flows in ventilated buildings, refrigerated stores, food processing machines etc.

2.3.1 Modelling Air Flow Patterns in Buildings

Considerable research has been carried out to model air flow fields in buildings using CFD-based programmes. Gosman, *et al* (1980) applied a finite volume method to solve the 3-D equations for air mass, momentum and energy conservation as well as two equations for turbulence quantities in the k-ε model. The effects of buoyancy were neglected in the model due to low Archimedes number of air movement in the ventilated room. Acceptable agreement was obtained when measured and predicted velocity profiles in the room and velocity decay in the air jet were compared. Timmons *et al* (1980) applied an inviscid two-dimensional model to simulate the air flow patterns in a slot-ventilated

livestock facility. The model used the equations in stream function and vorticity form, combining with semi-empirical relationships for vorticity distribution. The accuracy was considered acceptable except in the near-wall region where error was due to inviscid assumption.

Markatos and Malin (1982) developed a 2-D finite-difference procedure for predicting velocity and temperature distributions in enclosures containing a fire source. A heat source was used to represent the fire source. Additional terms were added to k and ε equations to prescribe the buoyant effects. The results were shown to be in reasonable agreement with experimental data. Markatos and Pericleous (1984) presented a computational method to obtain solutions of buoyancy-driven laminar and turbulent flows and heat transfer in a square cavity with differentially heated side walls. The k-ε model was used for the flow with Rayleigh numbers greater than 10^6. The results were compared with a published benchmark numerical solution, the agreement was generally good. Reinartz and Renz (1984) investigated the behaviour of a jet emerging from a radial pallet and resulting air flow in a rectangular room. A finite-volume scheme was applied to solve 2-D flow equations as well as the k-ε turbulence model. Acceptable accuracy of the numerical solution was obtained when compared with experimental data.

Choi *et al* (1988) used a standard k-ε turbulence model to predict two-dimensional isothermal air flow patterns in a slot-ventilated enclosure of simple geometry. A modified TEACH programme was employed to solve the model. Air distribution patterns, velocities, jet growth and attachment, and entrainment predictions were found to agree well with published data. This model was further extended to model a ventilated air space having an obstacle to flow (Choi *et al*, 1990). Sufficiently refined grid spacing was used in simulating corner eddy motion near solid boundaries. Comparison of predictions to the measured data showed that air distribution patterns were well predicted, and calculated air velocities were reasonably accurate.

Awbi (1989) described a finite-volume method to predict the air flow and heat transfer in a 2-D enclosure and the 3-D flow of a wall jet over surface-mounted obstacles. The CFD solution produced reasonably good predictions of the air velocity and temperature

distribution in a test room cooled by a ceiling jet. No experimental data were used to validate other predictions involving the heating and cooling of a room and flow of a wall jet over a obstacle. A low-Reynolds-number k-ε model was developed by Chen *et al* (1990) for the prediction of natural convection flow in cavities with Rayleigh number on the order of 10^{10}. The buoyancy was represented according to Boussinesq approximation; and the buoyancy production terms were added in k and ε equations. Predicted velocity and temperature profiles were in a rather good agreement with the measurements. The influence of the buoyancy production was found to be small on velocity and temperature profiles, but considerably large on the kinetic energy profiles.

Hoff *et al* (1992) applied a CFD model to investigate the effects of animal-generated buoyant forces on air temperature and speed distributions in a ceiling-slot, ventilated, swine grower facility. The model incorporated the Lam-Bremhorst turbulence model (LBLR) for low-Reynolds Number air flow typical of slot-ventilated, livestock facilities. Both numerical and experimental investigations were conducted using 1/5 scale-model facility. The model was able to predict air flow patterns adequately for Archmedes number Ar_c>40 and inlet jet momentum number J values < 0.00053. For Ar_c<40 and J values > 0.00053, the discrepancy between predicted and measured air flow patterns was attributed to variations in inlet flow development assumptions. This model was further evaluated by Hoff *et al* (1995). Overall, the LBLR model was found to adequately predict airspeed and temperature profiles, however shortcomings were indicated by comparisons of specific profiles. The model had a tendency to underpredict the ceiling detachment location for flows with Ar_c>40, and to overpredict the detachment location for flows with Ar_c below 40. The model also underpredicted the overall spread of inlet jet.

Hoff (1995) developed a simplified turbulence model for describing air flow in ceiling slot-ventilated enclosures. An effective viscosity was defined as a function of the inlet Reynolds Number Re_H and normalised vertical height from the floor. The effective viscosity was used to selectively augment the laminar viscosity in the Navier-Stokes equations. Predicted comparisons between the simplified and the LBLR models showed negligible differences for ventilation conditions with Re_H between 35,032 and 11,752. Liu *et al* (1996) numerically simulated a plane-free jet using the standard k-ε model and four

nonumiform grid patterns. Adequate grid solution was reached with five grid points in the inlet for the jet studied. The solution was in good agreement with the experimental results. A plane-wall jet was also simulated using five different grids and three k-ε models, which were the standard k-ε model (STD), Lam and Bremhorst low Reynolds number model (LB), and Lam and Bremhorst low Reynolds number model with wall functions (LBW). The LBW model was found better than the other two models. The LB model gave the worst performance for grids tested and STD model may not converge if all grid points were not in the fully turbulent region. Compared with published data, all three models predicted velocity profile and velocity decay well, but overpredicted the jet spread and entrainment ratio significantly.

Maghirang and Manbeck (1993) and Maghirang *et al* (1994) modelled transport of buoyant bubbles and 5 μm particles in slot-inlet ventilated airspace under isothermal and fully turbulent flow conditions. Air flow was modelled using the standard k-ε turbulence model. Particle transport was formulated using the equation of motion of particles. The model was solved by a CFD code FLUENT. Comparison between numerical solution and experimental results showed good agreement in velocity fields and bubble trajectories, fates, and residence times. No significant difference was found while comparing the numerically predicted fates, residence times, and concentration of the buoyant bubbles and 5 μm particles. Worley and Manbeck (1995) applied a similar approach to model airflow patterns and particle transport through a two-story stack layer facility with mild weather conditions. The model was validated by experimental results obtained from a 1/5 scale physical model.

Hoff and Bundy (1996) compared the LBLR model and a multi-zoned model in describing the distribution of carbon dioxide in a simulated swine grower pen. The multi-zoned model, initially developed by Liao and Fedds (1992), assumed three general air flow regions. Both the LBLR and multi-zoned models predicted similar trends in normalised CO_2 levels in the region immediately affected by the ventilating air jet. The multi-zoned required a prescribed airflow pattern and a detailed knowledge of entrainment ratio, consequently reduced the predictive ability of overall contaminant dispersion. Reynolds (1997) developed a model to predict mean concentrations of 1 μm diameter particles

within a ventilated airspace. Modelling was conducted in two steps. First, the statistical properties of the air flow were predicted using the k-ε turbulence model. The mean particle concentration fields were then calculated from independent trajectories of particles within the predicted air flow, which were simulated using a random flight model. The predicted locations of maximum particle concentrations and shape of the contours of constant particle concentrations were in accord with experimental results. However, the model did not accurately predict the absolute particle concentrations.

2.3.2 Modelling Air Flow Patterns in Refrigerated Spaces

The CFD-based models for air flow patterns in refrigerated spaces are still in development stage. Unlike an office or living room, a refrigerated space is almost fully occupied with produce and packaging, and the free space for the air circulation has a very complicated shape. Therefore, very fine and complex grids were usually needed to numerically simulate air motions in refrigerated spaces. Simplified assumptions had to be made to reduce the requirements in computing time and memory while the transport equations were solved.

Wang and Touber(1990) described a distributed dynamic model of a refrigerated room. The modelling was carried out in two steps. The first step was to model the flow pattern without considering any heat and mass transfer. As the air flow was treated as steady-state, the three-dimensional Navier-Stokes equation was decoupled from expression for energy and mass transfer. The air velocity and turbulence quantities in the k-ε model were solved by using a commercial CFD package PHOENICS, which employed the finite-volume method. The second step was to model the heat and mass transport based on the predicted flow pattern. Although such a strategy largely reduced the computational time, the prediction of the air flow pattern in the room still required 100 hours of computing on a Sun 3/60 workstation. The model was tested by experimental data, and satisfactory results were obtained.

Van Gerwen *et al.* (1991) used the PHOENICS package to simulate stationary 3-D air flow distribution in a carcass chiller. The carcass rows in the chiller were modelled as porous rows. The air velocity around a carcass, calculated by the CFD model, was used as

an input for heat and mass transfer equations on the surface of a thermal carcass model. Their model was also validated by measured data, and good agreement was found. Mariotti *et al* (1995) used a similar approach to model air distribution in a refrigerated room. The velocity field was firstly solved under steady state. Then with the obtained velocity distribution, the transient temperature field was solved. The solution procedure was based on the finite element method, which was claimed to provide the intrinsic flexibility to treat complex flow situations and not regular geometry conditions.

2.3.3 Modelling Air Flow Patterns in Other Agricultural Areas

Parsons (1991) developed a mathematical model for the gas flow in a bunker silo. The driving force was assumed to be the difference in density between the air outside and the carbon dioxide-rich gas inside the clamp. Darcy's law for fluid flow in a porous medium was used to calculate the gas flux. The model was solved using PHOENICS package.

Green (1992) used a two-dimensional k-ε turbulence model to examine air flow both through and above a small forest. The effects of the forest canopy were modelled using a sink for momentum and a source for the generation of turbulence energy. A further sink was also added to the k and ε equations to account for the additional loss of turbulence energy in plant canopies, as the larger-scale shear-generated turbulence was transformed into smaller scale motions in element wakes. PHOENICS code was used to solve the flow equations. Predictions from the model were compared with experimental data, and good agreement was observed.

Weiner and Parkin (1993) employed CFD code FLUENT to simulate the flow field of a vehicle-mounted mistblower. The standard k-ε turbulence model was applied to simulate air flow, and the equations of motion of particle were used for modelling drop dispersion. Comparisons between predictions and experimental measurements showed satisfactory agreement for major characteristics of the air jet such as centreline and horizontal velocity profiles.

Khelifi *et al* (1996a, 1996b) developed a two-dimensional finite element model to simulate airflow inside and around hoods used for pneumatic control of pest insects. Based on the 2-D Navier-Stokes equations, the model used the Stream Upwind Petrov-Galerkin method to improve the modelling of highly convective zones. A contour element concept was used to more accurately model the effects of the boundary layer in the neighbourhood of the walls. Experimental evaluation proved the validity and the capability of the model to adequately predict measured airspeeds.

Kieviet et al (1997) used the standard k-ε model to investigate air flow pattern in a concurrent pilot plant spray dryer. The model was solved using CFD code FLOW3D. The CFD model results were compared with measured data, and the agreement was found reasonable.

Forced-air convection is a common method to dry grains to acceptable storage moisture content. Air flow through the grain beds is usually described by Drake's Law, which relates pressure gradient to velocity, and continuity equation. Brook (1969) developed a finite difference method to predict air velocity and pressure distribution in a rectangular bin of corn. The model represented the log-log plots of velocity vs. pressure gradient as a series of straight line segments. However, the results from the model did not agree well with experimental pressure readings.

Marchant (1976) applied a finite element method to solve the air flows in several different storage structures. Eight-node quadrilateral elements were used in this study. The comparison of the predicted and measured air flow rate showed that the predictions might be made with reasonable accuracy. Smith (1982) used a finite element method with the frontal solution routine to calculate air velocity and pressure distribution in beds of hay or grain. While compared with experimental data, the predicted air velocity was found less accurate than pressure, and most of the error occurred in regions of high velocity. Chapman et al (1989) used a two-dimensional finite element analysis to predict air flow patterns in flat grain storages. No experiment was carried out for model validation.

2.4 MODELLING HEAT TRANSFER PROCESSES DURING PRODUCT COOLING

Product cooling involves a few heat transfer and generation processes including the convection at product and packaging material surfaces, conduction within products, conduction between products, conduction between products and packaging materials, convection and conduction within cooling medium, radiation between products and packaging materials' surfaces, internal heat generation due to respiration, and evaporative cooling effect due to transpiration. The influences of the above processes on cooling efficiency differ with cooling conditions. For instance, the effects of transpiration and respiration may be negligible during product precooling due to high cooling rates. However, these two factors have been shown to play an important role in product long-term storage.

Based on the approaches in handling cooling media, the relevant models are divided into two categories. In the first category, only heat conduction within product was modelled in detail; the temperature of cooling medium was assumed to be constant or a function of time, and no differential equation was derived for the energy conservation of cooling medium. The second-category models took account of the energy conservation for both product and cooling medium, and generally two differential equations were needed to simulate the temperature variation within the product and cooling medium.

2.4.1 Product Heat Conduction Models

Heat conduction within production is usually represented by the well-known Fourier equation for heat conduction, which can be derived from flow energy equation (eqn(2.3)) when the velocity is set to be zero.

$$C_p \frac{\partial(\rho T)}{\partial t} = \sum_{j=1}^{3} \frac{\partial}{\partial x_j}(K \frac{\partial T}{\partial x_j}) \qquad (2.16)$$

The product heat conduction model is made up of this equation in conjunction with proper boundary and initial conditions. Cleland (1990) presented five types of boundary conditions defining the heat transfer from the solid object being cooled to the external cooling medium. The most commonly used one is the third kind which is known as Newton's cooling law:

$$h_e(T_{am} - T_{x=0}) = -K\left[\frac{\partial T}{\partial x}\right]_{x=0} \tag{2.17}$$

Where:

T_{am} = ambient temperature (K).

$T_{x=0}$ = surface temperature (K).

h_e = surface heat transfer coefficient ($W \cdot m^{-2} \cdot K^{-1}$).

Cleland (1990), Lin (1994), and Amos (1995) have given comprehensive reviews for product heat conduction models. According to the solution methods for the Fourier's equation, the models can be classified as analytical, empirical and numerical models.

2.4.1.1 Analytical models

Analytical or exact solutions can be derived for one-dimensional heat conduction in regularly shaped product, based on the hypothesis of homogeneous materials, constant thermal properties, constant ambient conditions, the third kind boundary conditions, a uniform initial condition, no internal heat generation, and no mass transfer at the surface. The regular shapes include infinite slab, infinite cylinder, sphere, infinite rectangular rod, rectangular brick and finite cylinder. These solutions were well presented by Cleland (1990) and Lin (1994).

2.4.1.2 Empirical models

The base of most empirical methods is that almost all chilling processes follow a similar trend: the temperature of the product decreases at an exponential rate after an initial 'lag'

period. Instead of developing shape-specific empirical prediction methods, many efforts have been made to extend the analytical solutions for regular shapes in an empirical, but general fashion (Cleland, 1990).

An amount of theoretical and experimental work has been carried out to predict the cooling rate of irregular-shaped objects (Smith and Nelson, 1969; Smith, *et al*, 1967,1968; Clary, *et al*, 1968, 1971). A geometry index G was employed to account for the effect of geometry on product chilling. A set of time-dependent charts and graphs was presented for predicting chilling time under a wide range of conditions and geometries. A nomogram was used to find an so-called 'equivalent Biot number' so that the G value derived for Bi $\rightarrow \infty$ could be applied in situations where Bi is finite.

Cleland and Earle (1982) presented a simple method for predicting rates of chilling. A Bi-dependent shape factor E (equivalent heat transfer dimensionality) was developed. The empirical equations for calculating E for regular and irregular shapes were suggested. The method was restricted to chilling time prediction for the thermal centre position in an object. Lin (1994) and Lin *et al* (1996a, 1996b) proposed an empirical method for chilling time prediction. This method involved use of the first term of the analytical series solution for convective cooling of a sphere in conjunction with two shape-dependent parameters E (equivalent heat transfer dimensionality) and L (lag factor). A set of algebraic equations was used to calculate the E and L based on several simple dimensional measurements and Bi number. This approach can be applied to regular and irregular, 2-D and 3-D objects.

2.4.1.3 Numerical models

The heat conduction equation is commonly solved by the finite-difference or finite-element methods. As previously mentioned, the finite difference schemes require less computational efforts, but are more difficult to implement for irregular shapes while compared with finite-element analysis. Hence the application of finite elements to regular-shaped product may not be necessary, but finite elements may be more efficient in dealing with irregular shapes (Cleland, 1990).

Hayakawa (1978) modelled heat transfer and moisture loss from fresh produce subjected to cooling process. The overall configuration of produce was assumed to be an infinite slab. An implicit finite difference method was applied to solve the model. Ansari *et al* (1984) used a finite-difference method to solve the one-dimensional transient heat conduction equation in spherical co-ordinates. The enthalpy potential concept was employed to represent the cooling effect of evaporation. The calculation was made with both heat and mass transfer from the product surface for up to half the cooling time, thereafter only the heat transfer was included. The predicted temperature for apples and potatoes was compared with the measured data, and good agreement was observed. Chau and Gaffney (1990) develop a finite-difference model for simulating heat and mass transfer in the products with respiration and transpiration. Besides conduction and convection, the model also accounted for evaporative cooling due to transpiration and radiation heat transfer. The model agreed well with known analytical solutions and with experimental results.

Jiang *et al* (1987) modelled chilling of broccoli stalk. A two-dimensional axisymmetric finite-element grid was used to represent the three-dimensional object. Experimentally determined thermal properties were employed to simplify the model. Temperature differences between the simulated and measured values were within 1.1 ^{0}C. Haghighi and Segerlind (1988) proposed a finite-element model to study the simultaneous heat and mass transfer in an isotropic sphere. The model was used to solve a sample problem of drying a soybean kernel. The predicted drying curve for the soybean model compared favourably with experimental results in the literature. Pan and Bhowmik (1991) developed a finite-element model for predicting the temperature distribution in mature green tomatoes represented by real axisymmetric shape. The vertical cross-section of one half of a tomato was divided into 104 elements and 70 node points. Excellent agreement was obtained between model predictions and experimental data.

2.4.2 Product Heat Conduction plus Cooling Media Models

The above heat conduction models are most suitable for modelling heat transfer for single product items. During cooling most products are packed or bulk-stacked. The temperature

and velocity distribution within cooling media may be significantly affected by packaging and stack patterns. In these cases a simple conduction model may not be practical. A general procedure consists of the simultaneous solution of the mass, momentum and energy conservation equations for both the fluid and the solid region. However, continuous analyses of both velocity and temperature fields were not always considered fully justified in engineering design situations, where cost and time were taken into account.

Baird and Gaffney (1976) developed a numerical model to simulate temperature distribution within a bulk load of products. Heat transfer within individual products was described using heat conduction equation with connective boundary. Air flow was assumed to pass through the bulk load at a constant velocity. The change in energy of the air moving through a control volume was assumed to be equal to the change in energy of products in the control volume. Energy conversation equation was derived based on above assumptions. The finite-difference method was used to solve the model. Predicted temperature distributions with both individual products and within the bed were in good agreement with the data from experimental cooling test on oranges and grapefruit.

Remero and Chau (1987) proposed a finite-difference model to simulate heat and mass transfer when oranges were stored in a bulk refrigerated store in the absence of ventilation. The effects of respiratory heat generation and evaporative cooling due to transpiration were also accounted for. The bulk store was divided into several layers. For each layer a node was assigned to the air in the void volume and the products were discretised into elemental volumes. The air temperature and product (heat and mass transfer) characteristics were assumed not to vary with a layer. The air flow within the bulk store was described as Darcy flow through porous media. The Boussineq approximation was applied to describe natural convection. The similar approach was adopted by Bazan *et al* (1989) to predict the three-dimensional temperature response during the room cooling of a confined bin of spherical fruit. A close agreement between simulation and experimental results was obtained.

Reynoso and Michels (1988) proposed a simplified model to evaluate the performance of batch cryogenic freezers. It was assumed that the refrigerant medium in the freezer was perfectly mixed, and no internal temperature gradients exited in the products. An explicit finite-difference method was used to solve the model. The model was validated by experimental results. Comini *et al* (1995) modelled the conductive and convective heat transfer in refrigerated transport. Average air velocities and the convection coefficients were first evaluated and then specified as input data. Energy conservation equations for solid regions and fluid regions were solved using a finite-element approach.

In the models reviewed in section 2.3.2 (Wang and Touber, 1990; Van Gerwen *et al*, 1991), steady-state air flow fields were firstly solved using a CFD package. Based on predicted air flow patterns, transient energy conservation equations for air, wall and products were solved using the finite-difference method. Products stored in bulk were modelled as a porous solid.

Amos (1995) developed a multi-zone model for predicting apple temperature and weight loss with both position and time within a ventilated carton. In the model, air flow inside the carton was modelled by defining forced convection pathways with natural convection mixing to adjacent zones. The air in each zone was assumed perfectly mixed. Energy and water vapour mass balances were performed on each zone to determine air enthalpy and humidity ratio, as well as the temperature of apples and packaging materials. The model predictions fitted measured temperature data satisfactorily. However, the air flow pattern was estimated from measured air velocity data within the specified carton. This approach limits the application of the model under different package designs.

CHAPTER 3 RESEARCH OBJECTIVES

3.1 SUMMARY OF LITERATURE

The proper level of complexity is crucial while developing a workable mathematical model. The factors which can affect the model complexity include time variation (steady-state or dynamic model), space variation (1-D, 2-D, or 3-D model), number of dependent variables (velocity components, temperature or enthalpy, concentration, pressure, turbulence quantities), variation of fluid and solid properties (viscosity, density, thermal conductivity, specific heat, etc.), and boundary conditions (walls, inlet, outlet, source, sink, etc.). The more detailed a model is, the more computing power and input data are needed to solve the model.

Of the CFD-based air flow models reviewed, most of them were steady-state and were used for the flow field with relatively simple geometry. The standard k-ε model or its modified forms were employed for modelling turbulence. More complicated approaches, such as the Reynolds-stress model, were not found to be applied in agricultural and refrigeration areas. Commercial CFD packages have been successfully used to solve flow problems in many practical situations.

Considering the models for product cooling, the methodologies for modelling heat conduction within individual product have been well established. Only few researchers modelled the cooling of bulk produce in packages. The air flows in these models were treated in two ways. One was to arbitrarily define an air flow pathway according to experimental data or simplified assumptions. Another was to find air flow patterns by solving fundamental transport equations. Both defined and solved air flow distributions were assumed to be steady-state in these models. No model was found that solved all transport equations simultaneously under transient conditions.

3.2 RESEARCH OBJECTIVES

The aim of this project is to assess the usefulness of CFD as a tool in dynamic modelling of airflow and heat transfer in ventilated packages. The specific objectives are to:

(a) Conduct a detailed review of relevant literature on the basic principles and applications of CFD;

(b) Develop and implement a mathematical model which can predict the air flow patterns inside a ventilated carton and product cooling rate;

(c) Develop a scheme for experimental validation of model predictions.

The detailed predictions will include air velocity components, the temperature profiles of air, product and packaging materials when apple fruit packed in the package is cooled from ambient temperature to storage temperature. Both laminar and turbulent situations will be taken into account. The CFD facility 'PHOENICS' installed in the Department of Mathematics, Massey University, will be used to solve the model.

CHAPTER 4:MODEL DEVELOPMENT

4.1 INTRODUCTION

The model considered a one-carton situation, in which cooled air was forced to pass over a ventilated apple carton at a certain velocity. Only the air flow inside the carton was modelled, and the effect of air flow outside the carton was presented by heat convection boundary condition. The modelled apple carton was the TAI Z PACK, Count-100 carton used by ENZAFruit (International) in New Zealand for fruit export. In the carton, 100 apples were placed on four Friday trays, with 25 apples on each tray.

The solved variables in this model were air velocity components, air pressure, air temperature, fruit temperature, carton temperature, and tray temperature. Accordingly, the CFD-based model was made up of continuity equation for air flow, Navier-Stokes equations for air flow, energy conservation equation for air flow, and energy conservation equations for apple and packaging materials.

In the commercial operation of forced-air precooling, average air velocity over the carton inlets is in the range of 0.5-2.0 m/s, corresponding to Reynolds Number in the range of 2000- 8000. Under these conditions, both laminar and turbulence flows may occur. Thus the model should take account of both laminar and turbulent situations. Two modelling strategies could be adopted. In the first approach, the air flow was assumed to be steady-state while the buoyancy force due to natural convention was neglected, and the Navier-Stokes equations were decoupled from energy conservation equations; consequently the steady-state Navier-Stokes equations could be solved first, and then based on solved velocity, the energy equations were solved. The second approach was to solve all transport equations simultaneously without ignoring the effect of natural convection on air flow patterns. Both approaches were implemented in order to find the most appropriate one. Therefore four air flow situations were considered: steady-state laminar flow, steady-state turbulent flow, unsteady-state laminar flow, and unsteady-state turbulent flow.

4.2 CONSERVATION OF AIR MASS (CONTINUITY EQUATION)

Because the air velocity (less than 2 m/s) was relatively low (Mach number <<1), and the possible changes in air temperature and pressure would not cause significant changes in air density, it was reasonable to assume that the air was incompressible, and the air density was constant. According to the law of conservation of mass, air continuity equation was derived (Yuan, 1967):

$$\sum_{i=1}^{3} \frac{\partial u_i}{\partial x_i} = 0 \qquad (4.1)$$

Where:

i	=	index of axes in Cartesian coordinates.
x_i	=	spatial positions in Cartesian coordinates (m).
u_i	=	component of air velocity in x_i direction ($m \cdot s^{-1}$).

The above equation holds for laminar flow under both steady and unsteady states. For steady-state or unsteady-state turbulent flow, time-average continuity equation was used:

$$\sum_{i=1}^{3} \frac{\partial \bar{u}_i}{\partial x_i} = 0 \qquad (4.2)$$

Where:

$\bar{u}_i$	=	mean values of air velocity component u_i ($m \cdot s^{-1}$).

4.3 CONSERVATION OF AIR MOMENTUM (EQUATIONS OF MOTION)

4.3.1 General Equations

At about one atmospheric pressure, air dynamic viscosity changes between 17.16×10^{6} and 18.14×10^{6} $kg \cdot m^{-1} \cdot s^{-1}$ in the temperature range of 0 - 20 ^{0}C (Kothandaraman and Subramanyan, 1977), so air viscosity was assumed to be constant. Thus, air was treated as

incompressible fluid with constant viscosity. Based on the law of conservation of momentum, i.e. Newton's law of motion, equations of air motion (Navier-Stokes equations) were written (Yuan, 1967):

$$\rho \frac{\partial u_i}{\partial t} + \sum_{j=1}^{3} \rho u_j \frac{\partial u_i}{\partial x_j} - \sum_{j=1}^{3} \mu \frac{\partial^2 u_i}{\partial x_j^2} = X_i - \frac{\partial p}{\partial x_i} \qquad (4.3)$$

Where:

t	=	time (s).
X_i	=	components of body force per unit air volume along x_i direction ($N \cdot m^{-3}$).
p	=	air pressure ($N \cdot m^{-2}$).
μ	=	air dynamic viscosity ($N \cdot s \cdot m^{-2}$).
ρ	=	air density ($kg \cdot m^{-3}$).

4.3.2 Laminar Flow

4.3.2.1 Unsteady-state laminar flow

The only body force acting on air is gravitational force. Assuming the direction of gravitational force is opposite to x_1 axis, equation (4.3) can be written as:

$$\rho \frac{\partial u_1}{\partial t} + \sum_{j=1}^{3} \rho u_j \frac{\partial u_1}{\partial x_j} - \sum_{j=1}^{3} \mu \frac{\partial^2 u_1}{\partial x_j^2} = -\rho g - \frac{\partial p}{\partial x_1} \qquad (4.4a)$$

$$\rho \frac{\partial u_i}{\partial t} + \sum_{j=1}^{3} \rho u_j \frac{\partial u_i}{\partial x_j} - \sum_{j=1}^{3} \mu \frac{\partial^2 u_i}{\partial x_j^2} = -\frac{\partial p}{\partial x_i} \qquad (i = 2,3) \qquad (4.4b)$$

By noting that the pressure increases in negative x_1 direction, replace pressure p with p_0 (Kotake *et al*, 1993):

$$p = p_0 - \rho_{ref} g x_1 \tag{4.5}$$

Where:

ρ_{ref} = air density at reference positions ($kg \cdot m^{-3}$).

p_0 = relative air pressure ($N \cdot m^{-2}$).

g = universal gravitational constant ($m \cdot s^{-2}$).

Substitute equations (4.4a) and (4.4b) with equation (4.5), the body force term is expressed in form of buoyancy force:

$$\rho \frac{\partial u_1}{\partial t} + \sum_{j=1}^{3} \rho u_j \frac{\partial u_1}{\partial x_j} - \sum_{j=1}^{3} \mu \frac{\partial^2 u_1}{\partial x_j^2} = -(\rho - \rho_{ref}) g - \frac{\partial p_0}{\partial x_1} \tag{4.6a}$$

$$\rho \frac{\partial u_i}{\partial t} + \sum_{j=1}^{3} \rho u_j \frac{\partial u_i}{\partial x_j} - \sum_{j=1}^{3} \mu \frac{\partial^2 u_i}{\partial x_j^2} = -\frac{\partial p_0}{\partial x_i} \quad (i = 2,3) \tag{4.6b}$$

Because Mach number considered was very low, and the air temperature varied in a relatively small range, Boussinesq approximation was introduced which neglects variation of density insofar as they affect transience, convection and diffusion, but retains the effect of density variation in the buoyancy force (CHAM, 1995; Kotake, et al, 1993). The density was estimated by:

$$\rho = \rho_{ref}[1 - \beta(T - T_{ref})] \tag{4.7}$$

Where:

T = air temperature (K).

T_{ref} = air reference temperature (K).

β = air thermal expansion coefficient (K^{-1}).

Substitute equation (4.7) to equations (4.6a), and to simplify expression, ρ and p are used to express air reference density ρ_{ref} and relative pressure p_0 in following text and equations, the Navier-Stokes equations were derived in the desired form:

$$\rho\frac{\partial u_1}{\partial t}+\sum_{j=1}^{3}\rho u_j\frac{\partial u_1}{\partial x_j}-\sum_{j=1}^{3}\mu\frac{\partial^2 u_1}{\partial x_j^2}=\beta\rho(T-T_{ref})g-\frac{\partial p}{\partial x_1} \qquad (4.8a)$$

$$\rho\frac{\partial u_i}{\partial t}+\sum_{j=1}^{3}\rho u_j\frac{\partial u_i}{\partial x_j}-\sum_{j=1}^{3}\mu\frac{\partial^2 u_i}{\partial x_j^2}=-\frac{\partial p}{\partial x_i} \qquad (i=2,3) \qquad (4.8b)$$

4.3.2.2 Steady-state laminar flow

Equation (4.8a) and (4.8b) can not be solved without an air energy equation (section 4.4), which deals with air temperature in the fluid field. However, if air flow is mainly dominated by forced convection, the buoyancy force due to natural convection can be neglected. This assumption made the problem much simpler, since air flow pattern was independent of air temperature, then energy equation was decoupled from motion equations. Moreover, air flow could be assumed to be steady-state if the air velocity in carton inlets were constant. Hence, motion equations of steady laminar air flow were derived:

$$\sum_{j=1}^{3}\rho u_j\frac{\partial u_i}{\partial x_j}-\sum_{j=1}^{3}\mu\frac{\partial^2 u_i}{\partial x_j^2}=-\frac{\partial p}{\partial x_i} \qquad (4.9)$$

4.3.3 Turbulent Flow

4.3.3.1 Unsteady-state turbulence flow

As inlet air velocity increases, air flow may transform from laminar state to turbulence. In the turbulence flow, high transport of momentum and heat take place due to fluctuating components of flow. They are accompanied by an irreversible transformation of kinetic energy to thermal energy which is termed dissipation. Theoretically, a numerical solution of the Navier-Stokes equation should present a complete description of turbulent flow fields. However, as already mentioned in Chapter 2, since the irregularity of turbulence stem from the property of the equation itself, it is impossible to obtain a unique solution.

Thus, time-average Navier-Stokes equations were applied to get mean air velocity which presented a meaningful time-average air flow pattern (Yuan, 1967):

$$\rho\frac{\partial\overline{u}_1}{\partial t}+\sum_{j=1}^{3}\rho\overline{u}_j\frac{\partial\overline{u}_1}{\partial x_j}-\sum_{j=1}^{3}\frac{\partial}{\partial x_j}(\mu\frac{\partial\overline{u}_1}{\partial x_j}-\rho\overline{u_1'u_j'})=\rho\beta(\overline{T}-\overline{T}_{ref})g-\frac{\partial\overline{p}}{\partial x_1} \qquad (4.10a)$$

$$\rho\frac{\partial\overline{u}_i}{\partial t}+\sum_{j=1}^{3}\rho\overline{u}_j\frac{\partial\overline{u}_i}{\partial x_j}-\sum_{j=1}^{3}\frac{\partial}{\partial x_j}(\mu\frac{\partial\overline{u}_i}{\partial x_j}-\rho\overline{u_i'u_j'})=-\frac{\partial\overline{p}}{\partial x_i}\quad (i=2,3) \qquad (4.10b)$$

Where:

$\overline{u}_i$ = mean values of air velocity component u_i ($m\cdot s^{-1}$).

u_i', u_j' = turbulent fluctuations of air velocity components u_i, u_j ($m\cdot s^{-1}$).

$\overline{p}$ = mean value of air pressure ($N\cdot m^{-2}$).

$\overline{T}$ = time-average air temperature (K).

$\overline{T}_{ref}$ = reference time-average air temperature (K).

The time-average equations can be solved if the Reynolds stresses $-\rho\overline{u_i'u_j'}$ can be related to mean flow quantities. This was achieved by introducing an eddy-viscosity model, in which the unknown Reynolds stresses were modelled using an turbulent eddy viscosity μ_t (Launder & Spalding, 1974):

$$-\rho\overline{u_i'u_j'}=\mu_t(\frac{\partial\overline{u}_i}{\partial x_j}+\frac{\partial\overline{u}_j}{\partial x_i})-\frac{2}{3}\rho k\delta_{ij} \qquad (4.11)$$

Where:

μ_t = turbulent eddy viscosity ($N\cdot s\cdot m^{-2}$).

k = turbulent kinetic energy ($J\cdot kg^{-1}$).

δ_{ij} = Kronecker delta (δ_{ij} =1 if i=j, and 0 otherwise).

The turbulence eddy viscosity were calculated from turbulent energy k and its dissipation rate ε, which were solved by a k-ε model. Two k-ε models were assessed: Fully-Turbulence k-ε model (FTKE model) and Lam-Bremhorst Low-Reynolds-Number k-ε model (LRKE model).

(a) Fully-Turbulent k-ε model (FTKE model)

The FTKE model assumes that all points within solution grid exist in a region of full-turbulence. For the region where this requirement is not met, such as solid boundaries, wall-functions were used. The local turbulent eddy viscosity μ_t can be evaluated by the turbulent kinetic energy k and the rate of dissipation of the turbulent energy ε, which measures the rate of an irreversible transformation from turbulent to thermal energy (Launder and Spalding, 1974):

$$\mu_t = \frac{C_\mu \rho k^2}{\varepsilon} \tag{4.12}$$

Where:

C_μ = constant ($C_\mu = 0.09$).

ε = rate of dissipation of the turbulent energy ($J \cdot kg^{-1} \cdot s^{-1}$).

The k and ε are related according to the following governing equations:

$$\rho \frac{\partial k}{\partial t} + \sum_{j=1}^{3} \rho \bar{u}_j \frac{\partial k}{\partial x_j} - \sum_{j=1}^{3} \frac{\partial}{\partial x_i}[(\mu + \frac{\mu_t}{\sigma_k}) \frac{\partial k}{\partial x_j}] = \sum_{i=1}^{3} \sum_{j=1}^{3} \mu_t (\frac{\partial \bar{u}_i}{\partial x_j} + \frac{\partial \bar{u}_j}{\partial x_i}) \frac{\partial \bar{u}_i}{\partial x_j} - \rho\varepsilon + S_k \tag{4.13}$$

$$\rho \frac{\partial \varepsilon}{\partial t} + \sum_{j=1}^{3} \rho \bar{u}_j \frac{\partial \varepsilon}{\partial x_j} - \sum_{j=1}^{3} \frac{\partial}{\partial x_i}[(\mu + \frac{\mu_t}{\sigma_\varepsilon}) \frac{\partial \varepsilon}{\partial x_j}] = \sum_{i=1}^{3} \sum_{j=1}^{3} \frac{C_1 \mu_t \varepsilon}{k} (\frac{\partial \bar{u}_i}{\partial x_j} + \frac{\partial \bar{u}_j}{\partial x_i}) \frac{\partial \bar{u}_i}{\partial x_j} - \frac{C_2 \rho \varepsilon^2}{k} + S_\varepsilon \tag{4.14}$$

Where:

σ_k = constant ($\sigma_k = 1.0$).

σ_ε = constant (σ_ε=1.3).

C_1 = constant (C_1 =1.44).

C_2 = constant (C_2 =1.92).

S_k = buoyancy force production term in *k* equation ($J \cdot m^{-3} \cdot s^{-1}$).

S_ε = buoyancy force production term in ε equation ($J \cdot m^{-3} \cdot s^{-2}$).

The buoyancy force production terms S_k and S_ε were calculated as follows (Chen, *et al*, 1990):

$$S_k = -\beta \frac{\mu_t}{\mathrm{Pr}_t} \frac{\partial(\overline{T} - \overline{T}_{ref})}{\partial x_1} g \qquad (4.15)$$

$$S_\varepsilon = C_3 \frac{\varepsilon}{k} S_k \qquad (4.16)$$

Where:

Pr_t = turbulent Prandtl number.

C_3 = constant (C_3 = 1.44).

(b) Lam-Bramhorst Low-Reynolds-Number k-ε model (LRKE model).

The Low-Reynolds-Number model (LRKE model) was developed to eliminate the need for special treatments, such as wall functions, in regions where fully-turbulent conditions do not exist (Lam-Bramhorst, 1984; Chen, 1990; Hoff, et al, 1992). In the LRKE model a dumping function was used to modify the turbulent eddy viscosity:

$$\mu_t = \frac{C_\mu f_\mu \rho k^2}{\varepsilon} \qquad (4.17)$$

Where:

f_μ = dumping function for eddy viscosity.

The f_μ was expressed as the following:

$$f_\mu = (1.0 - e^{-A_\mu R_k})^2 (1.0 + \frac{A_t}{R_t}) \tag{4.18}$$

Where:

A_μ = constant ($A_\mu = 0.0165$).

A_t = constant ($A_t = 20.5$).

R_k, R_t = turbulence Reynolds numbers.

The turbulence Reynolds numbers are:

$$R_k = \frac{k^{0.5} \rho y_p}{\mu} \tag{4.19}$$

$$R_t = \frac{k^2 \rho}{\mu \varepsilon} \tag{4.20}$$

Where:

y_p = generalised normal distance from a solid boundary (m).

Accordingly the differential equations for k and ε were also modified in the LRKE model:

$$\rho \frac{\partial k}{\partial t} + \sum_{j=1}^{3} \rho \bar{u}_j \frac{\partial k}{\partial x_j} - \sum_{j=1}^{3} \frac{\partial}{\partial x_i} [(\mu + \frac{\mu_t}{\sigma_k}) \frac{\partial k}{\partial x_j}] = \sum_{i=1}^{3} \sum_{j=1}^{3} \mu_t (\frac{\partial \bar{u}_i}{\partial x_j} + \frac{\partial \bar{u}_j}{\partial x_i}) \frac{\partial \bar{u}_i}{\partial x_j} - \rho \varepsilon + S_k \tag{4.21}$$

$$\rho \frac{\partial \varepsilon}{\partial t} + \sum_{j=1}^{3} \rho \bar{u}_j \frac{\partial \varepsilon}{\partial x_j} - \sum_{j=1}^{3} \frac{\partial}{\partial x_i} [(\mu + \frac{\mu_t}{\sigma_\varepsilon}) \frac{\partial \varepsilon}{\partial x_j}] = \sum_{i=1}^{3} \sum_{j=1}^{3} \frac{C_1 f_1 \mu_t \varepsilon}{k} (\frac{\partial \bar{u}_i}{\partial x_j} + \frac{\partial \bar{u}_j}{\partial x_i}) \frac{\partial \bar{u}_i}{\partial x_j} - \frac{C_2 f_2 \rho \varepsilon^2}{k} + S_\varepsilon \tag{4.22}$$

Where:

f_1, f_2 = viscous dissipation auxiliary relations.

The f_1 and f_2 were written as:

$$f_1 = 1.0 + (\frac{A_{C1}}{f_\mu})^3 \tag{4.23}$$

$$f_2 = 1.0 - e^{-R_t^2} \tag{4.24}$$

Where:

A_{C1} = constant (A_{C1} = 0.05).

4.3.3.2 Steady-state turbulent flow

Similar to the situation of the above-mentioned laminar flow, air flow could be assumed to be steady-state if the air velocity in carton inlets were constant, and the buoyancy force due to natural convection was neglected. Thus, the time-dependent items and body force items in above turbulence governing equations disappeared.

$$\sum_{j=1}^{3} \rho \bar{u}_j \frac{\partial \bar{u}_i}{\partial x_j} - \sum_{j=1}^{3} \frac{\partial}{\partial x_j}(\mu \frac{\partial \bar{u}_i}{\partial x_j} - \rho \overline{u_i' u_j'}) = -\frac{\partial \bar{p}}{\partial x_i} \tag{4.25}$$

(a) Fully-Turbulent k-ε model (FTKE model)

$$\sum_{j=1}^{3} \rho \bar{u}_j \frac{\partial k}{\partial x_j} - \sum_{j=1}^{3} \frac{\partial}{\partial x_i}[(\mu + \frac{\mu_t}{\sigma_k})\frac{\partial k}{\partial x_j}] = \sum_{i=1}^{3}\sum_{j=1}^{3} \mu_t (\frac{\partial \bar{u}_i}{\partial x_j} + \frac{\partial \bar{u}_j}{\partial x_i})\frac{\partial \bar{u}_i}{\partial x_j} - \rho\varepsilon \tag{4.26}$$

$$\sum_{j=1}^{3} \rho \bar{u}_j \frac{\partial \varepsilon}{\partial x_j} - \sum_{j=1}^{3} \frac{\partial}{\partial x_i}[(\mu + \frac{\mu_t}{\sigma_\varepsilon})\frac{\partial \varepsilon}{\partial x_j}] = \sum_{i=1}^{3}\sum_{j=1}^{3} \frac{C_1 \mu_t \varepsilon}{k} (\frac{\partial \bar{u}_i}{\partial x_j} + \frac{\partial \bar{u}_j}{\partial x_i})\frac{\partial \bar{u}_i}{\partial x_j} - \frac{C_2 \rho \varepsilon^2}{k} \tag{4.27}$$

(b) Low-Reynolds-Number k-ε model (LRKE model)

$$\sum_{j=1}^{3}\rho\bar{u}_j\frac{\partial k}{\partial x_j}-\sum_{j=1}^{3}\frac{\partial}{\partial x_i}[(\mu+\frac{\mu_t}{\sigma_k})\frac{\partial k}{\partial x_j}]=\sum_{i=1}^{3}\sum_{j=1}^{3}\mu_t(\frac{\partial\bar{u}_i}{\partial x_j}+\frac{\partial\bar{u}_j}{\partial x_i})\frac{\partial\bar{u}_i}{\partial x_j}-\rho\varepsilon \tag{4.28}$$

$$\sum_{j=1}^{3}\rho\bar{u}_j\frac{\partial\varepsilon}{\partial x_j}-\sum_{j=1}^{3}\frac{\partial}{\partial x_i}[(\mu+\frac{\mu_t}{\sigma_\varepsilon}]\frac{\partial\varepsilon}{\partial x_j}]=\sum_{i=1}^{3}\sum_{j=1}^{3}\frac{C_1 f_1\mu_t\varepsilon}{k}(\frac{\partial\bar{u}_i}{\partial x_j}+\frac{\partial\bar{u}_j}{\partial x_i})\frac{\partial\bar{u}_i}{\partial x_j}-\frac{C_2 f_2\rho\varepsilon^2}{k} \tag{4.29}$$

Other equations and constants in section 4.3.3.1 still hold for steady-state turbulent air flow.

4.4 CONVERSATION OF ENERGY (HEAT TRANSFER EQUATIONS)

4.4.1 Energy Equations for Air Flow

The air temperature changes with time during apple cooling, so a dynamic energy equation was needed. At about one atmospheric pressure, air thermal conductivity changes between 24.42×10^3 and 25.93×10^3 $W\cdot m^{-1}\cdot K^{-1}$ in temperature range of 0 and 20 ^0C; and the air specific heat at constant pressure remains almost unchanged (Kothandaraman and Subramanyan, 1977). Thus, in the model air thermal conductivity and specific heat were assumed to be constant.

4.4.1.1 Laminar flow

For laminar flow, air was treated as viscous incompressible fluid, and the air energy conservation equation was written (Fletcher, 1988b):

$$\rho C_p\frac{\partial T}{\partial t}+\rho C_p\sum_{i=1}^{3}u_i\frac{\partial T}{\partial x_i}-K\sum_{i=1}^{3}\frac{\partial^2 T}{\partial x_i^2}=S_E \tag{4.30}$$

Where:

T	=	air temperature (K).
C_p	=	air specific heat at constant pressure ($J \cdot kg^{-1} \cdot K^{-1}$).
K	=	air thermal conductivity ($W \cdot m^{-1} \cdot K^{-1}$).
S_E	=	source term in energy equation ($W \cdot m^{-3}$).

The expression of source term S_E can be found from relevant literature (Rodi, 1979).

4.4.1.2 Turbulent flow

For turbulent flow the time-average energy equation was used (CHAM, 1995; Rodi, 1979):

$$C_p \frac{\partial(\rho \overline{T})}{\partial t} + \sum_{j=1}^{3} C_P \frac{\partial(\rho \overline{u}_j \overline{T})}{\partial x_j} - \sum_{j=1}^{3} \frac{\partial}{\partial x_j}(K \frac{\partial \overline{T}}{\partial x_j} - \rho C_p \overline{T' u'_j}) = \overline{S_E} \qquad (4.31)$$

Where:

$\overline{T}$	=	time-average air temperature (K).
$\overline{S_E}$	=	time-average source term in energy equation ($W \cdot m^{-3}$).

The Reynolds flux terms $-\rho C_P \overline{T' u'_j}$ were related to the average temperature field by a turbulent diffusion coefficient, which is usually assumed to be proportional to eddy viscosity through turbulent Prandtl number:

$$-\rho C_P \overline{T' u'_j} = \Gamma_t \frac{\partial \overline{T}}{\partial x_j} \qquad (4.32)$$

$$\mathrm{Pr}_t = \frac{C_p \mu_t}{\Gamma_t} \qquad (4.33)$$

Where:

Γ_t	=	turbulent diffusion coefficient ($W \cdot m^{-1} \cdot K^{-1}$).
Pr_t	=	turbulent Prandtl number.

4.4.2 Energy Equation for Apple

During rapid precooling, it was reasonable to neglect the effect of fruit respiration heat and the surface heat transfer due to transpiration. It was also assumed that apple fruit is made of uniform solid material with constant thermal properties. The energy equation for each apple was written:.

$$\rho_a C_a \frac{\partial T_a}{\partial t} - K_a \sum_{i=1}^{3} \frac{\partial^2 T_a}{\partial x_i^2} = 0 \qquad (4.34)$$

Where:

ρ_a = apple density ($kg \cdot m^{-3}$).

C_a = apple specific heat ($J \cdot kg^{-1} \cdot K^{-1}$).

T_a = apple temperature (K).

K_a = apple thermal conductivity ($W \cdot K^{-1} \cdot m^{-1}$).

4.4.3 Energy Equation For Carton And Trays

Similarly, carton and trays were assumed to be uniform materials with constant thermal properties. It was also assumed that no heat was generated inside packaging materials. The energy equations for tray and cartons were derived:

$$\rho_{tr} C_{tr} \frac{\partial T_{tr}}{\partial t} - K_{tr} \sum_{i=1}^{3} \frac{\partial^2 T_{tr}}{\partial x_i^2} = 0 \qquad (4.35)$$

$$\rho_c C_c \frac{\partial T_c}{\partial t} - K_c \sum_{i=1}^{3} \frac{\partial^2 T_c}{\partial x_i^2} = 0 \qquad (4.36)$$

Where:

ρ_{tr} = tray density ($kg \cdot m^{-3}$).

C_{tr} = tray specific heat ($J \cdot kg^{-1} \cdot K^{-1}$).

T_{tr} = tray temperature (K).

K_{tr} = tray thermal conductivity ($W \cdot m^{-1} \cdot K^{-1}$).

ρ_c = carton density ($kg \cdot m^{-3}$).

C_c = carton specific heat ($J \cdot kg^{-1} \cdot K^{-1}$).

T_c = carton temperature (K).

K_c = carton thermal conductivity ($W \cdot m^{-1} \cdot K^{-1}$).

4.5 INITIAL CONDITIONS

The starting-time values for variables were needed to solve the above equations. In general, a uniform initial value was set for each variable in its related domains.

4.5.1 Initial Conditions for Air

It was assumed that the air in the considered domain was initially at rest with constant temperature and pressure. Thus, initial conditions for air were written:

$u_i = 0$ $(i = 1,2,3)$ when $t = 0$ (4.37)

$T = T_i$ when $t = 0$ (4.38)

$p = p_i$ when $t = 0$ (4.39)

Where:

T_i = value of air initial temperature (K).

p_i = value of air initial pressure ($N \cdot m^{-2}$).

For turbulent flow, the initial values for turbulent energy k and turbulent energy dissipation rate ε were also needed.

$k = 0$ when $t = 0$ (4.40)

$\varepsilon = 0$ when $t = 0$ (4.41)

4.5.2 Initial Conditions for Apple And Packaging Materials

It was assumed that apples and packaging materials possessed uniform temperatures at the beginning of formulation:

$T_a = T_{ai}$ when t = 0 (4.42)

$T_{tr} = T_{tri}$ when t = 0 (4.43)

$T_c = T_{ci}$ when t = 0 (4.44)

Where:

T_{ai} = value of apple initial temperature (K).

T_{tri} = value of tray initial temperature (K).

T_{ci} = value of carton initial temperature (K).

4.6 BOUNDARY CONDITIONS

In the present formulation, the boundaries were divided into four categories: wall-type, inflow, fixed pressure, and external carton surface boundaries.

4.6.1 Wall-Type Boundary Conditions

Wall-type boundary conditions specified the boundaries between solid phases and fluid phase, which include the surfaces of the apples, the surfaces of the trays, and the internal surfaces of the carton.

4.6.1.1 Laminar flow

For laminar flow only air velocity at solid surfaces needed to be defined. Due to the effect of viscosity, air flow had the same velocity as the surface. All considered surfaces were at rest.

$u_i = 0$ (I =1,2,3) at any solid surface (4.45)

4.6.1.2 Turbulence flow

Apart from air velocity, turbulence energy k and its dissipation rate ε were defined. The velocity and turbulence parameters were defined separately for the FTKE and LRKE models.

(a) Fully-Turbulent k-ε model

Close to the wall, the Reynolds number becomes sufficiently low that molecular viscosity influences production, dissipation, and diffusion of turbulence energy. In this region the general transport equations can not be applied. The wall function was therefore employed to provide near-wall boundary conditions for the momentum and turbulence transport equations. In this method the dimensionless distance from the wall to the first node, y^+, was used to find the velocity, turbulence energy parameters k and ε from the equilibrium wall functions while y^+ ranges from 30 to 130 (CHAM, 1995):

$$\frac{u_R}{u_*} = \frac{1}{\kappa}\ln(Ey^+) \tag{4.46}$$

$$k = \frac{u_*^2}{C_\mu^{0.5}} \tag{4.47}$$

$$\varepsilon = \frac{C_\mu^{0.75} k^{1.5}}{\kappa y_p} \tag{4.48}$$

$$y^+ = \frac{u_* y_p \rho}{\mu} \tag{4.49}$$

$$u_* = (\frac{\tau_w}{\rho})^{0.5} \tag{4.50}$$

Where:

u_R = resultant velocity parallel to the wall ($m \cdot s^{-1}$).

u_* = friction velocity ($m \cdot s^{-1}$).

y^+ = dimensionless distance from the wall.

κ = van Karman's constant ($\kappa = 0.41$).

E = roughness parameter (E = 8.6).

y_p = generalised normal distance from a solid boundary (m).

τ_w = wall shear stress ($N \cdot m^{-2}$).

(b) Low-Reynolds-Number k-ε model

In the LRKE model no wall functions were needed. The boundary conditions were simpler than in the FTKE model.

$u_i = 0$ (I =1,2,3) at any solid surface (4.51)

$k = 0$ at any solid surface (4.52)

$\frac{\partial \varepsilon}{\partial x_i} = 0$ at any solid surface (4.53)

4.6.2 Inflow Boundary Conditions

The inflow boundary was referred to as the opening through which the air was assumed to enter a domain with constant mass flow rate. It was also assumed that air was evenly distributed over the opening. The inlet boundaries were specified as inflow boundaries:

$T = T_{in}$ at any inflow boundary (4.54)

$u_i = u_{i\text{-}in}$ (I is the direction perpendicular to the opening)

$u_i = 0$ (I is the direction parallel to the opening)

at any inflow boundary (4.55)

$k = 0.005 u_{i\text{-}in}^2$ at any inflow boundary (4.56)

$\varepsilon = 10 C_\mu^{0.75} k^{1.5} H^{-1}$ at any inflow boundary (4.57)

Where:

T_{in} = value of air temperature at the opening (K).

$u_{i\text{-}in}$ = value of air velocity at the opening ($m \cdot s^{-1}$).

H = characteristic inlet dimension (m).

4.6.3 Fixed-Pressure Boundary Conditions

The fixed-pressure boundary conditions specified the openings where the pressure in the outlet was kept at a fixed value. The outlet boundaries were treated as the fixed-pressure boundaries:

$p = p_{fixed}$ at any fixed value boundary (4.58)

Where:

p_{fixed} = value of air pressure at the opening ($N \cdot m^{-2}$).

4.6.4 Boundary Conditions for Carton External Surfaces

The external carton surfaces were typically convection heat transfer boundaries, following Newton's Law of cooling:

$$-k(\frac{\partial T_c}{\partial x_i})_{surface} = h_c(T_e - T_c) \quad \text{(i is the direction perpendicular to the surface)} \tag{4.59}$$

Where:

T_e = temperature of external air flow (K).

h_e = surface heat transfer coefficient ($W \cdot m^{-2} \cdot K^{-1}$).

4.7 SUMMARY OF PARTIAL DIFFERENTIAL EQUATIONS

All the partial differential equations previously given described the conservation of certain properties including momentum, energy, mass, turbulent energy. These variables were

thought of obeying a generalised conservation principle, therefore a general differential equation was written for the conservation of all the properties (Patankar, 1980):

$$\frac{\partial}{\partial t}(\rho\phi) + div(\rho\mathbf{u}\phi) = div(\Gamma grad\phi) + S \qquad (4.60)$$

Where:

ϕ	=	dependent variable.
Γ	=	diffusion coefficient.
S	=	source term.
t	=	time (s).
u	=	air velocity vector ($m \cdot s^{-1}$).
ρ	=	air density ($kg \cdot m^{-3}$).
div	=	divergence.

The four terms in the general differential equation were the unsteady term $\frac{\partial}{\partial t}(\rho\phi)$, the convection term $div(\rho\mathbf{u}\phi)$, the diffusion term $div(\Gamma grad\phi)$, and the source term S. The dependent variable ϕ stood for a variety of different quantities including mass fraction of fluid, temperature, velocity components, turbulence kinetic energy, and rate of dissipation of turbulent energy. Accordingly, for each of these variables, an appropriate meaning was given to the diffusion coefficient Γ and the source term S. Table 4.1 shows the details of the governing PDEs expressed in the form of the general differential equation.

From Table 4.1 it can be seen that the use of div(Γgradϕ) as diffusion term did not limit the general ϕ equation to gradient-driven diffusion process, since not all diffusion fluxes were governed by the gradient of the relevant variable. Whatever terms that could not be fitted into the normal diffusion term were always expressed as a part of the source term. The gradient-diffusion term was explicitly included in the general ϕ equation because most dependent variables did require a prominent diffusion term of this nature.

All the relevant differential equations for heat transfer, fluid flow, turbulence were treated as particular cases of the general ϕ equation. As a consequence, it was operative to formulate a general numerical method and to prepare general-purpose computer programs, which were able to be repeatedly used for different meanings of ϕ along with appropriate expressions for Γ and S, as well as with appropriate initial and boundary conditions.

Table 4.1 Partial differential equations in the generalised form

Fluid characteristics	Law of conversation	Equation	dependent variable ∅	diffusion coefficient Γ	source term S	Note
All kinds of air flow	Mass	Continuity equation (4.1 and 4.2)	1	0	0	no unsteady term
Steady-state laminar air flow	Momentum	Equation of motion (4.9)	u_i (i =1,2,3)	μ	$-\frac{\partial p}{\partial x_i}$	no unsteady term
Unsteady-state laminar air flow	Momentum	Equation of motion (4.6a)	u_1 (u)	μ	$\beta(T-T_{ref})g-\frac{\partial p}{\partial x_1}$	
Unsteady-state laminar air flow	Momentum	Equation of motion (4.6b)	u_i (i =2,3)	μ	$-\frac{\partial p}{\partial x_i}$	
Laminar air flow	Energy	Equation of energy (4.30)	T	$\frac{K}{C_P}$	S_E	
Steady-state turbulent air flow	Momentum	Equation of motion (4.25)	$\overline{u}_i$ (i = 1,2,3)	μ+μ_t	$\sum_{j=1}^{3}(\frac{\partial}{\partial x_j}(\mu_t\frac{\partial \overline{u}_j}{\partial x_i}-\frac{2}{3}\rho k\delta_{ij}))$ $-\frac{\partial \overline{p}}{\partial x_i}$	no unsteady term
Steady-state turbulent air flow	Turbulent kinetic energy	Equation of k (4.26) (FTKE model)	k	$\mu+\frac{\mu_t}{\sigma_k}$	$\sum_{i=1}^{3}\sum_{j=1}^{3}\mu_t(\frac{\partial \overline{u}_i}{\partial x_j}+\frac{\partial \overline{u}_j}{\partial x_i})\frac{\partial \overline{u}_i}{\partial x_j}$ $-\rho\varepsilon$	no unsteady term
Steady-state turbulent air flow	Rate of dissipation of turbulent energy	Equation of ε (4.27) (FTKE model)	ε	$\mu+\frac{\mu_t}{\sigma_\varepsilon}$	$\sum_{i=1}^{3}\sum_{j=1}^{3}\frac{C_1\mu_t\varepsilon}{k}(\frac{\partial \overline{u}_i}{\partial x_j}+\frac{\partial \overline{u}_j}{\partial x_i})\frac{\partial \overline{u}_i}{\partial x_j}$ $-\frac{C_2\rho\varepsilon^2}{k}$	no unsteady term

Table 4.1 (continued) Partial differential equations in the generalised form

Fluid characteristics	Law of conversation	Equation	dependent variable ∅	diffusion coefficient Γ	source term S	Note
Steady-state turbulent air flow	Turbulent kinetic energy	Equation of k (4.28) (LRKE model)	k	$\mu+\frac{\mu_t}{\sigma_k}$	$\sum_{i=1}^{3}\sum_{j=1}^{3}\mu_t(\frac{\partial\overline{u}_i}{\partial x_j}+\frac{\partial\overline{u}_j}{\partial x_i})\frac{\partial\overline{u}_i}{\partial x_j}$ $-\rho\varepsilon$	no unsteady term
Steady-state turbulent air flow	Rate of dissipation of turbulent energy	Equation of ε (4.29) (LRKE model)	ε	$\mu+\frac{\mu_t}{\sigma_\varepsilon}$	$\sum_{i=1}^{3}\sum_{j=1}^{3}\frac{C_1 f_1\mu_t\varepsilon}{k}(\frac{\partial\overline{u}_i}{\partial x_j}+\frac{\partial\overline{u}_j}{\partial x_i})\frac{\partial\overline{u}_i}{\partial x_j}$ $-\frac{C_2 f_2\rho\varepsilon^2}{k}$	no unsteady term
Unsteady-state turbulent air flow	Momentum	Equation of motion (4.10a)	$\overline{u}_1$	$\mu+\mu_t$	$\sum_{j=1}^{3}(\frac{\partial}{\partial x_j}(\mu_t\frac{\partial\overline{u}_j}{\partial x_1}-\frac{2}{3}\rho k\delta_{1j}))$ $+\beta(\overline{T}-\overline{T}_{ref})g-\frac{\partial\overline{p}}{\partial x_1}$	
Unsteady-state turbulent air flow	Momentum	Equation of motion (4.10b)	$\overline{u}_i$ (i = 2,3)	$\mu+\mu_t$	$\sum_{j=1}^{3}(\frac{\partial}{\partial x_j}(\mu_t\frac{\partial\overline{u}_j}{\partial x_i}-\frac{2}{3}\rho k\delta_{ij}))$ $-\frac{\partial\overline{p}}{\partial x_i}$	
Unsteady-state turbulent air flow	Turbulent kinetic energy	Equation of k (4.13) (FTKE model)	k	$\mu+\frac{\mu_t}{\sigma_k}$	$\sum_{i=1}^{3}\sum_{j=1}^{3}\mu_t(\frac{\partial\overline{u}_i}{\partial x_j}+\frac{\partial\overline{u}_j}{\partial x_i})\frac{\partial\overline{u}_i}{\partial x_j}$ $-\rho\varepsilon+S_k$	
Unsteady-state turbulent air flow	Rate of dissipation of turbulent energy	Equation of ε (4.14) (FTKE model)	ε	$\mu+\frac{\mu_t}{\sigma_\varepsilon}$	$\sum_{i=1}^{3}\sum_{j=1}^{3}\frac{C_1\mu_t\varepsilon}{k}(\frac{\partial\overline{u}_i}{\partial x_j}+\frac{\partial\overline{u}_j}{\partial x_i})\frac{\partial\overline{u}_i}{\partial x_j}$ $-\frac{C_2\rho\varepsilon^2}{k}+S_\varepsilon$	

Table 4.1 (continued) Partial differential equations in the generalised form

Fluid characteristics	Law of conversation	Equation	dependent variable ∅	diffusion coefficient Γ	source term S	Note
Unsteady-state turbulent air flow	Turbulent kinetic energy	Equation of k (4.21) (LRKE model)	k	$\mu+\frac{\mu_t}{\sigma_k}$	$\sum_{i=1}^{3}\sum_{j=1}^{3}\mu_t(\frac{\partial\bar{u}_i}{\partial x_j}+\frac{\partial\bar{u}_j}{\partial x_i})\frac{\partial\bar{u}_i}{\partial x_j}$ $-\rho\varepsilon+S_k$	
Unsteady-state turbulent air flow	Rate of dissipation of turbulent energy	Equation of ε (4.22) (LRKE model)	ε	$\mu+\frac{\mu_t}{\sigma_\varepsilon}$	$\sum_{i=1}^{3}\sum_{j=1}^{3}\frac{C_1 f_1\mu_t\varepsilon}{k}(\frac{\partial\bar{u}_i}{\partial x_j}+\frac{\partial\bar{u}_j}{\partial x_i})\frac{\partial\bar{u}_i}{\partial x_j}$ $-\frac{C_2 f_2\rho\varepsilon^2}{k}+S_\varepsilon$	
Turbulent air flow	Energy	Equation of energy (4.32)	$\bar{T}$	$\frac{K}{C_p}+\frac{\mu_t}{\mathrm{Pr}_t}$	$\overline{S_E}$	
Apple	Energy	Equation of energy (4.35)	T_a	$\frac{K_a}{C_a}$	0	
Tray	Energy	Equation of energy (4.36)	T_{tr}	$\frac{K_{tr}}{C_{tr}}$	0	
Carton	Energy	Equation of energy (4.37)	T_c	$\frac{K_C}{C_C}$	0	

CHAPTER 5:MODEL IMPLEMENTATION

5.1 INTRODUCTION

The overall model was made up of a group of partial differential equations, auxiliary equations along with boundary and initial conditions. It was impossible to solve these equations analytically. Thus the numerical method was applied for approximate solutions. As mentioned in CHAPTER 4, all the relevant differential equations for heat transfer, fluid flow, turbulence were treated as particular cases of the general ϕ equation (equation 4.60). Consequently it was necessary to formulate a general numerical method and to prepare general-purpose computer programs, which were able to be repeatedly used for different meanings of ϕ along with appropriate expressions for diffusion coefficient Γ and source term S, as well as with appropriate initial and boundary conditions.

The process of obtaining the computational solutions consisted of two stages. The first stage was discretisation which converted the continuous partial differential equations and auxiliary equations into a discrete system of algebraic equations. The second stage used an equation solver to provide the solution of the system of algebraic equations. The above solution process was achieved using a Computational Fluid Dynamics (CFD) package PHOENICS (CHAM, UK Ltd), which employed the finite volume method to convert the PDEs into a set of algebraic equations, which were then solved by iteration.

5.2 STRUCTURE OF PHOENICS

PHOENICS consists of four computer codes: a pre-processor called SATELLITE, a processor called EARTH, a post-processor called PHOTON, and a separate self-instruction program called POLIS. The relationship among these components is illustrated in Figure 5.1 (CHAM, 1995).

The SATELLITE station converts instructions provided by a user into a data file which the EARTH can process. A user can give instructions by either writing a Q1 file in the

PHOENICS Input Language (PIL), or inputting data through a MENU system. These instructions enable the user to define the relevant problem.

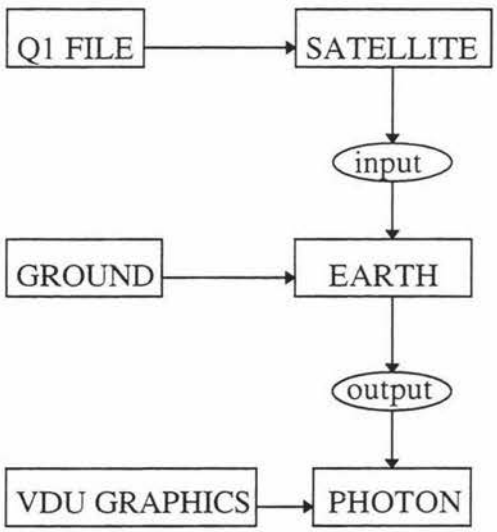

Figure 5.1 Structure of the programmes of PHOENICS

EARTH is the main flow-simulation software. It reads the data file from SATELLITE and executes the corresponding computations, and then produces output files which can be read by the user, or processed by PHOTON. EARTH also has FORTRAN subroutines accessible to the user. These subroutines are stored in GROUND. The GROUND supplies necessary boundary conditions, material properties and output control features which are not included in EARTH.

PHOTON is the graphic post-processor which reads the data in the output file written by EARTH and displays them in a graphic form on the computer screen in response to the instructions given by the user.

POLIS stands for PHOENICS On-Line Information System which provides information and tutorial needed for the user to learn how to use PHOENICS,

5.3 DISCRETISATION

In PHOENICS package, the finite volume method is the discretisation tool, which divides the calculation domain into a number of non-overlapping control volumes such that there is one control volume surrounding each grid point. The differential equations are then integrated over each control volume. Piecewise profiles expressing the variation of ϕ between the grid points are used to evaluate the required integrals. The result is the generation of discretization equations containing the values of ϕ for a group of grid points. A discretisation equation obtained in this manner expresses the conservation principle for ϕ in the finite volume, just as the PDE expresses it in an infinitesimal control volume (CHAM, 1995).

5.3.1 Space Discretization

5.3.1.1 Configuration of apple carton

The modelled apple carton was the TAI Z PACK, Count-100 carton used by ENZAFruit in New Zealand for fruit export (Figure 5.2). In the carton 100 apples were placed on four Friday trays, with 25 apples on each tray. The photograph (Figure 5.3) shows the arrangement of apples on the trays. The dimensions of carton are illustrated in Figure 5.4. The average mass of each apple is 0.186 kg (ENZA, 1996).

Because of irregularity and nonuniformity of apple shape, it was not reasonable to treat the apple as a simple geometrical object such as sphere. Compared with real fruit, significant errors were usually introduced into the surface area and volume calculated from the simplified geometry. By the following correlations derived from experimental data (Clayton, et al, 1995), the volume and surface area of apple were calculated:

$$A = dM^{e} \tag{5.1}$$

$$A = cV_a^{f} \tag{5.2}$$

Where:

A	=	apple surface area (m^2).
M	=	apple mass (kg).
V_a	=	apple volume (m^3).
c, d, e, f	=	parameters.

The results of calculation are shown in Table 5.1.

Table 5.1 Calculation of Count-100 apple volume and surface area

mass (kg)	d	e	c	f	volume (m^3)	area (m^2)
0.186	0.0575	0.687	4.88	0.661	0.000210305	0.018106

The apple was initially assumed to be made up of a cylinder and two truncated cones. However, the trays were modelled as flat plates in order to maintain mesh orthogonality to a certain degree (section 5.3.1.2), so modification in initially modelled apple shape was made to accommodate the assumed tray geometry. Figure 5.5 shows the dimensions of the model apple. The relative positions of apples on a tray are illustrated in Figure 5.6. The displacements C1 and C2, and apple dimensions H, L1 and B2 were based on the measured dimensions of carton, tray and apples. The other dimensions of apple were chosen such that they satisfied the arrangement defined by C1, C2 , H, L1 and B1, and provided the closet values of volume and surface area to that calculated from the apple mass. Table 5.2 gave the dimensions and displacements specified in Figure 5.5 and 5.6, as well as the resulting surface area and volume of the model apple.

Table 5.2 Values used for specifying model apple

Dimension	A1	A2	B1	B2	L1	L2	H
Value (m)	0.020	0.040	0.050	0.070	0.065	0.025	0.060
Displacement	C1			C2			
Value (m)	0.062			0.090			
Area (m^2)				Volume (m^3)			
0.01834				0.0002136			

Figure 5.2 TAI Z PACK Count-100 apple carton

Figure 5.3 Arrangement of apples on a tray

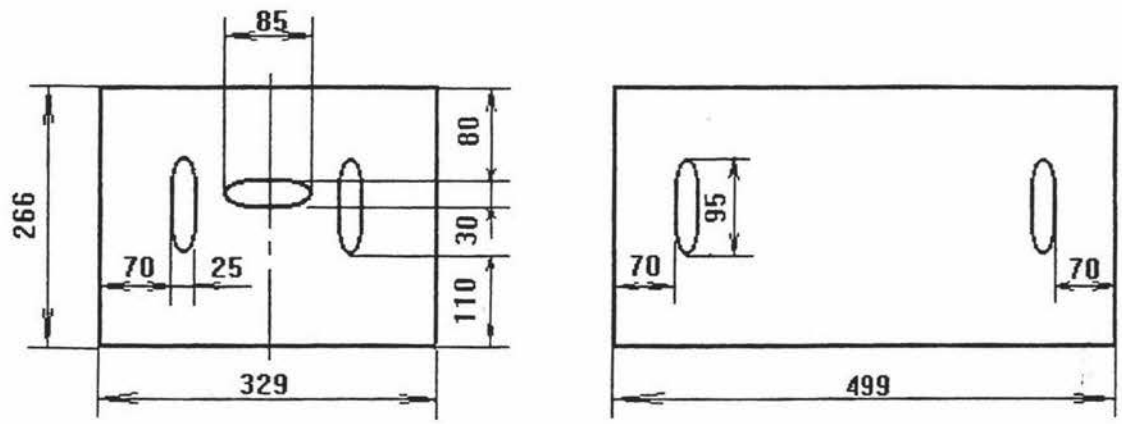

Figure 5.4 Dimensions of TAI Z PACK Count-100 apple carton

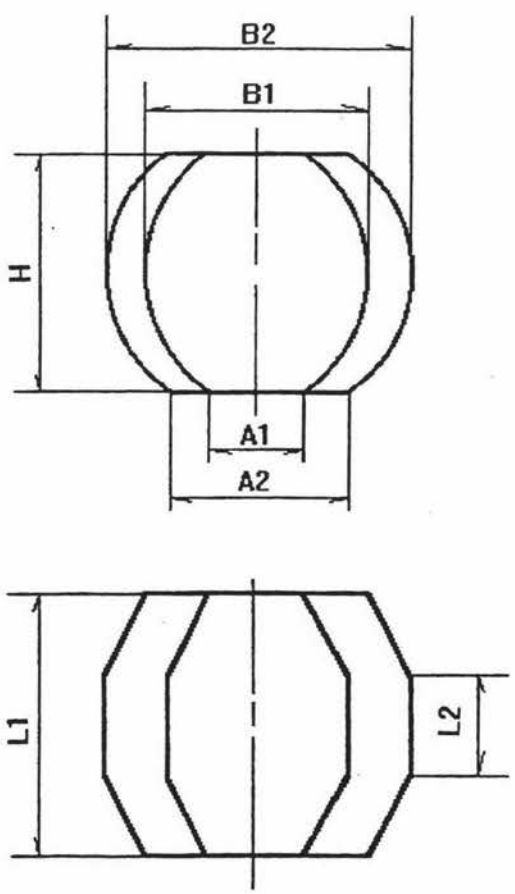

Figure 5.5 Dimensions of model apple (top: front view, bottom: plan)

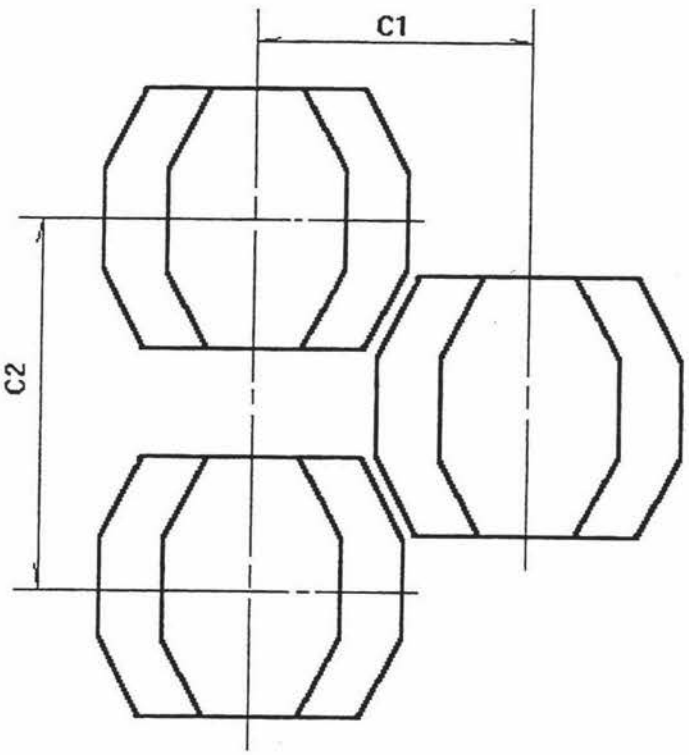

Figure 5.6 Relative positions of model apples on a tray

5.3.1.2 Grid generation

In PHOENICS the calculation domain is divided into a number of sub-domains called cells. The grid has an I, J, K structure in which the location of each cell is specified by the cell indices (IX, JY, KZ) which are the count numbers of the cell in x, y, z directions. Each cell constitutes six faces which are named as South (s), North (n), West (w), East (e), Low (l), and High (h) faces. An array of cells with the same KZ is referred to as a slab. To avoid occurrence of wavy velocity and pressure fields, the staggered grid is used in PHOENICS. The scalars such as temperature and turbulent energy are stored at the centre points of six-sided cells, with values supposed to be typical of the whole cell. The velocity vector components are stored at the centre points of the six cell faces. Vectors quantities are computed by reference to cells which are staggered with respect to the scalar cells. The convention adopted by PHOENICS was displayed in Figure 5.7.

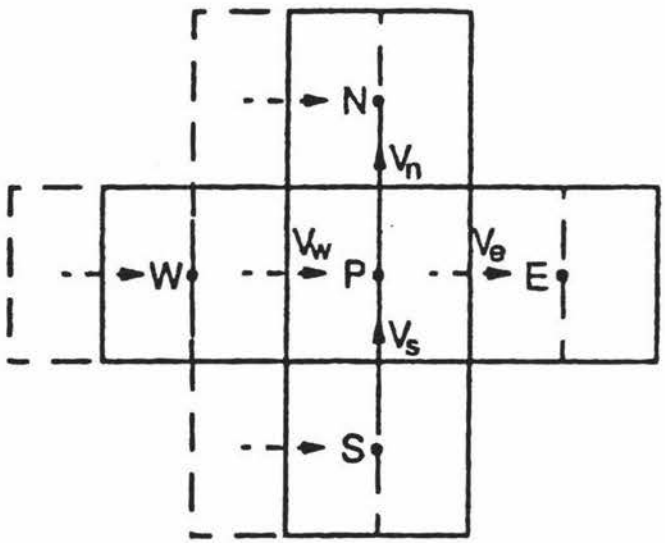

Figure 5.7 A cell with its four neighbours in the staggered grid (the high (H) and low (L) neighbours are omitted) (adapted from Wang, 1990).

PHOENICS can employ Cartesian, Cylindrical-polar, and Body-fitted grids. The carton with apples and trays inside exhibited very complicated configuration. It was impossible to outline the structural characteristics with the regular Cartesian or cylindrical polar coordinates. Therefore the Body-Fitted Coordinates (BFC) grid system was used. BFC grids provided good geometric presentation, particularly for the surface boundary layers, and hence for wall friction and heat transfer. Usage of BFC might also reduce the diffusion error in numerical solutions due to the difference between the grid and fluid flow directions (CHAM, 1995).

The details of the BFC grid generation are given in Group 6 of Q1 file (Code STL1, attached disk). Because of the symmetric structure of the carton, only half of the domain was needed for numerical solution. Positive z axis was decided as the direction of main stream, and y axis as the carton height, x axis as the width. The cell numbers in X, Y, Z directions were 14, 31 and 46. The entire grid system had 19964 cells. The BFC grid was established according to the shapes of apples, trays and carton walls . The domain was cut into a series of sections by 47 planes perpendicular to z axis (plane K1-K47). These planes had three typical structures (Figure 5.8, 5.9 and 5.10). The grids for all the planes were

generated respectively. The whole grid system was formed by combining the grids of these planes. Figure 5.11 - 5.19 displays the grids perpendicular to y axis (plane J1-J32), and to x axis (plane I1-I15). Figure 5.8-5.14 also provide the indices used for specifying the locations of cells.

In order to maintain grid orthogonality, and to define the grid more conveniently, some modifications in the dimensions of carton and trays were made. The original and modified dimensions were showed in Table 5.3. In order to maintain the mass and thermal resistance unchanged, the density and thermal conductivity of carton and tray have to be adjusted to account for the modified volume and thickness (section 6.2.3).

Table 5.3 Original and modified dimensions of carton and tray

Dimension	Original	Modified
Carton length (mm)	499	496
Carton width (mm)	329	342
Carton height (mm)	266	275
Carton side wall thickness (mm)	6	10
Carton top and bottom wall thickness (mm)	3	5
Tray thickness (mm)	2	5

5.3.2 Derivation of Discretisation Equations

To derive the discretisation equations, the grid-point cluster shown in the Figure 5-6 was employed. The attention was focused on the grid point P, which had the grid points E, W, N, S, H, L as its neighbours. The subscripts e, w, n, s, h, l denoted the surfaces of the control volume. In the finite volume method the discretisation equation was derived by integrating Equation (4.60) over the control volume and a time interval:

$$\int_V \int_t^{t+\Delta t} \frac{\partial}{\partial t}(\rho\phi)dt\ dv = \int_t^{t+\Delta t}\int_V div(\Gamma grad\phi - \rho\mathbf{u}\phi)dv\ dt + \int_t^{t+\Delta t}\int_V Sdv\ dt \qquad (5.3)$$

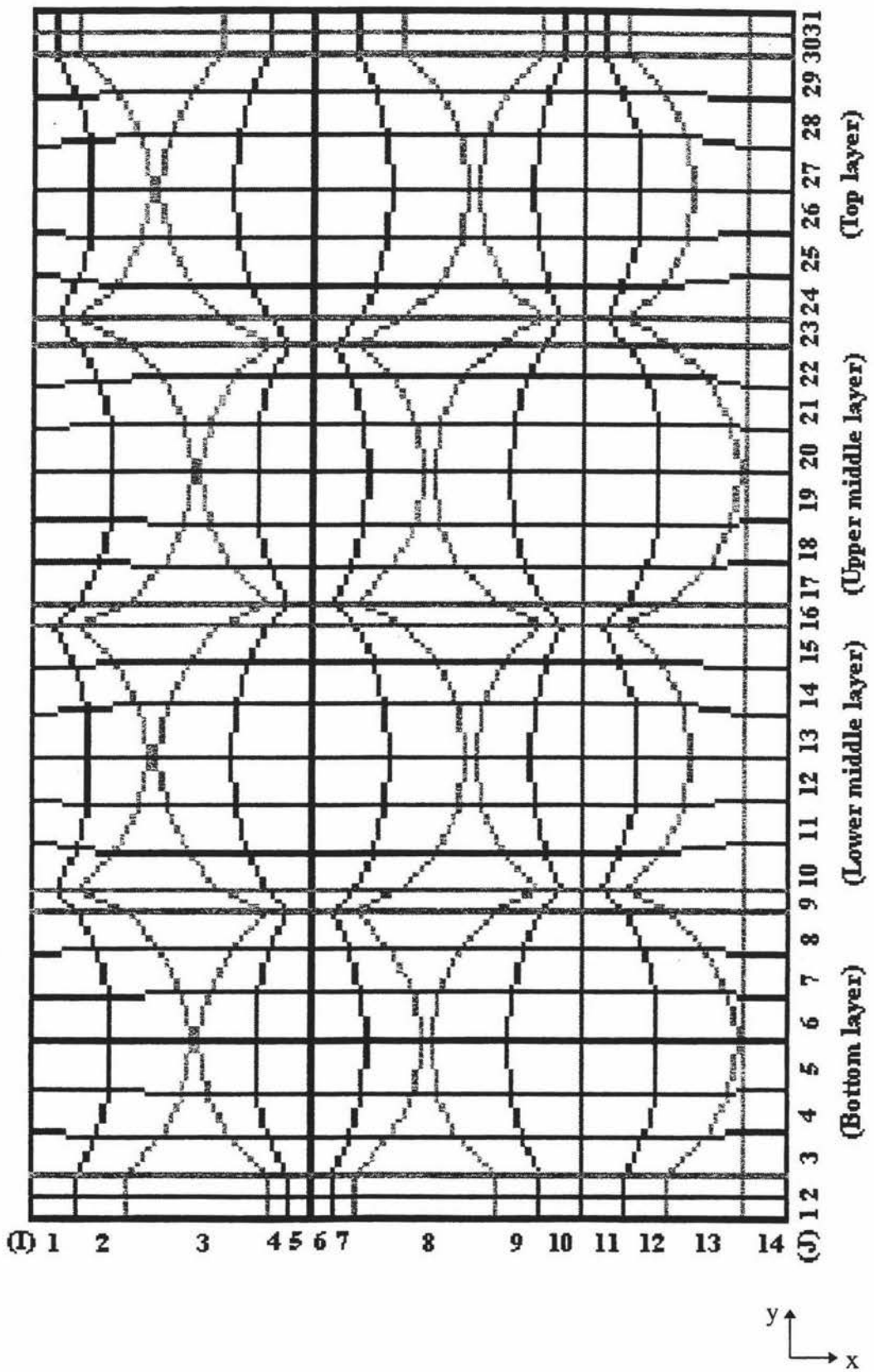

Figure 5.8 Grid for plane K1-K3, K9-K11, K17-K19, K25-K27, K33-35, K41-K43

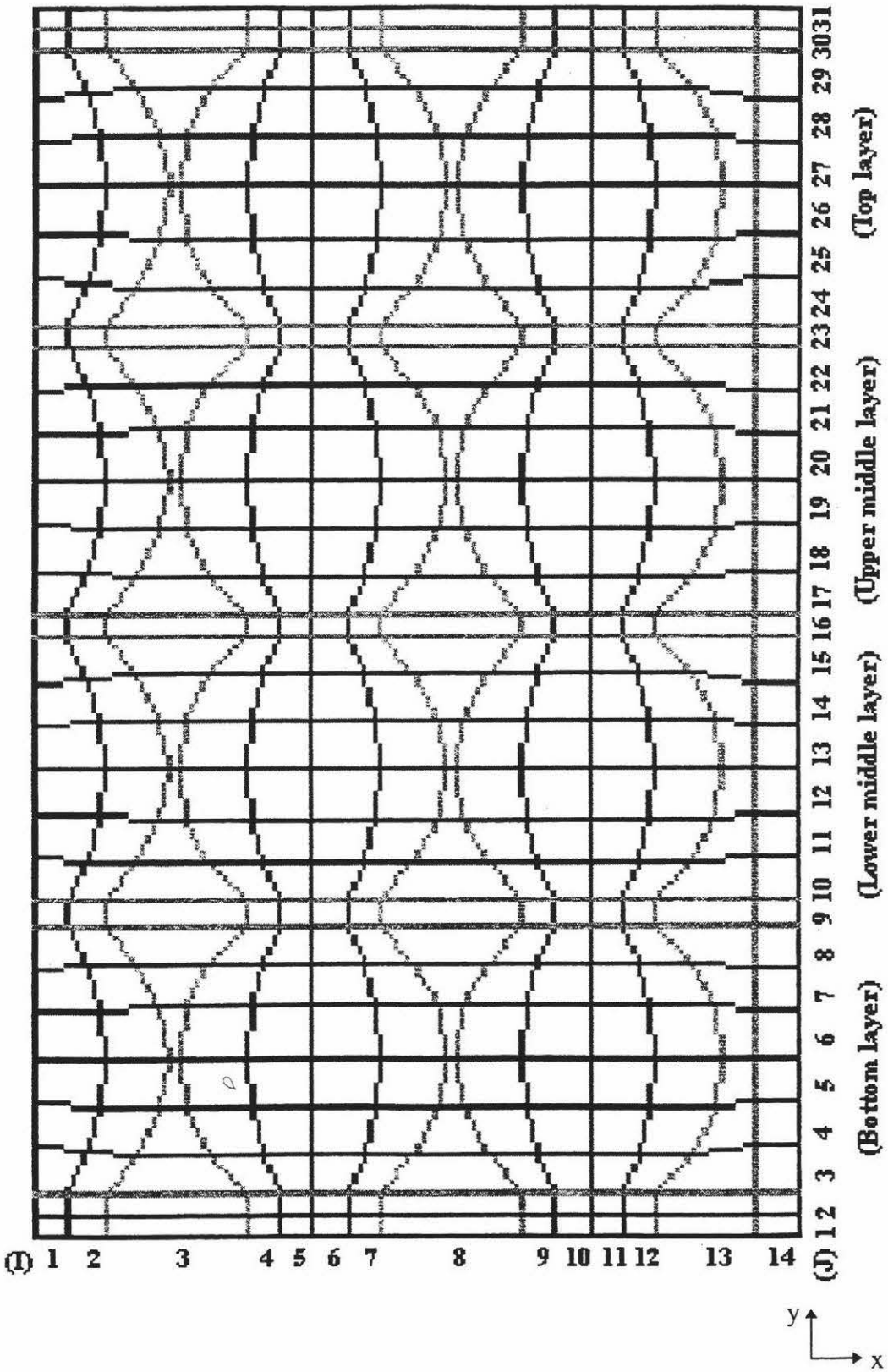

Figure 5.9 Grid for plane K4, K8, K12, K16, K20, K24, K28, K32, K36, K40, K44

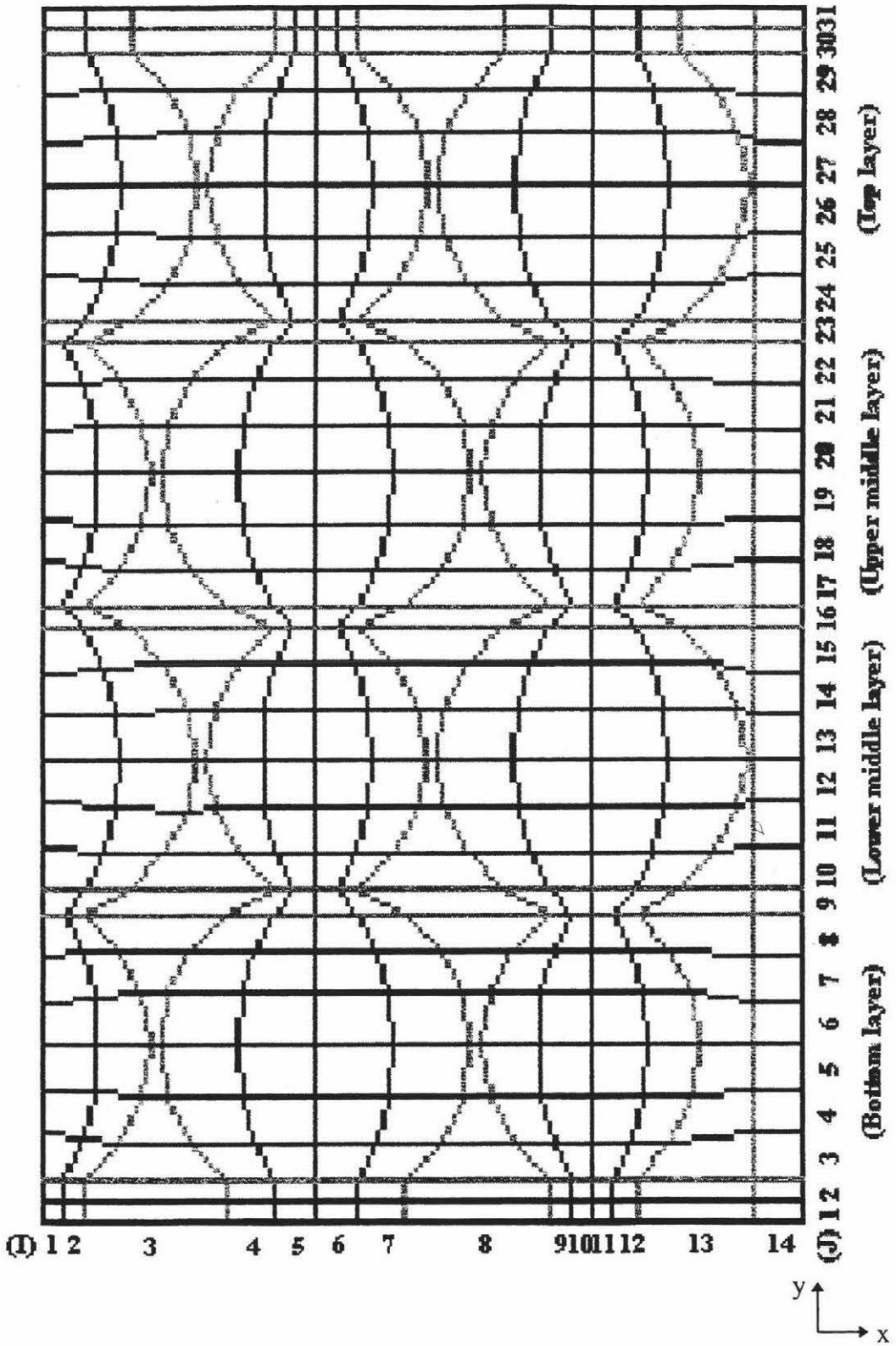

Figure 5.10 Grid for plane K5-K7, K13-K15, K21-K23, K29-K31, K37-K39, K45-K47

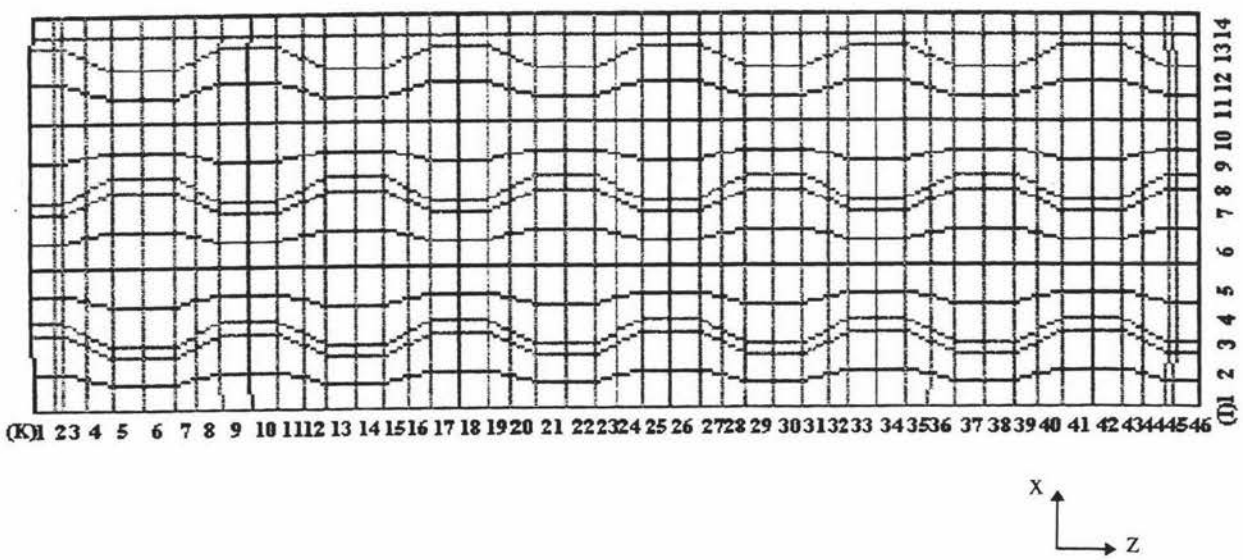

Figure 5.11 Grid for plane J5, J7, J19, J21

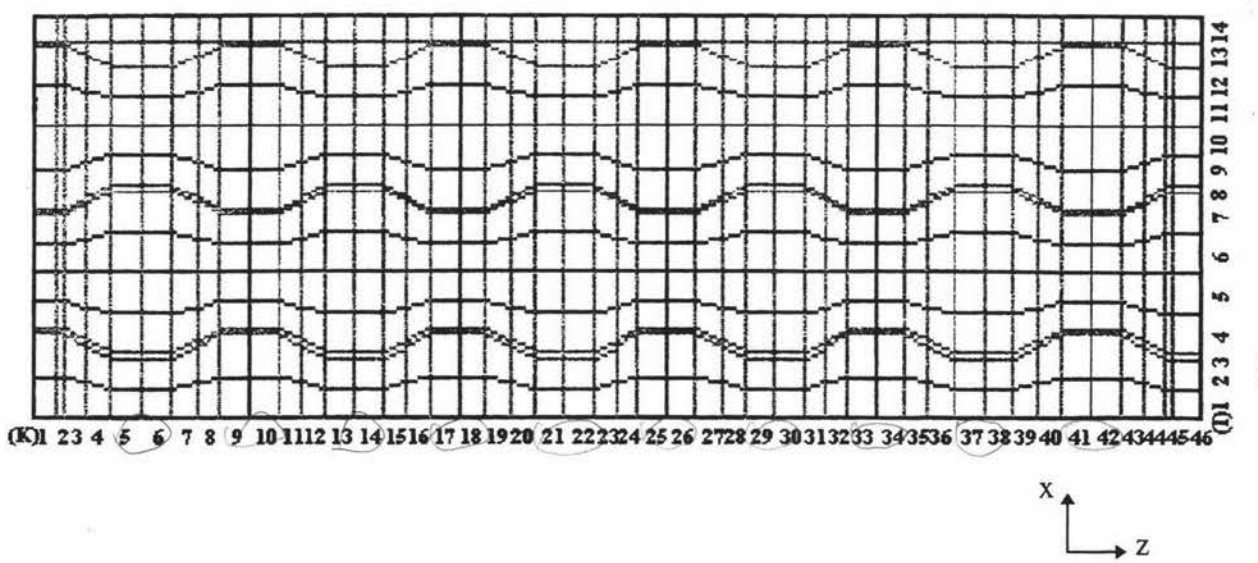

Figure 5.12 Grid for plane J6, J20

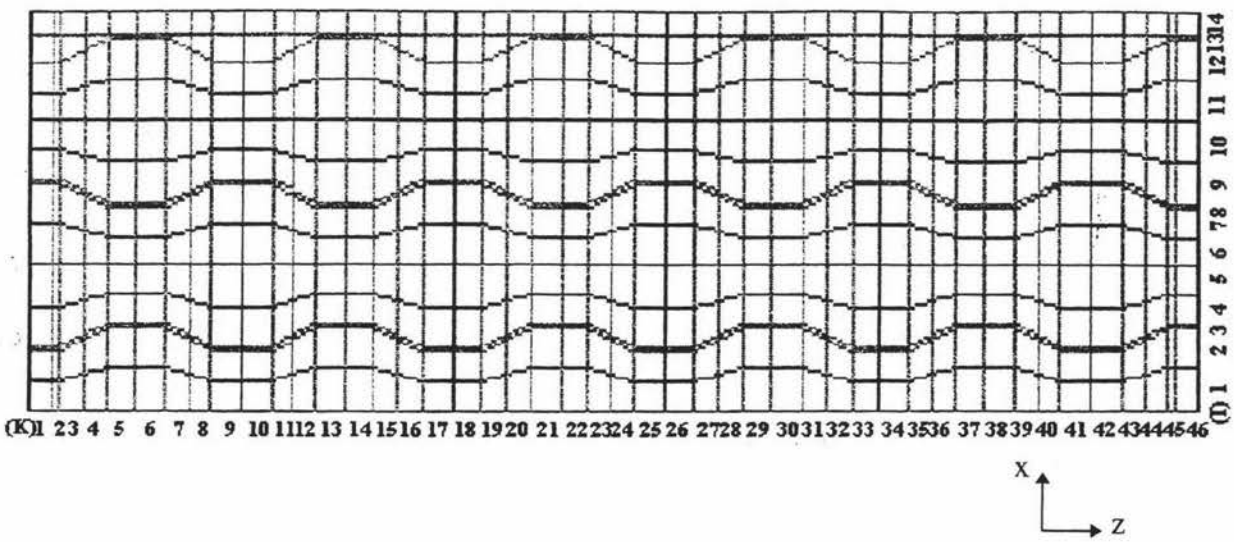

Figure 5.13 Grid for plane J13, J27

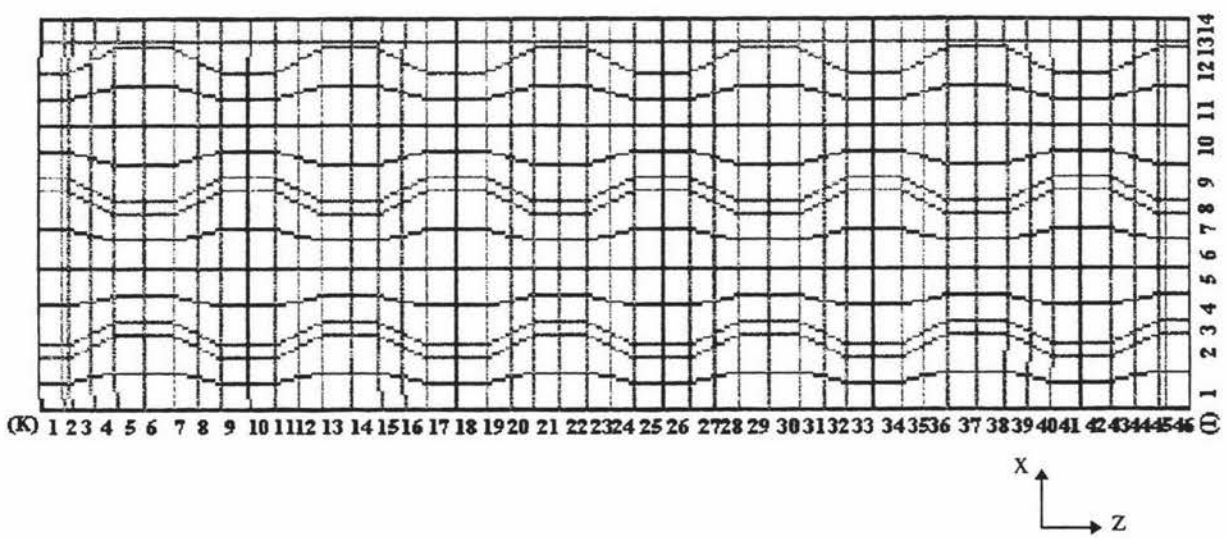

Figure 5.14 Grid for plane J12, J14, J26, J28

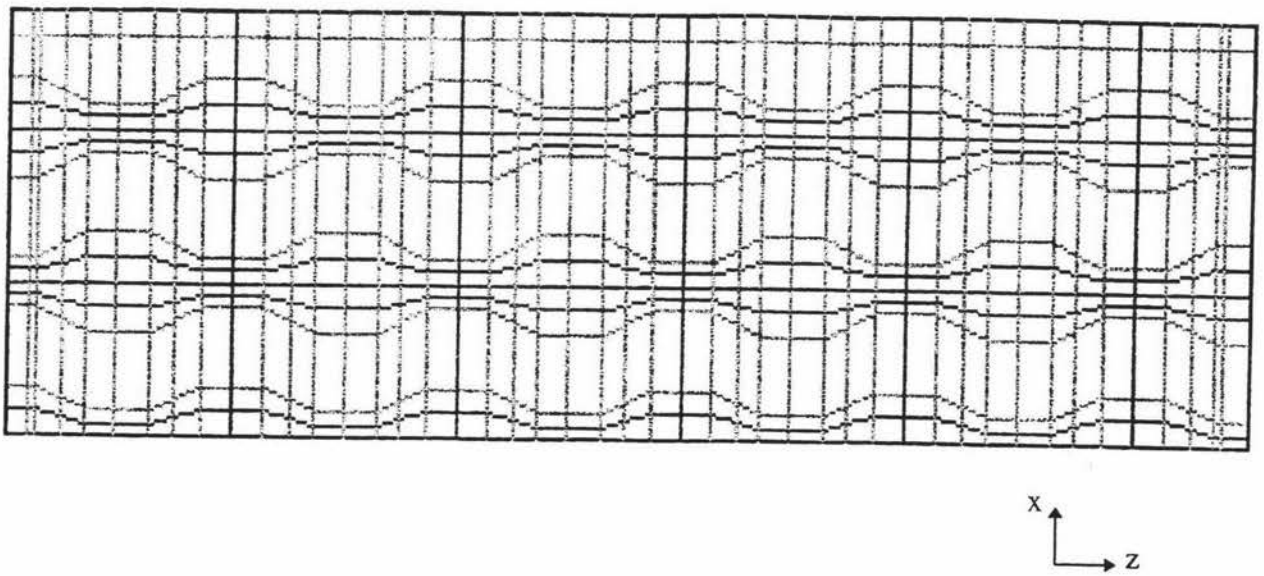

Figure 5.15 Grid for plane J1-J3, J9, J17, J23

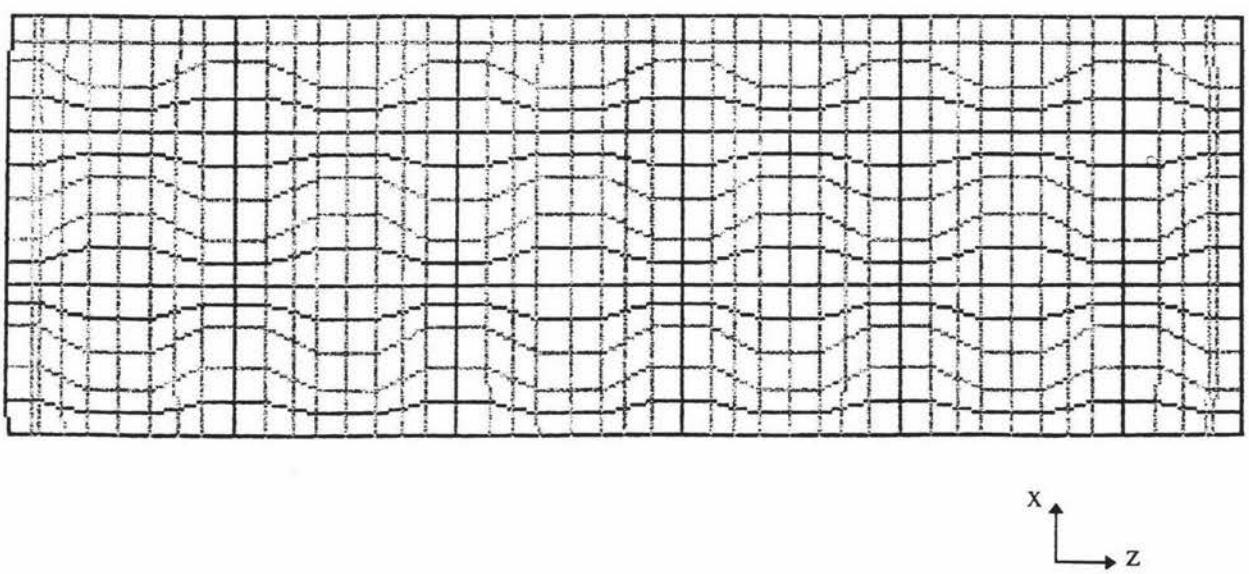

Figure 5.16 Grid for plane J4, J8, J18, J22

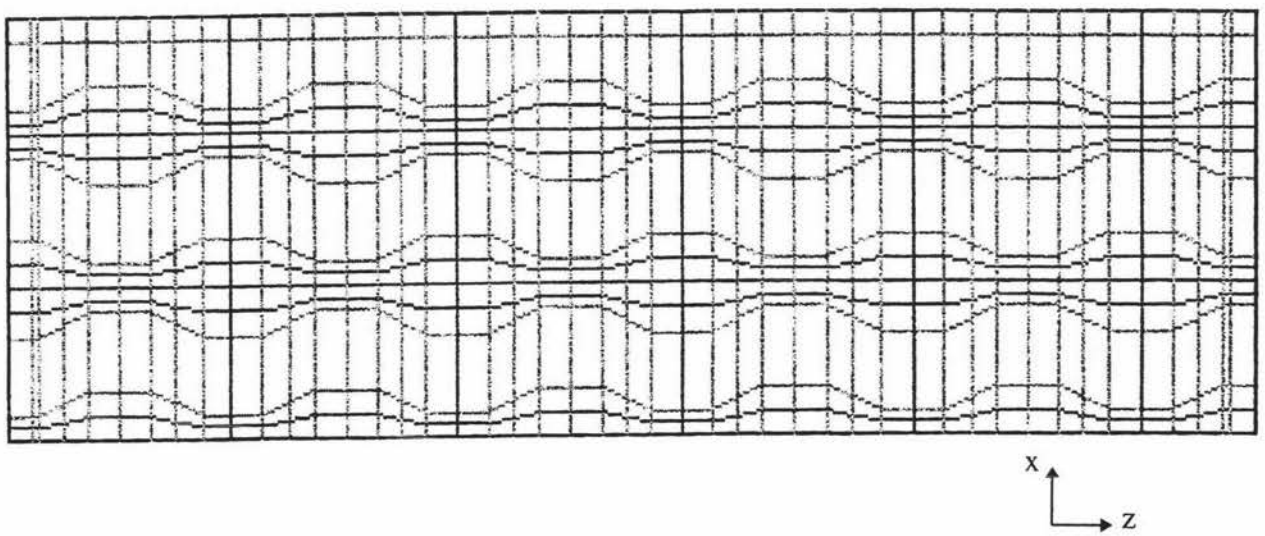

Figure 5.17 Grid for plane J10, J16, J24, J30-J32

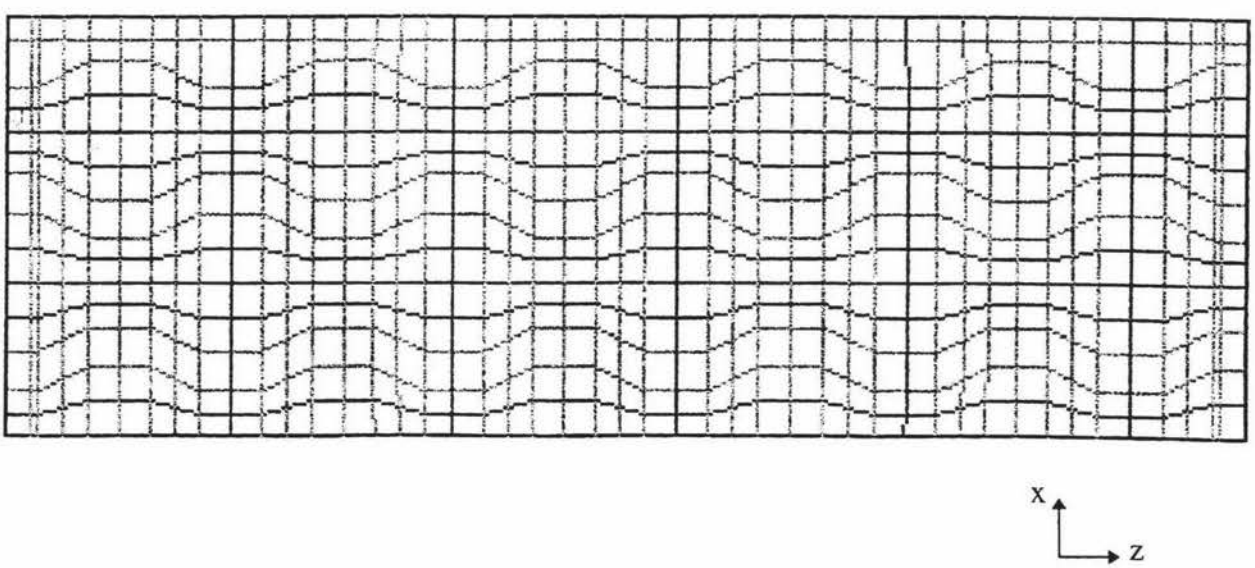

Figure 5.18 Grid for plane J11, J15, J25, J29

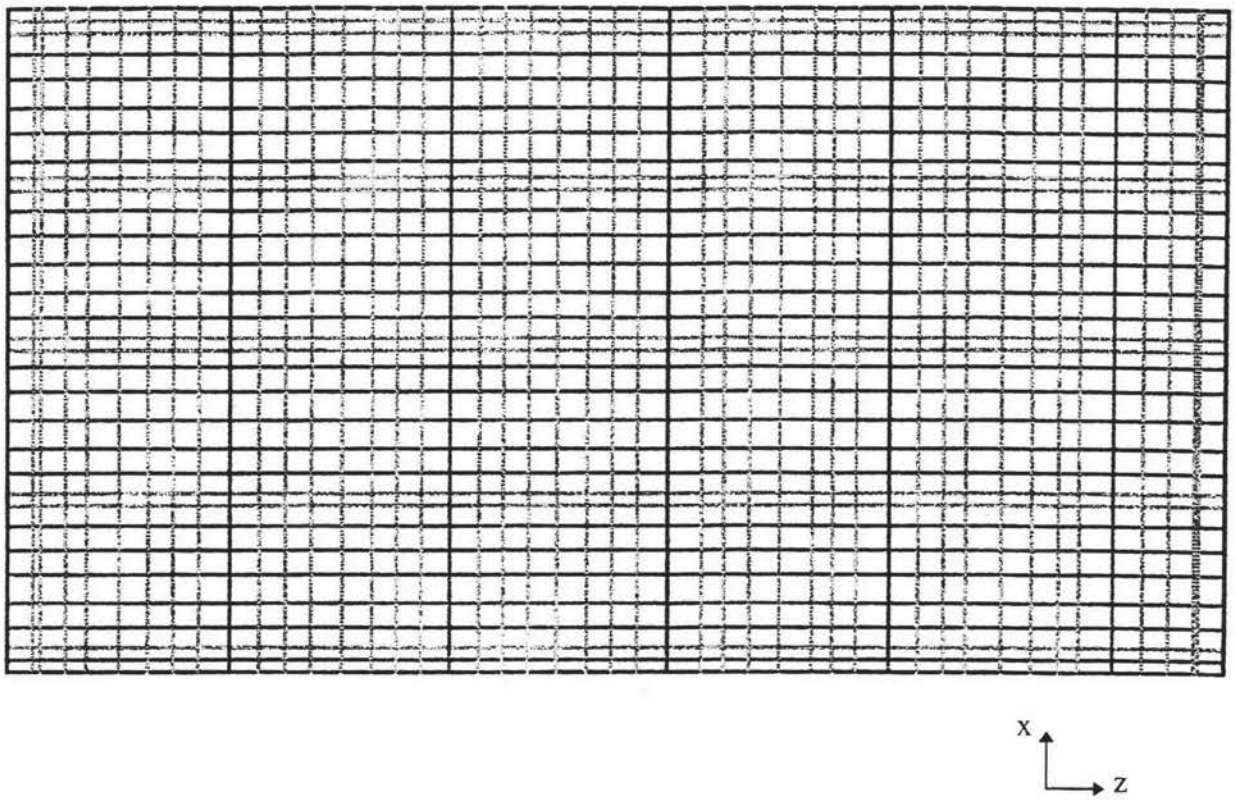

Figure 5.19 Grid for plane I1-I15

Where:

Δt = time interval (s).

V = volume of the control volume (m^3).

The above equation was converted into the following form according to the Gauss's Theorem (Patankar, 1980):

$$\int_V \int_t^{t+\Delta t} \frac{\partial}{\partial t}(\rho\phi)dt\ dv = \int_t^{t+\Delta t} \oint_S (\Gamma grad\phi - \rho \mathbf{u}\phi) \cdot d\mathbf{s}\ dt + \int_t^{t+\Delta t} \int_V Sdv\ dt \qquad (5.4)$$

Where:

S = total surface area of the control volume (m^2).

5.3.2.1 Treatment of convection and diffusion terms

The convection and diffusion term in Equation (5.4) was written in form of integration over the six surfaces of the control volume:

$$\oint_S (\Gamma grad\phi - \rho \mathbf{u}\phi)\cdot d\mathbf{s} = \int_{A_e}[\Gamma_e(\frac{\partial\phi}{\partial x})_e - \rho u_e\phi_e]ds - \int_{A_w}[\Gamma_w(\frac{\partial\phi}{\partial x})_w - \rho u_w\phi_w)ds +$$
$$\int_{A_n}[\Gamma_n(\frac{\partial\phi}{\partial y})_n - \rho v_n\phi_n)ds - \int_{As}[\Gamma_s(\frac{\partial\phi}{\partial y})_s - \rho v_s\phi_s]ds + \qquad (5.5)$$
$$\int_{A_h}[\Gamma_h(\frac{\partial\phi}{\partial z})_h - \rho w_h\phi_h]ds - \int_{A_l}[\Gamma_l(\frac{\partial\phi}{\partial z})_l - \rho w_l\phi_l]ds$$

Where:

A_w	=	west surface area of the control volume(m^2).
A_e	=	east surface area of the control volume(m^2).
A_s	=	south surface area of the control volume(m^2).
A_n	=	north surface area of the control volume(m^2).
A_l	=	low surface area of the control volume(m^2).
A_h	=	high surface area of the control volume(m^2).
u_w	=	velocity component perpendicular to the west surface ($m\cdot s^{-1}$).
u_e	=	velocity component perpendicular to the east surface ($m\cdot s^{-1}$).
v_s	=	velocity component perpendicular to the south surface ($m\cdot s^{-1}$).
v_n	=	velocity component perpendicular to the north surface ($m\cdot s^{-1}$).
w_l	=	velocity component perpendicular to the low surface ($m\cdot s^{-1}$).
w_h	=	velocity component perpendicular to the high surface ($m\cdot s^{-1}$).
ϕ_w	=	value of variable ϕ in the west surface.
ϕ_e	=	value of variable ϕ in the east surface.
ϕ_s	=	value of variable ϕ in the south surface.
ϕ_n	=	value of variable ϕ in the north surface.
ϕ_l	=	value of variable ϕ in the low surface.
ϕ_h	=	value of variable ϕ in the high surface.
Γ_w	=	value of Γ in the west surface.

Γ_e = value of Γ in the east surface.

Γ_s = value of Γ in the south surface.

Γ_n = value of Γ in the north surface.

Γ_l = value of Γ in the low surface.

Γ_h = value of Γ in the high surface.

$(\frac{\partial \phi}{\partial x})_w$ = derivative of ϕ at x direction in the west surface.

$(\frac{\partial \phi}{\partial x})_e$ = derivative of ϕ at x direction in the east surface.

$(\frac{\partial \phi}{\partial y})_s$ = derivative of ϕ at y direction in the south surface.

$(\frac{\partial \phi}{\partial y})_n$ = derivative of ϕ at y direction in the north surface.

$(\frac{\partial \phi}{\partial z})_l$ = derivative of ϕ at z direction in the low surface.

$(\frac{\partial \phi}{\partial z})_h$ = derivative of ϕ at z direction in the high surface.

Considering the ϕ flux per unit area due to both convection and diffusion out of the east surface:

$$J_e = \Gamma_e (\frac{\partial \phi}{\partial x})_e - \rho u_e \phi_e \tag{5.6}$$

Where:

J_e = flux of ϕ per unit area due to convection and diffusion out of the east surface.

If J_e was assumed to prevail the entire east surface, the total flux of ϕ out of the east surface was written:

$$\int_{A_e} [\Gamma_e (\frac{\partial \phi}{\partial x})_e - \rho u_e \phi_e] ds = J_e A_e \tag{5.7}$$

To make further progress, the profile assumptions or interpolation formulae were needed to evaluate the surface values of $(\frac{\partial \phi}{\partial x})_e$ and ϕ_e with the grid-point value ϕ_P and its neighbour point value ϕ_E. The Hybrid Scheme was employed in PHOENICS to provide the proper interpolation formulae. In this scheme a Peclet number was first defined:

$$P_e = \frac{\rho u_e (\delta x)_e}{\Gamma_e} \tag{5.8}$$

Where:

P_e	=	Peclet number between grid point P and its neighbouring point E.
$(\delta x)_e$	=	displacement between grid-point P and its neighbouring point E (m).

The Peclet number indicated how the surface value ϕ_e was affected by the grid point values ϕ_P and ϕ_E. In the limit of zero Peclet number, the pure-diffusion situation occurred, and the ϕ~x variation could be considered as linear. For a large positive value of P_e , the value of ϕ_e remained very close to the upstream value ϕ_P. When the fluid flew in the negative x direction, ϕ_E became the upstream value. Then for a large negative P_e , the value of ϕ_e was very nearly equal to ϕ_E (Patankar, 1980).

The hybrid scheme is a combination of the central-difference scheme and upwind scheme. For the Peclet number range $-2 \le P_e \le 2$, the hybrid scheme was identical with the central-difference scheme which employed the piecewise-linear profile between grid points P and E.

When $-2 \le P_e \le 2$,

$$\phi_e = f_e \phi_E + (1 - f_e)\phi_P \tag{5.9}$$

$$(\frac{\partial \phi}{\partial x})_e = \frac{\phi_E - \phi_P}{(\delta x)_e} \tag{5.10}$$

$$f_e = \frac{(\delta x)_{e+}}{(\delta x)_e} \tag{5.11}$$

$(\delta x)_{e+}$ = displacement between the grid point P and the east surface (m).

f_e = ratio of $(\delta x)_{e+}$ to $(\delta x)_e$.

To substitute Equation (5.6) with Equation (5.9) and (5.10),

When $-2 \leq P_e \leq 2$, $$J_e = (\frac{\Gamma_e}{(\delta x)_e} - \rho u_e f_e)\phi_E - (\frac{\Gamma_e}{(\delta x)_e} - \rho u_e f_e + \rho u_e)\phi_P \quad (5.12)$$

Out of this range the scheme reduced to the upwind scheme in which the diffusion was set equal to zero, and the surface value ϕ_e was taken as the upstream value:

When $Pe < -2$, $$\phi_e = \phi_E \quad (5.13)$$

$$(\frac{\partial \phi}{\partial x})_e = 0 \quad (5.14)$$

To substitute Equation (5.6) with Equation (5.13) and (5.14),

When $Pe < -2$, $$J_e = -\rho u_e \phi_E - (-\rho u_e + \rho u_e)\phi_P \quad (5.15)$$

When $Pe > 2$, $$\phi_e = \phi_P \quad (5.16)$$

$$(\frac{\partial \phi}{\partial x})_e = 0 \quad (5.17)$$

To substitute Equation (5.6) with Equation (5.16) and (5.17),

When $Pe > 2$, $$J_e = -\rho u_e \phi_P \quad (5.18)$$

Summarising the above equations, the following parameter was defined:

$$a_e = \begin{cases} \dfrac{\Gamma_e}{(\delta x)_e} - \rho u_e f_e & when \quad -2 \le P_e \le 2 \\ -\rho u_e & when \quad P_e < -2 \\ 0 & when \quad P_e > 2 \end{cases} \tag{5.19}$$

Where:

a_e = parameter for the east surface.

Equations (5.12), (5.15), (5.18) were written as follows:

$$J_e = a_e \phi_E - (a_e + \rho u_e)\phi_p \tag{5.20}$$

Using the same approach, the ϕ flux per unit area out of the west, north, south, high and low surfaces were derived:

$$J_w = -\Gamma_w (\frac{\partial \phi}{\partial x})_w + \rho u_w \phi_w \tag{5.21}$$

$$J_n = \Gamma_n (\frac{\partial \phi}{\partial y})_n - \rho v_n \phi_n \tag{5.22}$$

$$J_s = -\Gamma_s (\frac{\partial \phi}{\partial y})_s + \rho v_s \phi_s \tag{5.23}$$

$$J_h = \Gamma_h (\frac{\partial \phi}{\partial z})_h - \rho w_h \phi_h \tag{5.24}$$

$$J_l = -\Gamma_l (\frac{\partial \phi}{\partial z})_l + \rho w_l \phi_l \tag{5.25}$$

Where:

J_w = flux of ϕ per unit area due to convection and diffusion out of the west surface.

J_n = flux of ϕ per unit area due to convection and diffusion out of the north surface.

J_s = flux of ϕ per unit area due to convection and diffusion out of the south surface.

J_h = flux of ϕ per unit area due to convection and diffusion out of the high surface.

J_l = flux of ϕ per unit area due to convection and diffusion out of the low surface.

The Peclet numbers related to these surfaces were defined:

$$P_s = \frac{\rho u_s (\delta x)_s}{\Gamma_s} \tag{5.26}$$

$$P_n = \frac{\rho u_n (\delta y)_n}{\Gamma_n} \tag{5.27}$$

$$P_s = \frac{\rho u_s (\delta y)_s}{\Gamma_s} \tag{5.28}$$

$$P_h = \frac{\rho u_h (\delta z)_h}{\Gamma_h} \tag{5.29}$$

$$P_l = \frac{\rho u_l (\delta z)_l}{\Gamma_l} \tag{5.30}$$

Where:

P_w = Peclet number between grid point P and its neighbouring point W.

P_n = Peclet number between grid point P and its neighbouring point N.

P_s = Peclet number between grid point P and its neighbouring point S.

P_h = Peclet number between grid point P and its neighbouring point H.

P_l = Peclet number between grid point P and its neighbouring point L.

$(\delta x)_w$ = displacement between grid point P and its neighbouring point W (m).

$(\delta y)_n$ = displacement between grid point P and its neighbouring point N (m).

$(\delta y)_s$ = displacement between grid point P and its neighbouring point S (m).

$(\delta z)_h$ = displacement between grid point P and its neighbouring point H (m).

$(\delta z)_l$ = displacement between grid point P and its neighbouring point L (m).

The geometric parameters were needed:

$$f_w = \frac{(\delta x)_{w+}}{(\delta x)_w} \tag{5.31}$$

$$f_n = \frac{(\delta y)_{n+}}{(\delta y)_n} \tag{5.32}$$

$$f_s = \frac{(\delta y)_{s+}}{(\delta y)_s} \tag{5.33}$$

$$f_h = \frac{(\delta z)_{h+}}{(\delta z)_h} \tag{5.34}$$

$$f_l = \frac{(\delta z)_{l+}}{(\delta z)_l} \tag{5.35}$$

Where:

$(\delta x)_{w+}$ = displacement between the grid point P and the west surface (m).

$(\delta y)_{n+}$ = displacement between the grid point P and the north surface (m).

$(\delta y)_{s+}$ = displacement between the grid point P and the south surface (m).

$(\delta z)_{h+}$ = displacement between the grid point P and the high surface (m).

$(\delta z)_{l+}$ = displacement between the grid point P and the low surface (m).

f_w = ratio of $(\delta x)_{w+}$ to $(\delta x)_w$.

f_n = ratio of $(\delta y)_{n+}$ to $(\delta y)_n$.

f_s = ratio of $(\delta y)_{s+}$ to $(\delta y)_s$.

f_h = ratio of $(\delta z)_{h+}$ to $(\delta z)_h$.

f_l = ratio of $(\delta z)_{l+}$ to $(\delta z)_l$.

The parameters for calculating the ϕ flux at these surfaces were derived:

$$a_w = \begin{cases} \dfrac{\Gamma_w}{(\delta x)_w} + \rho u_w f_w & when \quad -2 \le P_w \le 2 \\ 0 & when \quad P_w < -2 \\ \rho u_w & when \quad P_w > 2 \end{cases} \tag{5.36}$$

$$a_n = \begin{cases} \dfrac{\Gamma_n}{(\delta y)_n} - \rho v_n f_n & when \quad -2 \le P_n \le 2 \\ -\rho v_n & when \quad P_n < -2 \\ 0 & when \quad P_n > 2 \end{cases} \tag{5.37}$$

$$a_s = \begin{cases} \dfrac{\Gamma_s}{(\delta y)_s} + \rho v_s f_s & when \quad -2 \le P_s \le 2 \\ 0 & when \quad P_s < -2 \\ \rho v_s & when \quad P_s > 2 \end{cases} \tag{5.38}$$

$$a_h = \begin{cases} \dfrac{\Gamma_h}{(\delta z)_h} - \rho w_h f_h & when \quad -2 \le P_h \le 2 \\ -\rho w_h & when \quad P_h < -2 \\ 0 & when \quad P_h > 2 \end{cases} \tag{5.39}$$

$$a_l = \begin{cases} \dfrac{\Gamma_l}{(\delta z)_l} + \rho w_l f_l & when \quad -2 \le P_l \le 2 \\ 0 & when \quad P_l < -2 \\ \rho w_l & when \quad P_l > 2 \end{cases} \tag{5.40}$$

Where:

a_w = parameter for the west surface.

a_n = parameter for the north surface.

a_s = parameter for the south surface.

a_h = parameter for the high surface.

a_l = parameter for the low surface.

The ϕ flux per unit area out of the surfaces of the control volume were written as the following:

$$J_w = a_w\phi_W - (a_w - \rho u_w)\phi_p \tag{5.41}$$

$$J_n = a_n\phi_N - (a_n + \rho v_n)\phi_p \tag{5.42}$$

$$J_s = a_s\phi_S - (a_s - \rho v_s)\phi_p \tag{5.43}$$

$$J_h = a_h\phi_H - (a_h + \rho w_h)\phi_p \tag{5.44}$$

$$J_l = a_l\phi_L - (a_l - \rho w_l)\phi_p \tag{5.45}$$

Similar to the J_e, if J_w, J_n, J_s, J_h, and J_l were assumed to prevail their related surfaces respectively, the total flux of ϕ out of the control volume was written:

$$\oint_S (\Gamma grad\phi - \rho\mathbf{u}\phi)\cdot d\mathbf{s} = J_e A_e + J_w A_w + J_n A_n + J_s A_s + J_h A_h + J_l A_l \tag{5.46}$$

To substitute Equation (5.46) with Equation (5.20), (5.41), (5.42), (5.43), (5.44) and (5.45), the expression for the convection and diffusion term in the integrated general equation was obtained:

$$\oint_S (\Gamma grad\phi - \rho \mathbf{u}\phi)\cdot d\mathbf{s} = a_e A_e \phi_E + a_w A_w \phi_W + a_n A_n \phi_N + a_s A_s \phi_S +$$
$$a_h A_h \phi_H + a_l A_l \phi_L - (a_e A_e + a_w A_w + a_n A_n + a_s A_s + a_h A_h + a_l A_l)\phi_P - \quad (5.47)$$
$$(\rho u_e A_e - \rho u_w A_w + \rho v_n A_n - \rho v_s A_s + \rho w_h A_h - \rho w_l A_l)\phi_P$$

Considering the integrated continuity equation, the Equation (5.4) was reduced to the following form because of no unsteady and source term:

$$\oint_S (\Gamma grad\phi - \rho \mathbf{u}\phi)\cdot d\mathbf{s} = 0 \quad (5.48)$$

For continuity equation values of ϕ and Γ throughout the fluid field were 1 and 0. Combining the Equation (5.47) and (5.48), the continuity equation was converted into the following form:

$$u_e A_e - u_w A_w + v_n A_n - v_s A_s + w_h A_h - w_l A_l = 0 \quad (5.49)$$

Consequently, the Equation (5.47) was simplified to the desired form:

$$\oint_S (\Gamma grad\phi - \rho \mathbf{u}\phi)\cdot d\mathbf{s} = a_e A_e \phi_E + a_w A_w \phi_W + a_n A_n \phi_N + a_s A_s \phi_S +$$
$$a_h A_h \phi_H + a_l A_l \phi_L - (a_e A_e + a_w A_w + a_n A_n + a_s A_s + a_h A_h + a_l A_l)\phi_P \quad (5.50)$$

5.3.2.2 Treatment of source term

Introducing the average value of S over the control volume, the source term in Equation (5.4) was written:

$$\int_V S dv = \overline{S} V \quad (5.51)$$

Where:

$\overline{S}$ = the average value of S over the control volume.

When the source S was dependent on the variable ϕ, linearization for S~ϕ was needed:

$$\overline{S} = S_1 + S_2\phi_p \tag{5.52}$$

Where:

S_1 = assumed constant part of source term.

S_2 = coefficient of ϕ_P in source term.

The S_1 and S_2 were chosen by the following method:

$$\overline{S} = S^* + (\frac{\partial S}{\partial \phi})^*_p(\phi_P - \phi^*_p) \tag{5.53}$$

Where:

ϕ^*_p = the guess value or the previous iteration value of ϕ_P.

S^* = S value calculated from ϕ^*_p .

$(\frac{\partial S}{\partial \phi})^*_p$ = $(\frac{\partial S}{\partial \phi})_p$ value calculated from ϕ^*_p .

Combining Equation (5.52) and (5.53), the S_1 and S_2 were expressed as the following:

$$S_1 = S^* - (\frac{\partial S}{\partial \phi})^*_p\phi^*_p \tag{5.54}$$

$$S_2 = (\frac{\partial S}{\partial \phi})^*_p \tag{5.55}$$

5.3.2.3 Treatment of unsteady term

Time is a one-way co-ordinate, in another word, the present situation is only affected by the past, not by the future. The solution was obtained by marching in time from a given initial distribution of variable ϕ. In a typical 'time step' the task was to find the values of ϕ

at time t+Δt while given the grid-point values of ϕ at time t. For the representation of the unsteady term, the grid point value was assumed throughout the control volume:

$$\int_V \int_t^{t+\Delta t} \frac{\partial}{\partial t}(\rho\phi)dt\ dv = \rho V(\phi_p - \phi_P^0) \tag{5.56}$$

Where:

ϕ_P^0 = value of ϕ_P at previous time step.

The time integration in the convection-diffusion and source terms were dealt with the fully implicit scheme, in which the ϕ value in grid point P was assumed to suddenly change from ϕ_P^0 to ϕ_P at time t, and then stay at ϕ_P over the whole of the time step Δt. The ϕ values at the grid points E, W, N, S, L, and H were handled by the same assumption. Over a relatively large time interval, the fully implicit scheme was considered to be more closer to the reality than others such as the explicit and Crank-Nicolson schemes. With this scheme the large time steps can be applied to the fine spacing grid without obtaining physically unrealistic results. Based on the above assumption, the terms on the right-hand side of the Equation (5.4) were written as the following:

$$\int_t^{t+\Delta t} \oint_S (\Gamma grad\phi - \rho\mathbf{u}\phi)\cdot d\mathbf{s}\ dt + \int_t^{t+\Delta t} \int_V Sdv\ dt = \Delta t(\oint_S (\Gamma grad\phi - \rho\mathbf{u}\phi)\cdot d\mathbf{s} + \int_V Sdv) \tag{5.57}$$

To substitute Equation (5.4) with Equation (5.56) and (5.57),

$$\rho V(\phi_p - \phi_P^0) = \Delta t(\oint_S (\Gamma grad\phi - \rho\mathbf{u}\phi)\cdot d\mathbf{s} + \int_V Sdv) \tag{5.58}$$

5.3.2.4 Treatment of diffusion coefficient

The most diffusion coefficients on the surfaces of control volume were assumed to have the same value as in the grid point because of no significant differences between the

neighbouring grid points. In these cases no special treatment was needed. However, the interpolation was needed for the situation in which Γ varies significantly with the spacing variables. The piecewise linear interpolation may result in physically unrealistic solutions. Other than the arithmetic mean, the harmonic mean of Γ values in two neighbouring points showed more clear physical meaning (Patankar, 1980). The harmonic-mean method was demonstrated by calculation of the Γ value on the east surface of control volume with the grid point P:

$$\Gamma_e = \left(\frac{f_e}{\Gamma_E} + \frac{1-f_e}{\Gamma_P}\right)^{-1} \tag{5.59}$$

Where:

Γ_P = Γ value at the grid point P.

Γ_E = Γ value at the grid point E.

5.3.2.5 Discretisation equation

The discretisation equation for the general differential equation (Equation (4.61)) was derived by substituting Equation (5.58) with Equation (5.50) and (5.52):

$$a_P\phi_P = a_E\phi_E + a_W\phi_W + a_N\phi_N + a_S\phi_S + a_H\phi_H + a_L\phi_L + a_T\phi_T + b_P \tag{5.60a}$$

$$a_P\phi_P = \sum a_{nb}\phi_{nb} + b_P \tag{5.60b}$$

$$a_E = a_e A_e \tag{5.61}$$

$$a_W = a_w A_w \tag{5.62}$$

$$a_N = a_n A_n \tag{5.63}$$

$$a_S = a_s A_s \tag{5.64}$$

$$a_H = a_h A_h \tag{5.65}$$

$$a_L = a_l A_l \tag{5.66}$$

$$a_T = \frac{V\rho}{\Delta t} \tag{5.67}$$

$$b_P = S_1 V \tag{5.68}$$

$$a_P = a_E + a_W + a_N + a_S + a_H + a_L + a_T - S_2 V \tag{5.69}$$

Where:

a_E	=	coefficient for the grid point E in the discretisation equations.
a_W	=	coefficient for the grid point W in the discretisation equations.
a_N	=	coefficient for the grid point N in the discretisation equations.
a_S	=	coefficient for the grid point S in the discretisation equations.
a_H	=	coefficient for the grid point H in the discretisation equations.
a_L	=	coefficient for the grid point L in the discretisation equations.
a_T	=	time coefficient in the discretisation equations.
a_{nb}	=	a_E, a_W, a_N, a_S, a_H, a_L, a_T.
ϕ	=	ϕ_E, ϕ_W, ϕ_N, ϕ_S, ϕ_H, ϕ_L,ϕ_T.
a_P	=	coefficient for the grid point P in the discretisation equations.
b_P	=	coefficient for the source term in the discretisation equations.

5.3.2.6 Treatment of momentum equations and pressure field

The pressure gradient forms a part of the source term in a momentum equation, but originally no direct equation for pressure exits. The pressure field is indirectly specified via the continuity equation, so a pressure equation may be derived from the continuity equation.

the continuity equation, so a pressure equation may be derived from the continuity equation.

As mentioned above, the velocity components were stored at the centre points of the cell faces. The control volumes for the velocity components were staggered on that for the scalars. The staggering for x direction component u was in the x direction only, and v in the y direction, w in the z direction. This layout realised one of main advantages of the staggered grid: the pressure differences between the grid points (with respect to the scalar cells) could be used to calculate the pressure force acting on the control volumes for the velocity components.

The discretisation equations for the velocity components u, v, and w were written as the similar form described in the previous section, but the pressure gradients were not included in the source-term quantities S_1 and S_2.

$$a_{ue}u_e = \sum a_{unb}u_{nb} + b_{ue} + (p_P - p_E)A_e \tag{5.70}$$

Where:

u_e	=	x direction velocity component at centre point of east surface of scalar cell ($m \cdot s^{-1}$).
u_{nb}	=	x direction velocity components at centre points of east surfaces of neighbouring scalar cells ($m \cdot s^{-1}$).
a_{ue}	=	coefficient for u_e in the discretisation equation.
a_{unb}	=	coefficient for u_{nb} in the discretisation equation.
b_{ue}	=	coefficient for the source term in the discretisation equation for u.
p_P	=	pressure at grid point P of the scalar cell ($N \cdot m^{-2}$).
p_E	=	pressure at grid point E of the east neighbouring scalar cell ($N \cdot m^{-2}$).

$$a_{vn}v_n = \sum a_{vnb}v_{nb} + b_{vn} + (p_P - p_N)A_n \tag{5.71}$$

Where:

v_n = y direction velocity component at centre point of north surface of scalar cell ($m \cdot s^{-1}$).

v_{nb} = y direction velocity components at centre points of north surfaces of neighbouring scalar cells ($m \cdot s^{-1}$).

a_{vn} = coefficient for v_n in the discretisation equation.

a_{vnb} = coefficient for v_{nb} in the discretisation equation.

b_{vn} = coefficient for the source term in the discretisation equations for v.

P_N = pressure at grid point E of the east neighbouring scalar cell ($N \cdot m^{-2}$).

$$a_{wh}w_h = \sum a_{wnb}w_{nb} + b_{wh} + (p_P - p_H)A_h \tag{5.72}$$

Where:

w_h = z direction velocity component at centre point of high surface of scalar cell ($m \cdot s^{-1}$).

w_{nb} = z direction velocity components at centre points of high surfaces of neighbouring scalar cells ($m \cdot s^{-1}$).

a_{wh} = coefficient for w_h in the discretisation equation.

a_{wnb} = coefficient for w_{nb} in the discretisation equation.

b_{wh} = coefficient for the source term in the discretisation equations for w.

P_H = pressure at grid point E of the high neighbouring scalar cell ($N \cdot m^{-2}$).

Above equations can not be solved until the pressure field was given or was somehow estimated. An imperfect velocity field was calculated according to a guessed pressure field:

$$a_{ue}u_e^* = \sum a_{unb}u_{nb}^* + b_{ue} + (p_P^* - p_E^*)A_e \tag{5.73}$$

$$a_{vn}v_n^* = \sum a_{vnb}v_{nb}^* + b_{vn} + (p_P^* - p_N^*)A_n \tag{5.74}$$

$$a_{wh}w_h^* = \sum a_{wnb}w_{nb}^* + b_{wh} + (p_P^* - p_H^*)A_h \tag{5.75}$$

Where:

u_e^* = x direction velocity component u_e calculated based on the estimated pressure field ($m \cdot s^{-1}$)

u_{nb}^* = x direction velocity components u_{nb} calculated based on the estimated pressure field ($m \cdot s^{-1}$)

v_n^* = y direction velocity component v_n calculated based on the estimated pressure field ($m \cdot s^{-1}$)

v_{nb}^* = y direction velocity components v_{nb} calculated based on the estimated pressure field ($m \cdot s^{-1}$)

w_h^* = z direction velocity component w_h calculated based on the estimated pressure field ($m \cdot s^{-1}$)

w_{nb}^* = z direction velocity components w_{nb} calculated based on the estimated pressure field ($m \cdot s^{-1}$)

p_P^*, p_E^*, p_N^*, p_H^*

= estimated pressures at the grid points P, E, N, H ($N \cdot m^{-2}$).

The correct pressure p_P, p_E, p_N, and p_L were obtained from:

$$p_P = p_P^* + \Delta p_P \tag{5.76}$$

$$p_E = p_E^* + \Delta p_E \tag{5.77}$$

$$p_N = p_N^* + \Delta p_N \tag{5.78}$$

$$p_L = p_L^* + \Delta p_L \tag{5.79}$$

Where

Δp_P = pressure correction for pressure at grid point P($N \cdot m^{-2}$).

Δp_E = pressure correction for pressure at the neighbouring grid point E ($N \cdot m^{-2}$).

Δp_N = pressure correction for pressure at the neighbouring grid point N ($N \cdot m^{-2}$).

Δp_H = pressure correction for pressure at the neighbouring grid point H ($N \cdot m^{-2}$).

The corresponding velocity corrections were introduced in a similar manner:

$$u_e = u_e^* + \Delta u_e \tag{5.80}$$

$$v_n = v_n^* + \Delta v_n \tag{5.81}$$

$$w_h = w_h^* + \Delta w_h \tag{5.82}$$

Where:

Δu_e = velocity correction for u_e ($m \cdot s^{-1}$).

Δv_n = velocity correction for v_n ($m \cdot s^{-1}$).

Δw_h = velocity correction for w_h ($m \cdot s^{-1}$).

To subtract Equation (5.73) from Equation (5.70),

$$a_{ue}\Delta u_e = \sum a_{unb}\Delta u_{nb} + (\Delta p_P - \Delta p_E)A_e \tag{5.83}$$

To simplify the derivation further, the term $\sum a_{unb}\Delta u_{nb}$ was dropped. This omission, as discussed by Patankar (1980), did not affect the correctness of the converged solution.

$$\Delta u_e = \frac{(\Delta p_P - \Delta p_E)A_e}{a_{ue}} \tag{5.84}$$

Substitute Equation (5.80) with Equation (5.84),

$$u_e = u_e^* + \frac{(\Delta p_P - \Delta p_E)A_e}{a_{ue}} \tag{5.85}$$

Similarly, the velocity components on the other five surfaces of the scalar cell were obtained.

$$u_w = u_w^* + \frac{(\Delta p_W - \Delta p_P)A_w}{a_{uw}} \tag{5.86}$$

$$v_n = v_n^* + \frac{(\Delta p_P - \Delta p_N)A_n}{a_{vn}} \tag{5.87}$$

$$v_s = v_s^* + \frac{(\Delta p_S - \Delta p_P)A_s}{a_{vs}} \tag{5.88}$$

$$w_h = w_h^* + \frac{(\Delta p_P - \Delta p_H)A_h}{a_{wh}} \tag{5.89}$$

$$w_l = w_l^* + \frac{(\Delta p_L - \Delta p_P)A_l}{a_{wl}} \tag{5.90}$$

Where:

u_w = x direction velocity component at centre point of west surface of scalar cell ($m \cdot s^{-1}$).

v_s = y direction velocity component at centre point of south surface of scalar cell ($m \cdot s^{-1}$).

w_l = z direction velocity component at centre point of low surface of scalar cell ($m \cdot s^{-1}$).

u_w^* = x direction velocity component u_w calculated based on the estimated pressure field ($m \cdot s^{-1}$)

v_s^* = y direction velocity component v_s calculated based on the estimated pressure field ($m \cdot s^{-1}$)

w_l^* = z direction velocity component w_l calculated based on the estimated pressure field ($m \cdot s^{-1}$)

Δp_W = pressure correction for pressure at the neighbouring grid point W ($N \cdot m^{-2}$).

Δp_S = pressure correction for pressure at the neighbouring grid point S ($N \cdot m^{-2}$).

Δp_L = pressure correction for pressure at the neighbouring grid point L ($N \cdot m^{-2}$).

a_{uw} = coefficient for u_w in the discretisation equation.

a_{vs} = coefficient for v_s in the discretisation equation.

a_{wl} = coefficient for w_l in the discretisation equation.

Substitute Equation (5.49) (the continuity equation) with Equation (5.85), (5.86), (5.87), (5.88), (5.89), and (5.90), the discretisation equation for pressure correction was obtained.

$$a_P \Delta p_P = a_E \Delta p_E + a_W \Delta p_W + a_N \Delta p_N + a_S \Delta p_S + a_H \Delta p_H + a_L \Delta p_L + b_P \quad (5.91a)$$

$$a_P \Delta p_P = \sum a_{nb} \Delta p_{nb} + b_P \quad (5.91b)$$

$$a_E = \frac{A_e^{\,2}}{a_{ue}} \quad (5.92)$$

$$a_W = \frac{A_w^{\,2}}{a_{uw}} \quad (5.93)$$

$$a_N = \frac{A_n^{\,2}}{a_{vn}} \quad (5.94)$$

$$a_S = \frac{A_s^{\,2}}{a_{vs}} \quad (5.95)$$

$$a_H = \frac{A_h^{\,2}}{a_{wh}} \tag{5.96}$$

$$a_L = \frac{A_l^{\,2}}{a_{wl}} \tag{5.97}$$

$$b_P = u_e^* A_e - u_w^* A_w + v_n^* A_n - v_s^* A_s + w_h^* A_h - w_l^* A_l \tag{5.98}$$

$$a_P = a_E + a_W + a_N + a_S + a_H + a_L \tag{5.99}$$

The above procedure was developed by Patankar and Spalding (1972) and Patankar (1980), and named SIMPLE, which stands for Semi-Implicit Method for Pressure-Linked equations. The important operations, in the order of their execution, were:

(1) Guess the pressure field p^*;
(2) Solve the momentum equations (Equations 5.70-5.72), obtain u^*,v^*, and w^*;
(3) Solve the pressure correction Δp equation (Equation 5.91);
(4) Calculate p by adding Δp to p^* (Equations 5.76-5.79);
(5) Calculate u, v, w from u^*,v^*, and w^* by Equations 5.85-5.90;
(6) Treat the corrected pressure p as a new guessed pressure p^*, return to step (2), and repeat the whole procedure until a converged solution is obtained.

5.3.2.7 Conjugate heat transfer situation

When the boundary between the fluid and solid phases were considered, e.g. apple surfaces, carton walls, the conjugate heat transfer situations occurred in that conduction in the solid and convection in the fluid must both be taken into account. The calculation of separate solutions for the solid and fluid regions would require an involved interative procedure for matching the interface conduction. The harmonic-mean practice for Γ offered a much easier alternative that was described by Patankar (1980).

The problem was solved by using a calculation domain that included both the fluid and solid regions, with the out surface of the solid coinciding with the boundary of the domain. When the velocity equations were solved, Γ for the grid points that fell in the fluid region was made equal to the viscosity of the fluid, while for the grid points lying in the solid region was set equal to a very large number. This ensured that the zero velocity on the out surface of the solid prevailed throughout the solid region, and thus the fluid region experienced the correct boundary condition.

For solving the temperature equation, the true conductivities of the solid and of the fluid were used in their respective regions. The harmonic-mean method was used to obtain thermal conductivity in the interface between the solid and fluid phases (Patankar, 1980). Then the problem was solved as a convection-conduction problem (Equation (4.30) or (4.32)) throughout the entire calculation domain. Since the velocities in the solid were zero, a pure-conduction calculation (Equation (4.35) or (4.36) or 4.37)) was actually performed in the solid region. The temperature distributions in the solid and in the fluid, given by the resulting solution, automatically matched at the solid-fluid interface.

5.4 SOLUTION OF DISCRETISATION EQUATIONS

Considering the discretisation equations for a variable ϕ, the coefficients a_{nb} might be a function of ϕ, then the algebraic equations were not actually linear though they were treated as linear. Furthermore, the equations for ϕ might be linked with the equations for other variables through the coefficients. Therefore iterative methods were applied to solve these equations. These started from a guessed field of ϕ, and the algebraic equations were used to obtain improved field. Successive repetitions of the algorithm finally lead to a solution that was sufficiently close to the correct solution of the algebraic equations. The iterative methods employed by PHOENICS are mainly point-by-point, slabwise and whole-field methods. The point-by-point method is the Gauss-Sedial method in which values of variable are calculated by visiting each grid in a certain order. The method was discarded because of its long converge time. The whole field method was used to solve the algebraic equations for pressure correction and temperature. The slabwise iteration was applied to get the solutions for velocity components (CHAM, 1995).

5.4.1 Solution Procedure

In PHOENICS the iteration was conducted in several levels. For the dependent variables solved in the model, the structure of iteration is described in Figure 5.20. This procedure shows that the pressure correction and temperature were solved in whole field, while the other variables were solved slabwise.

In the slabwise method, the off-slab values of ϕ (ϕ_L, ϕ_H) were treated as temporarily known, then the problem was reduced to the solution, at each slab and for each variable ϕ, of an NX*NY system of 'linear-like' equations. A generalised 2D version of the Tri-Diagonal Matrix Algorithm (TDMA) was applied to solve the equations for each slab (CHAM, 1995).

The whole field solver was operated by a further extension of the 2D TDMA. The whole field solution was used for the pressure correction equation, as this transmitted effects of the flow boundary conditions and blockages rapidly throughout the domain. Because of slight non-linearity in temperature equations the whole field method was preferable for the solution of these equations (CHAM,1995).

5.4.2 Convergence of solution

The residuals are the quantities used in PHOENICS to monitor the convergence procedure. The residual of a cell for a variable is defined as:

$$\varepsilon_P = a_P \phi_P - \sum a_{nb} \phi_{nb} - b_P \qquad (5.100)$$

Where:

ε_p = residual of ϕ in the cell P.

```
Do ISTEP=1, LSTEP                          (time step, unsteady situation only)
    Do ISWEEP=1, LSWEEP                    (sweep)
        Do IZ=1, NZ                        (slabs along z direction)
            Apply previous sweep's pressure and velocity corrections
            Do IC=1, LITC                  (inner iteration, set as 1)
                Solve scalars k and ε
            Enddo
            Solve velocity in order v, u, w
            Construct and store pressure correction sources and coefficients
        Enddo
        Solve and store pressure correction whole field
        Solve and store temperature whole field
    Enddo
Enddo
```

Figure 5.20 Solution procedure

The EARTH can print the normalised whole field residual:

$$Er = \frac{\sum_{p} |\varepsilon_p|}{RESREF(\phi)} \tag{5.101}$$

Where:

Er = normalised whole field residual.

RESREF(ϕ) = user-set reference value for ϕ.

In addition to the normalised residual, a monitoring location (or cell) is selected in the Q1 file. The spot values and residuals of each variable at the monitoring location also can be displayed.

While assessing if a run has converged, there are several guidelines to follow and observe (CHAM, 1995):

- have the values at the monitor point stopped changing?
- have the residuals reached the cut-off point (at which the calculation stops), or reduced by several orders of magnitude in any case?
- have the sums of mass and heat sources printed in the Result file balanced ?

Two devices are applied to achieve or promote convergence. Firstly, a variable can be prevented from overshooting, during the iteration procedure, by prescribing a range of physically realistic values it can take. Secondly, relaxation is a commonly-used device that promotes convergence by slowing down (relaxing) the changes made to the values of the variables during the solution procedure. Two kinds of relaxation are provided by PHOENICS: linear and false time-step relaxation.

When linear relaxation is applied to a variable ϕ, the new value ϕ_{new} for the variable at each cell is taken as:

$$\phi_{new} = \phi_{old} + \alpha(\phi^* - \phi_{old}) \qquad (5.102)$$

Where:

ϕ_{new}	=	new in-store value of ϕ.
ϕ_{old}	=	current in-store value of ϕ.
ϕ^*	=	value of ϕ resulting from the current iteration.
α	=	relaxation factor ($0 < \alpha \leq 1$).

False time-step relaxation is achieved by adding to the RHS of the discretisation equation an extra term, which has the same form as that resulting from the transient term in differential equation if the calculation is transient:

$$a_P\phi_P = \sum a_{nb}\phi_{nb} + b_P + \frac{\rho V_P}{\Delta t_f}(\phi_{old} - \phi_p) \qquad (5.103)$$

Where:

ϕ_p = cell value of ϕ to be computed.

V_P = cell volume.

Δt_f = false time step.

The arrangements of relaxation were specified in section 6.2.2.

5.4.3 PHOENICS Programmes

Initially both Fully-Turbulence k-ε (FTKE) and Low-Reynolds-Number k-ε (LRKE) model were tried in PHOENICS programmes. While using FTKE model, the calculated values of dimensionless distance from the wall y^+ were less than 30, which were outside the suitable range (30-130) for application of wall functions (section 4.6.1.2). Thus, the FTKE model was discarded, only LRKE model was applied to simulate the turbulent flow. Due to time restriction, PHOENICS code for unsteady-state flow situation was not written. All PHOENICS programmes were provided in the attached disk.

Five sets of PHOENICS codes were written in form of Q1 file for three different flow situations, which are summarised in Table 5.4. For steady-state laminar flow, two sets of PHOENICS codes were needed. The first set was applied to solve steady-state velocity field, in which temperature was set as stored variable so that initial temperature field was included in the output file. The second one was employed to obtain unsteady-state temperature field which adopted the output of the previous calculation as its input data. Similarly two programmes were used for steady-state turbulence flow, one for the solution of steady-state velocity and turbulence quantities, and one for unsteady-state temperature. For unsteady-state laminar flow, only one programme was necessary because all variables were solved simultaneously under unsteady state.

Table 5.4 Summary of PHOENICS programmes

Application	PHOENICS programme	Solved variables	Stored variables
Steady-state laminar flow	Code SSL1	u, v, w, p	T
	Code SSL2	T	u, v, w, p
Steady-state turbulent flow	Code SST1	u, v, w, p, k, ε	T
	Code SST2	T	u, v, w, p, k, ε
Unsteady-state laminar flow	Code USL	u, v, w, p, T	
Heat transfer coefficient	Code HTC	u, v, w, p, k, ε, T	

In addition, a programme was written for computing the heat transfer coefficients on the carton external surfaces. The programme simulated turbulent air flow over a solid block in a wind tunnel. The block was set to have the same dimensions as the carton, and to possess the same thermal properties as the carton. The dimensions of the wind tunnel were decided according to that of the environmental tunnel at Centre for Postharvest and Refrigeration Research, Massey University. The experiments for model validation were conducted in the environment tunnel. The heat transfer coefficient for an area of the external solid surface was calculated from the Stanton number and resultant velocity parallel to the surface at the first node next to the area (CHAM, 1995):

$$h = S_t \rho C_p |u_r| \tag{5.104}$$

Where:

h = heat transfer coefficient for an area of external solid surface cell ($W \cdot K^{-1} \cdot m^{-2}$).

S_t = Stanton number at the first grid node (calculated by PHEONICS programme).

u_r = resultant velocity parallel to the surface at the first grid node (calculated by PHOENICS programme) ($m \cdot s^{-1}$).

C_p = air specific heat capacity under constant pressure ($J \cdot K^{-1} \cdot kg^{-1}$).

ρ = air density ($kg \cdot m^{-3}$)

Average heat transfer coefficients for front, rear and side surfaces were calculated by averaging the coefficient for each area.

CHAPTER 6: SIMULATION RESULTS

6.1 INTRODUCTION

Carton inlet velocity was set as 0.5 m/s which is typical in commercial coolstore operation. Consequently a set of input parameters for the model was determined. The PHOENICS programmes were run in a Digital AlphaStation 4/233 with 64MB of RAM, which has a 64-bit CPU and runs at 233 MHz. Three sets of temperature and velocity predictions were obtained after running the programmes for steady-state laminar flow (Code SSL1 and SSL2), steady-state turbulent flow (Code SST1 and SST2), and unsteady-state laminar flow (Code USL).

6.2 MODEL INPUT DATA

The model input data consisted of the values set for boundary and initial conditions, properties of air and solid materials, relaxation factors, and length of time step.

6.2.1 Initial and Boundary Conditions

Table 6.1 shows the initial conditions of flow field. At the beginning of simulation, the flow field was assumed to be static. For the sake of computation, very small values were used to represent zero initial values.

Table 6.2 provides the values needed to specify boundary conditions. Inflow conditions specified two carton front inlets. Other carton vents were assumed to be fixed-pressure boundaries. Heat transfer coefficients for the carton external surfaces were computed by Code HTC, in which air flow outside the carton was assumed to be turbulent with velocity in the environment tunnel set as 3.0 m/s. Wall-type boundaries were handled internally by PHOENICS, so no input data were necessary for this kind of boundaries.

Table 6.1 Input data for initial conditions

Variable	Initial value	Note
Temperature of air and solid materials (^{0}C)	20.0	
Air velocity component u ($m \cdot s^{-1}$)	1.0×10^{-9}	
Air velocity component v ($m \cdot s^{-1}$)	1.0×10^{-5}	
Air velocity component w ($m \cdot s^{-1}$)	1.0×10^{-3}	
Turbulence kinetic energy k ($J \cdot kg^{-1}$)	1.0×10^{-10}	Turbulence flow only
Dissipation rate of turbulence kinetic energy ε ($J \cdot kg^{-1} \cdot s^{-1}$)	1.0×10^{-10}	Turbulence flow only

Table 6.2 Input data for boundary conditions

Boundary	Variable	Value	Note
Inflow boundaries	Fixed mass flow rate ($kg \cdot s^{-1}$)	0.6465	
	air velocity component w ($m \cdot s^{-1}$)	0.5	
	air velocity components u, v ($m \cdot s^{-1}$)	0.0	
	air temperature T (^{0}C)	0.5	
	turbulence kinetic energy k ($J \cdot kg^{-1}$)	0.00125	Turbulence flow only
	dissipation rate of turbulence kinetic energy ε ($J \cdot kg^{-1} \cdot s^{-1}$)	0.00121	Turbulence flow only
Outflow boundaries	Fixed pressure ($N \cdot m^{-2}$)	1.013×10^{5}	
Carton external surfaces	Heat transfer coefficient for front surface ($W \cdot m^{-2} \cdot K^{-1}$)	8.6	Air velocity in the tunnel was set as 3.0 $m \cdot s^{-1}$
	Heat transfer coefficient for side surfaces ($W \cdot m^{-2} \cdot K^{-1}$)	15.3	
	Heat transfer coefficient for rear surface ($W \cdot m^{-2} \cdot K^{-1}$)	3.9	

6.2.2 Relaxation arrangement

Relaxation methods and related parameters were selected by trial-and-error approach. Several sets of parameters were tried until convergent solutions were obtained. Very small relaxation factors and false-time steps had to be used for reaching convergent solutions. Table 6.3 gives the relaxation arrangement.

Table 6.3 Relaxation arrangement

Variable	Relaxation Method	Relaxation factor or false time step	Note
Velocity components	False-time-step	3.75×10^{-3}	
Pressure	Linear	5×10^{-2}	
Temperature	Linear	0.35	
Turbulence kinetic energy	False-time-step	3.75×10^{-3}	Turbulence flow
dissipation of turbulence kinetic energy	False-time-step	3.75×10^{-3}	Turbulence flow
turbulence viscosity	Linear	0.35	Turbulence flow

6.2.3 Thermal Properties

Air thermal properties were taken as those at 0 ^{0}C and 1 atmosphere pressure. Due to modification in the dimensions of carton and trays (section 5.2.1.2), adjusted properties were used. Because the trays do not make full contact with carton top and bottom, the carton top and bottom walls were assumed to be made up of 3 mm thick cardboard and 2 mm thick air layer. Table 6.4 shows the thermal properties used in the model.

6.2.4 Time Step

Four time steps were applied in PHOENICS code SSL1 to simulate precooling process under steady-state laminar flow condition. Figure 6.1 shows the differences between predicted apple centre temperature adopting 30-second time step and that by using other

three time steps. No significant variations were observed among the predictions using 30-second, 60-second and 120-second time steps. Therefore 120 second was chosen as the time step for all relevant programmes.

Table 6.4 Thermal Properties (Sources: ASHRAE, 1993; Amos, 1995; Kothandranaman & Subermanyan, 1977)

Material	Properties	Value	
Air	Density	1.293	$kg \cdot m^{-3}$
	Kinematic viscosity	1.328×10^{-5}	$m^2 \cdot s^{-1}$
	Specific heat	1005	$J \cdot kg^{-1} \cdot K^{-1}$
	Thermal conductivity	0.02442	$W \cdot m^{-1} \cdot K^{-1}$
Apple	Density	830	$kg \cdot m^{-3}$
	Specific heat	3650	$J \cdot kg^{-1} \cdot K^{-1}$
	Thermal conductivity	0.42	$W \cdot m^{-1} \cdot K^{-1}$
Carton	Density	310	$kg \cdot m^{-3}$
	Density (adjusted for side walls)	186	$kg \cdot m^{-3}$
	Density (adjusted for top and bottom walls)	186	$kg \cdot m^{-3}$
	Specific heat	1700	$J \cdot kg^{-1} \cdot K^{-1}$
	Thermal conductivity	0.048	$W \cdot m^{-1} \cdot K^{-1}$
	Thermal conductivity (adjusted for side walls)	0.08	$W \cdot m^{-1} \cdot K^{-1}$
	Thermal conductivity (adjusted for top and bottom walls)	0.03581	$W \cdot m^{-1} \cdot K^{-1}$
Tray	Density	930	$kg \cdot m^{-3}$
	Density (adjusted)	372	$kg \cdot m^{-3}$
	Specific heat	1300	$J \cdot kg^{-1} \cdot K^{-1}$
	Thermal conductivity	0.13	$W \cdot m^{-1} \cdot K^{-1}$
	Thermal conductivity (adjusted)	0.325	$W \cdot m^{-1} \cdot K^{-1}$

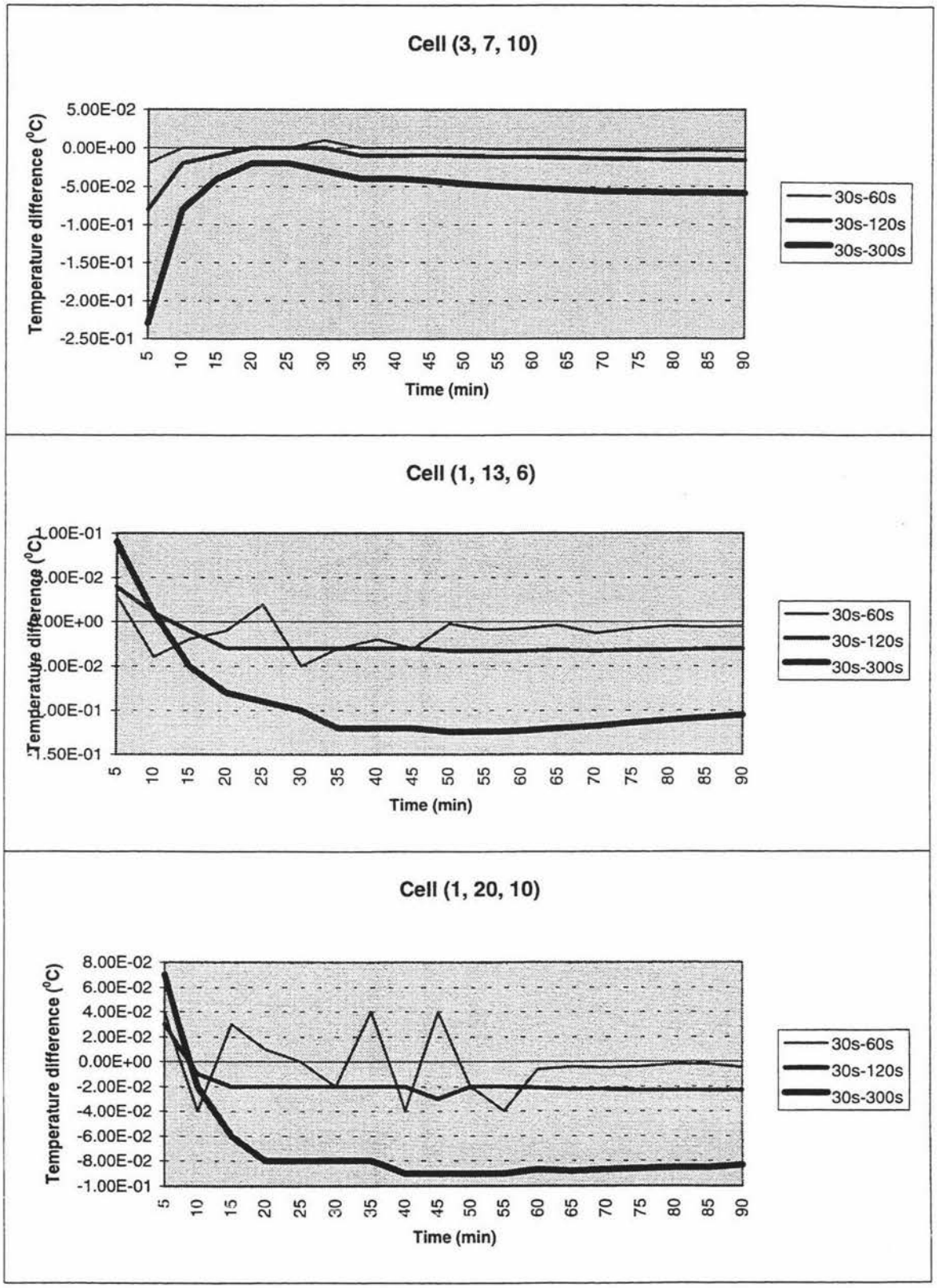

30s-60s: temperature predicted using 30s time step - temperature predicted using 60s time step
30s-120s: temperature predicted using 30s time step - temperature predicted using 120s time step
30s-300s: temperature predicted using 30s time step - temperature predicted using 300s time step

Figure 6-1 Differences in temperature predicted using different time steps

6.3 PARAMETERS FOR CONVERGENCE MONITORING

As outlined in section 5.3.2, when the whole field residual for a variable ϕ is less than a reference value REFSEF(ϕ), the solution for this variable stops. REFSEF (ϕ) was set by PHOENICS internally. Convergence criteria also include situations of mass and heat balance, which are specified by net sums of air volume fraction and temperature in Q1 files. Table 6.5 shows programme running times and the parameters used for convergence monitoring while running the above programmes. It took much longer to run the programme for unsteady-state laminar flow.

Table 6.5 Programme running time and convergence-related parameters

Flow condition	Steady-state laminar		Steady-state turbulent		Unsteady-state laminar
Programme	SSL1	SSL2	SST1	SST2	USL
Running time (hour)	7.0	6.3	7.1	1.5	91.2
RESREF (p)	1.571×10^{-6}	—	1.560×10^{-6}	—	2.009×10^{-6}
RESREF (u)	3.068×10^{-7}	—	3.139×10^{-7}	—	3.112×10^{-6}
RESREF (v)	4.686×10^{-7}	—	4.707×10^{-7}	—	5.769×10^{-6}
RESREF (w)	1.955×10^{-7}	—	1.855×10^{-7}	—	1.950×10^{-6}
RESREF (k)	—	—	3.086×10^{-9}	—	—
RESREF (ε)	—	—	4.360×10^{-8}	—	—
RESREF (T)	—	1.270×10^{-2}	—	5.443×10^{-2}	1.302×10^{-1}
Positive sum of R	2.151×10^{-3}	—	2.151×10^{-3}	—	2.151×10^{-3}
Negative sum of R	-2.151×10^{-3}	—	-2.151×10^{-3}	—	-2.151×10^{-3}
Net sum of R	1.397×10^{-9}	—	1.863×10^{-9}	—	2.701×10^{-8}
Positive sum of T	—	5.912×10^{2}	—	2.365×10^{2}	5.912×10^{-2}
Negative sum of T	—	-5.941×10^{2}	—	-2.366×10^{2}	-5.979×10^{-2}
Net sum of T	—	-2.928	—	-1.103	-6.671

Note: R = volume fraction; T = temperature.

6.4 SIMULATION RESULTS AND DISCUSSION

6.4.1 Predicted Air Flow Patterns

Figures 6.2 and 6.3 show the steady-state laminar and turbulent air flow patterns in the four layers within the carton. Figures 6.4, 6.5 and 6.6 give unsteady-state air flow patterns after 1, 4 and 12-hour cooling. Figures 6.7 compares air velocity components in different positions within the carton through 12-hour cooling, that were calculated for steady-state laminar, steady-state turbulent, and unsteady-state laminar flows. The positions of cells and layers were specified in Figures 5-8 - 5-12.

Considering all three flow conditions, it can be observed that predicted air velocities in the top and bottom were much smaller than those in the middle layers. The uneven air flow distribution can be attributed to different resistance to air flow in different layers. The canton inlets were in the middle of the carton from which air can directly pass the middle layers with relatively small resistance, but air flow had to overcome the large resistance resulting from the narrow gaps between trays and carton wall to enter the top and bottom layers.

Very similar air flow patterns were found while comparing the predictions for steady-state laminar and turbulent flow, although the predicted average velocities under turbulent condition seem slightly higher than under laminar conditions. The reasons for the similarity may be that almost all flow motions occur in a low-velocity range (0 - 1.15 m/s) and within near-wall regions.

From comparison between the predictions for steady-state and unsteady-state laminar flows, we can find the effects of buoyancy force. At the beginning of cooling, the unsteady-state flow velocities in bottom and lower middle layers were higher than that of steady-state flow, while the unsteady-state flow velocities in the top layer was lower, and in the upper middle layer, the velocity differences between unsteady-state and steady-state flows were found much smaller. As cooling process continued, the velocities predicted by unsteady-state laminar programme approached those predicted by steady-state

programme. This was mainly due to the decrease in buoyancy force resulting from reduction of temperature difference throughout the cooling process.

In the middle layers, the air velocities calculated under unsteady-state laminar condition approached the values of steady-state laminar flow much faster than that in the top and bottom layers. This can be attributed to faster cooling and strong effect of forced convection, which make the effect of natural convection less significant.

When comparing the predicted unsteady-state laminar flow patterns in three times of cooling, it can be found that the change in flow patterns throughout cooling was negligible. Moreover, the predicted unsteady-state laminar flow patterns were very similar to that of steady-state laminar flow.

6.4.2 Temperature Predictions

Figures 6.8 - 6.10 and 6.14 show temperature profiles of air, apple centres, carton and trays predicted for steady-state laminar, steady-state turbulent and unsteady-state flows. Figure 6.11 - 6.13 illustrate temperature contours in four layers of the carton under these three flow conditions.

Considering temperature predictions for all three types of flows, the predicted temperature in the upper middle layer dropped with the fastest rate, because the largest amount of cooled air was introduced. The lowest cooling rates occurred in the bottom layer due to the smallest amount of air passing through. The temperature differences between air and fruit were much clearer in the middle layers than in the top and bottom layers. The cooling rates of the apples close to the inlets were much faster than the others, since they were cooled by the medium with the lowest temperature. The predicted temperature of the fruit near the carton walls was also lower than those in the middle of the carton, due to the cooling effect of air flow outside the carton.

Comparing temperature predictions for steady-state laminar and turbulent flows, almost identical temperature contours were observed. Temperature under turbulent condition

dropped slightly faster in several positions than that under laminar conditions. This can be explained by higher predicted velocities for turbulent flow (section 6.4.1).

Very similar temperature contours were also found between steady-state and unsteady-state laminar flows. Cooling rates predicted for unsteady-state flow were slightly faster than that for steady-state flow, especially in the bottom layer, since the effects of natural convection were introduced in unsteady-state flow simulation, which enhances heat transfer within the carton.

By comparing the temperature profiles under three flow conditions, it may be concluded that the differences among these predictions are negligible.

6.4.3 Summary

The predicted air flow patterns in steady-state laminar and unsteady-state turbulent laminar flow were very similar. For the unsteady-state laminar flow, the effects of the change in flow patterns on heat transfer were small, and can be considered negligible. Therefore it is reasonable to adopt steady-state laminar programmes instead of unsteady-state programme for modelling of air flow patterns in ventilated cartons.

The CFD model required less input data, and presented more detailed predictions than other types of models. The model enables us to predict velocity and temperature distribution within the carton, which is crucial in studying the effects of packaging and cooling conditions on product cooling rate. By modifying the grid and input data, the model can be applied to examine air flow patterns and cooling rates under different package structures (locations of vents, dimensions of carton and trays, etc.) and cooling conditions.

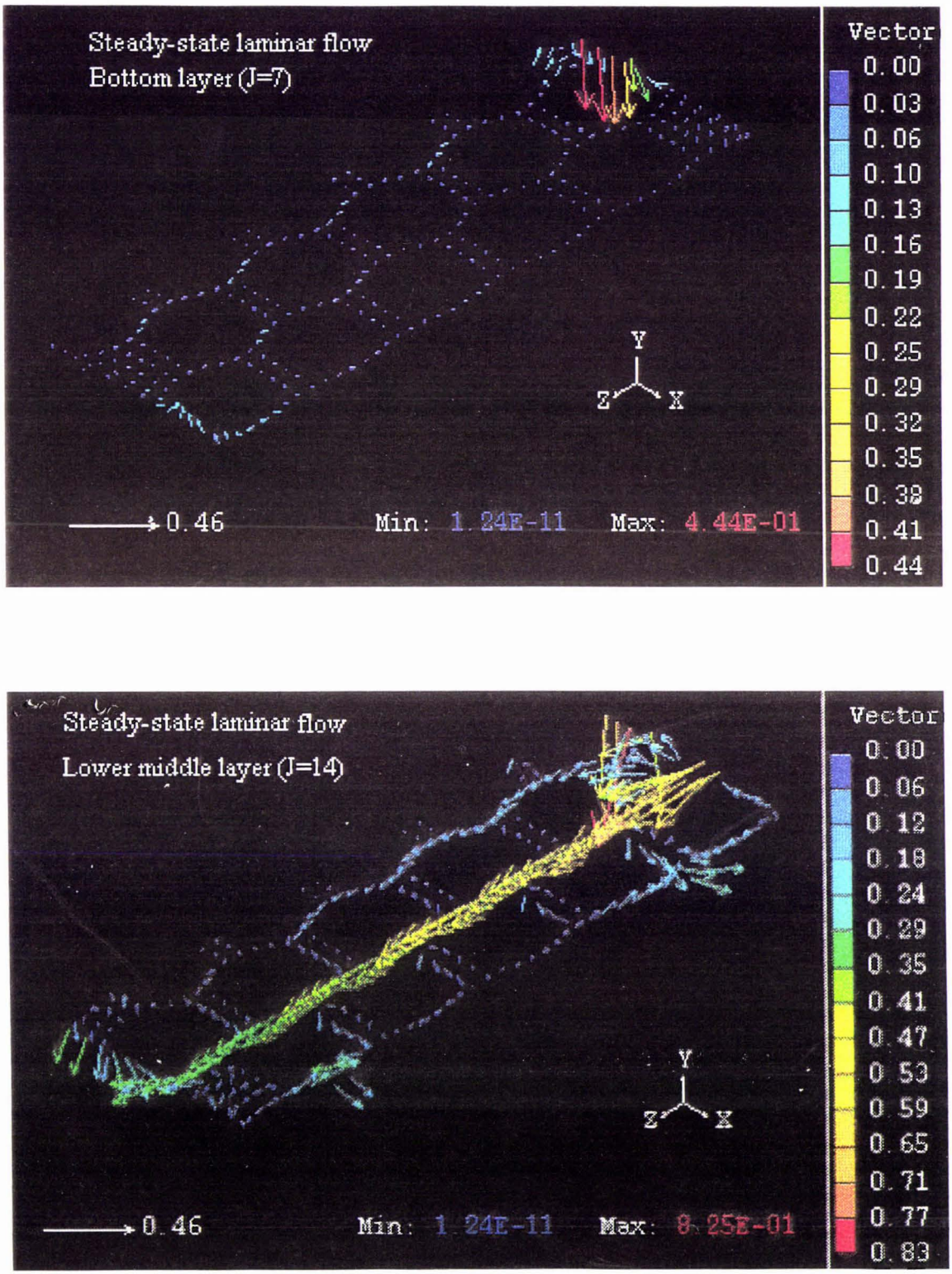

Figure 6.2 Predicted steady-state laminar air flow pattern

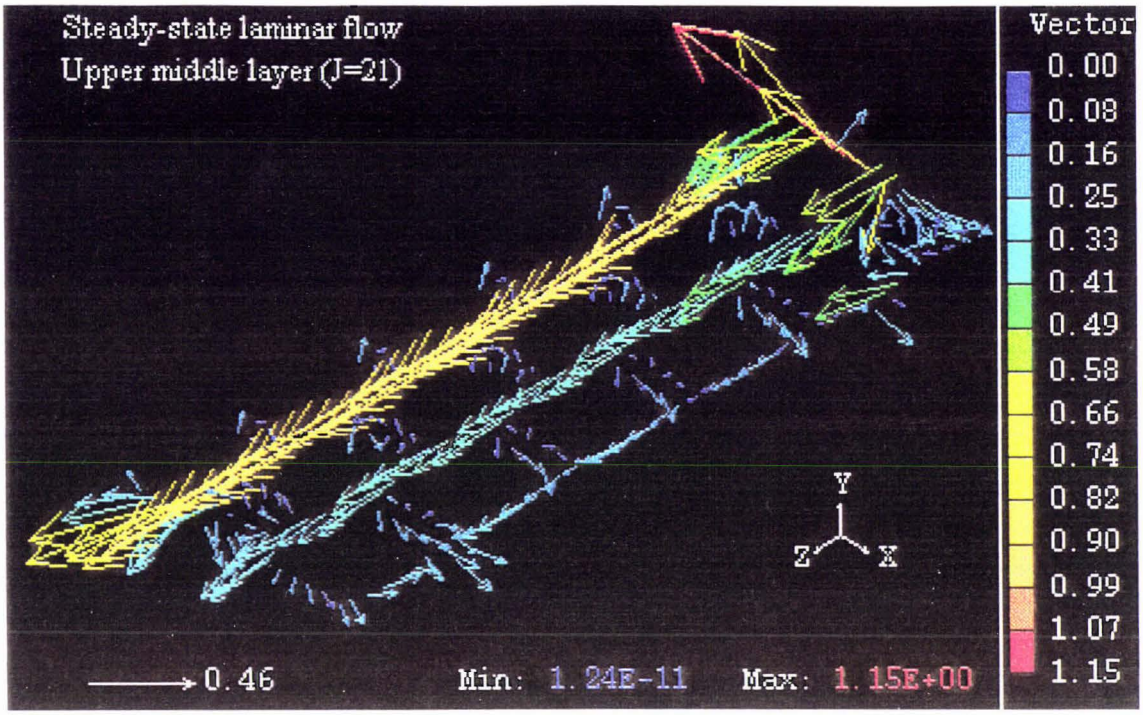

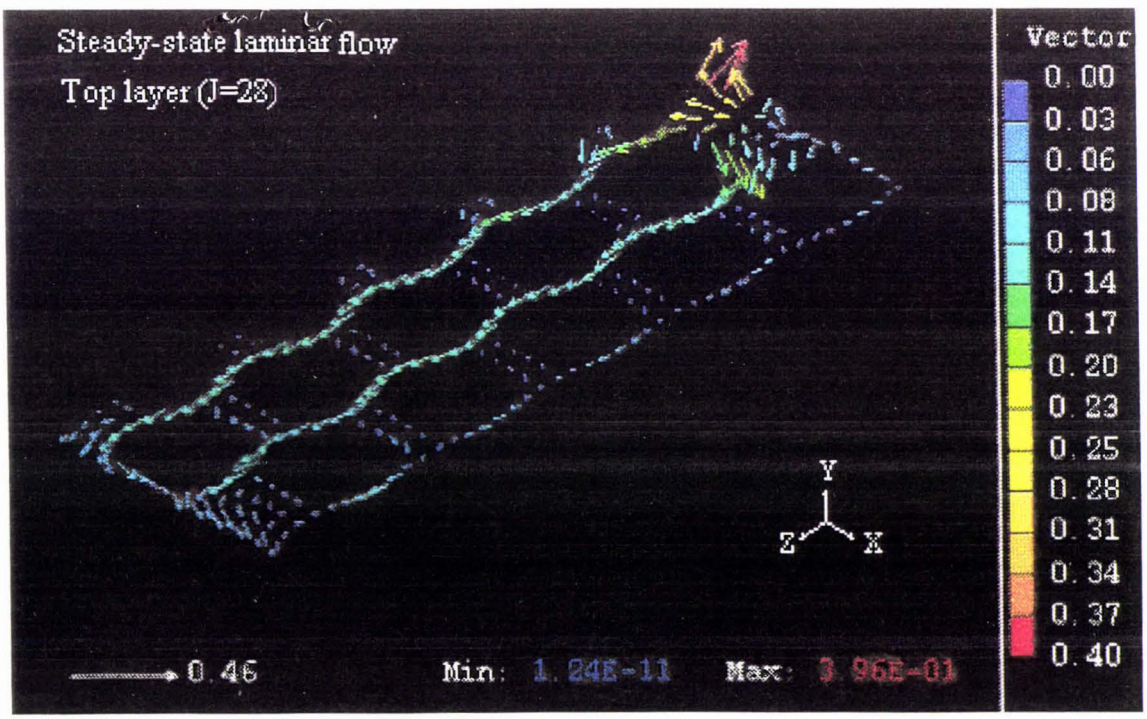

Figure 6.2 (continued) Predicted steady-state laminar air flow pattern

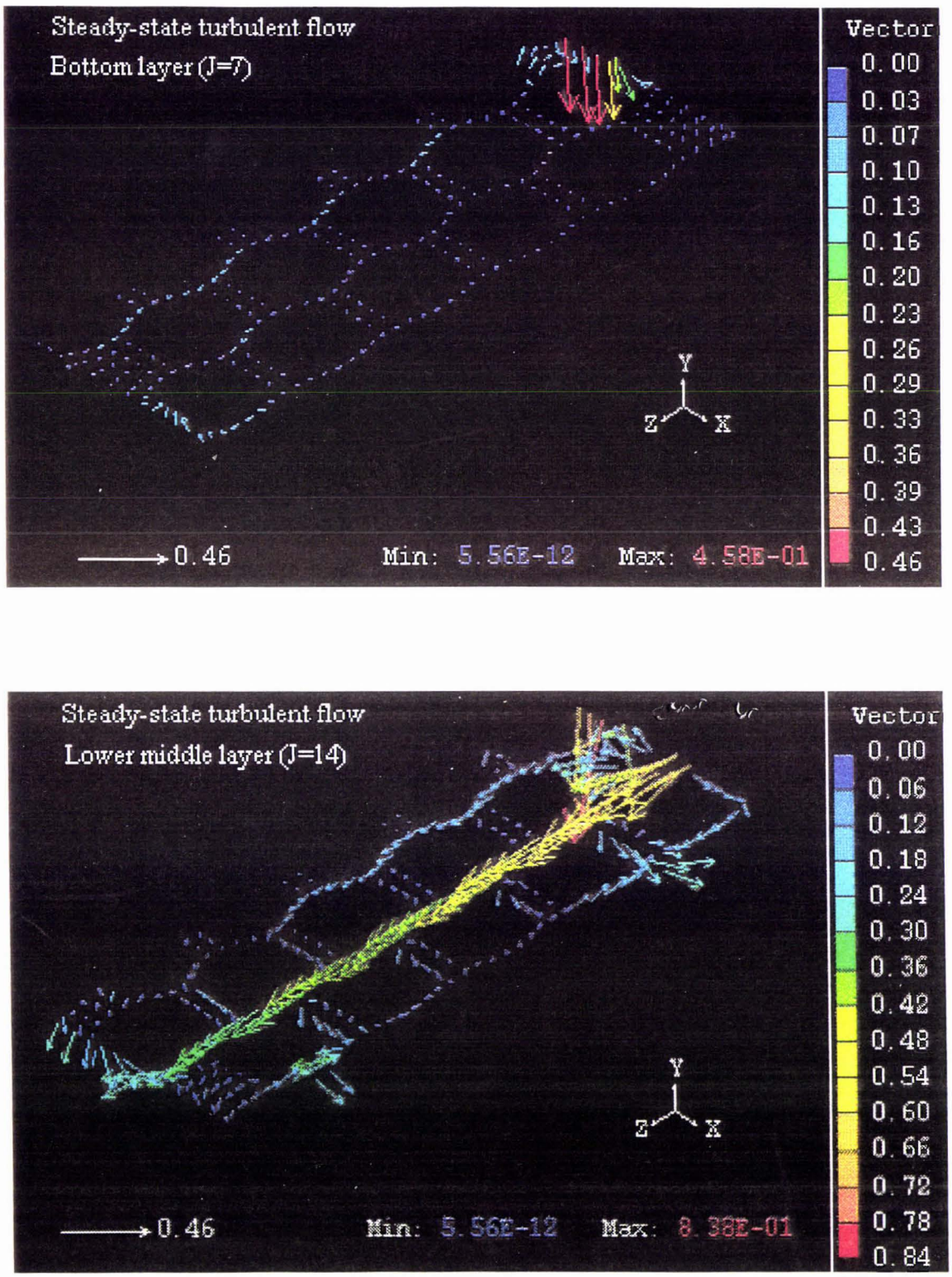

Figure 6.3 Predicted steady-state turbulent air flow pattern

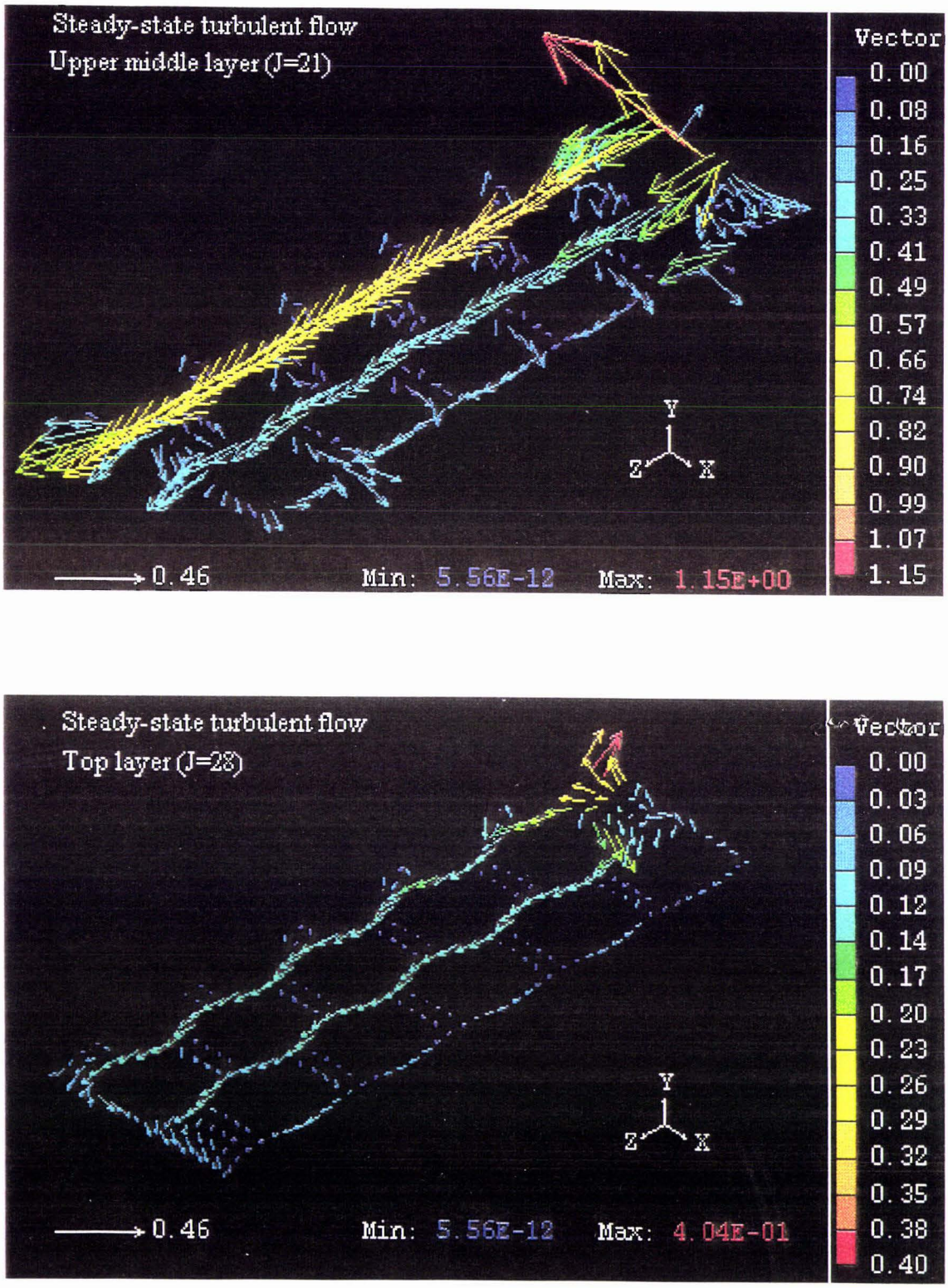

Figure 6.3 (continued) Predicted steady-state turbulent air flow pattern

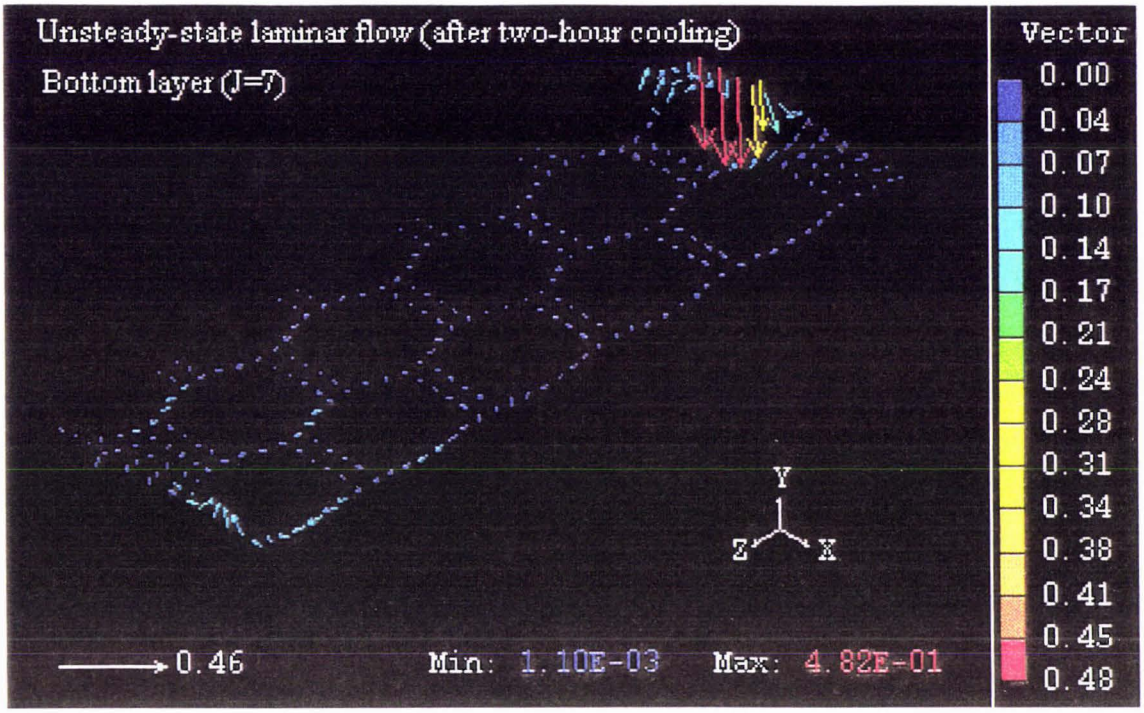

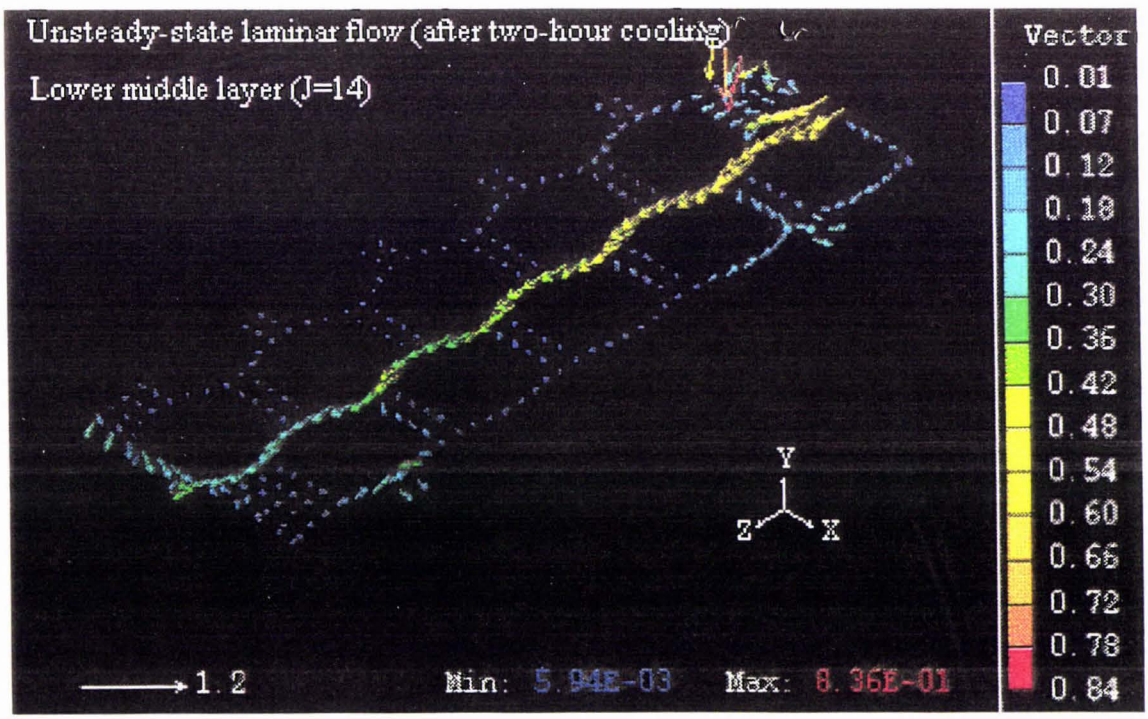

Figure 6.4 Predicted unsteady-state laminar air flow pattern after one-hour cooling

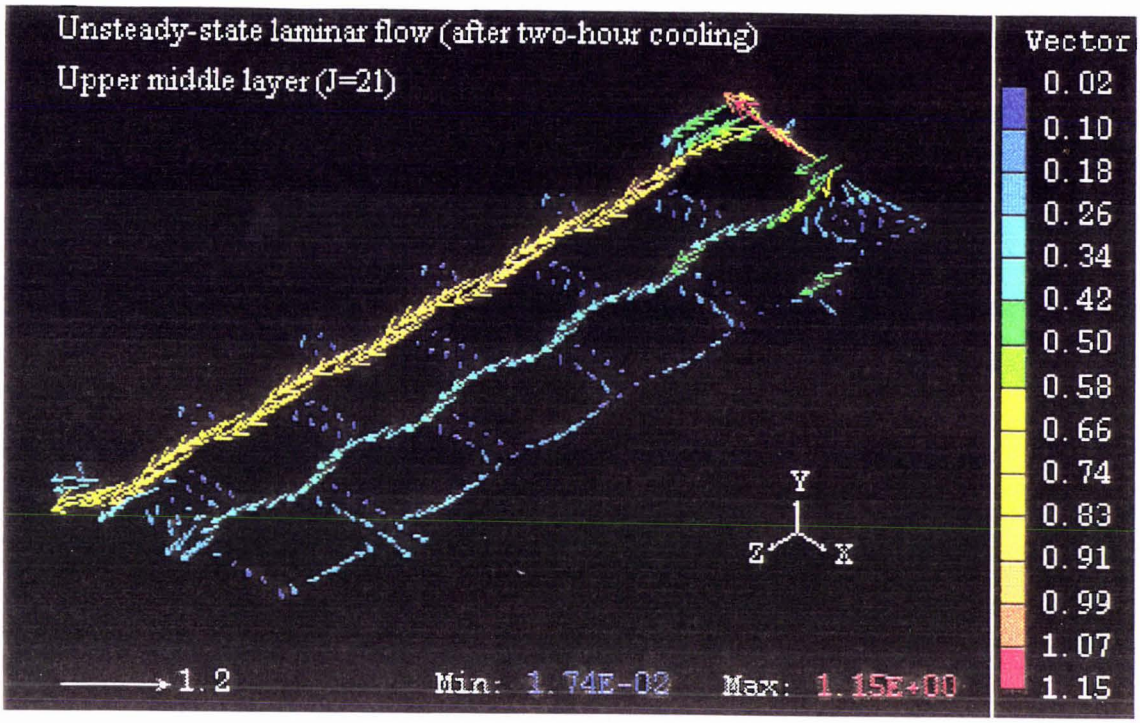

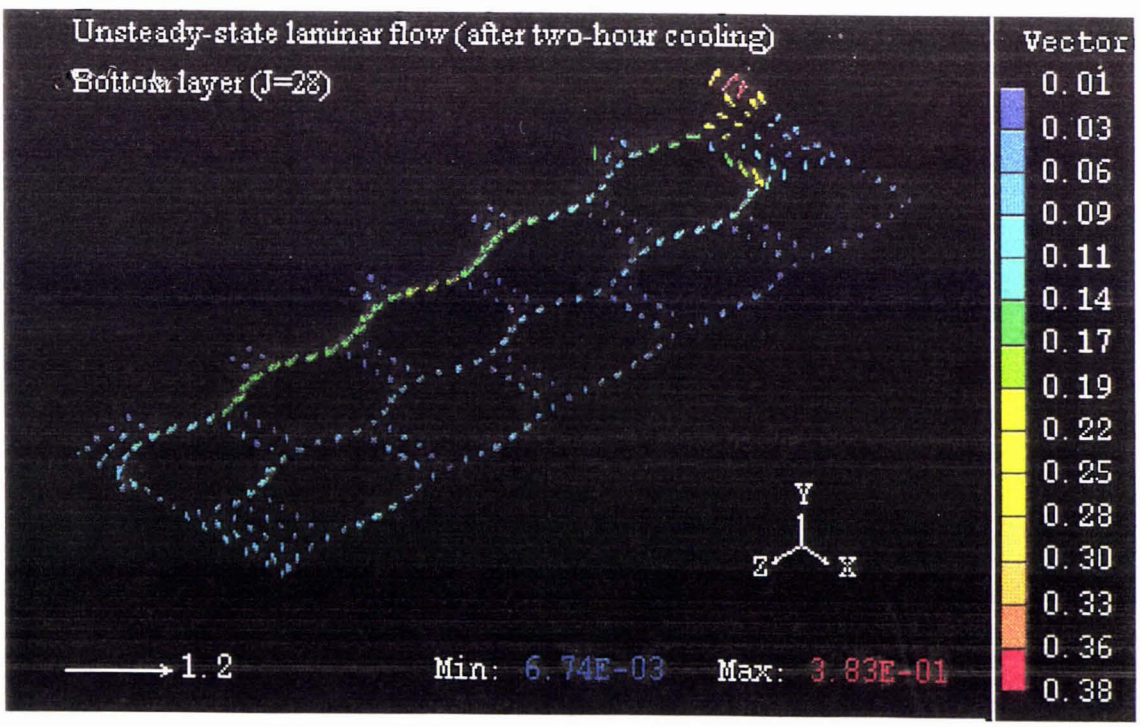

Figure 6.4 (continued) Predicted unsteady-state laminar air flow pattern after one-hour cooling

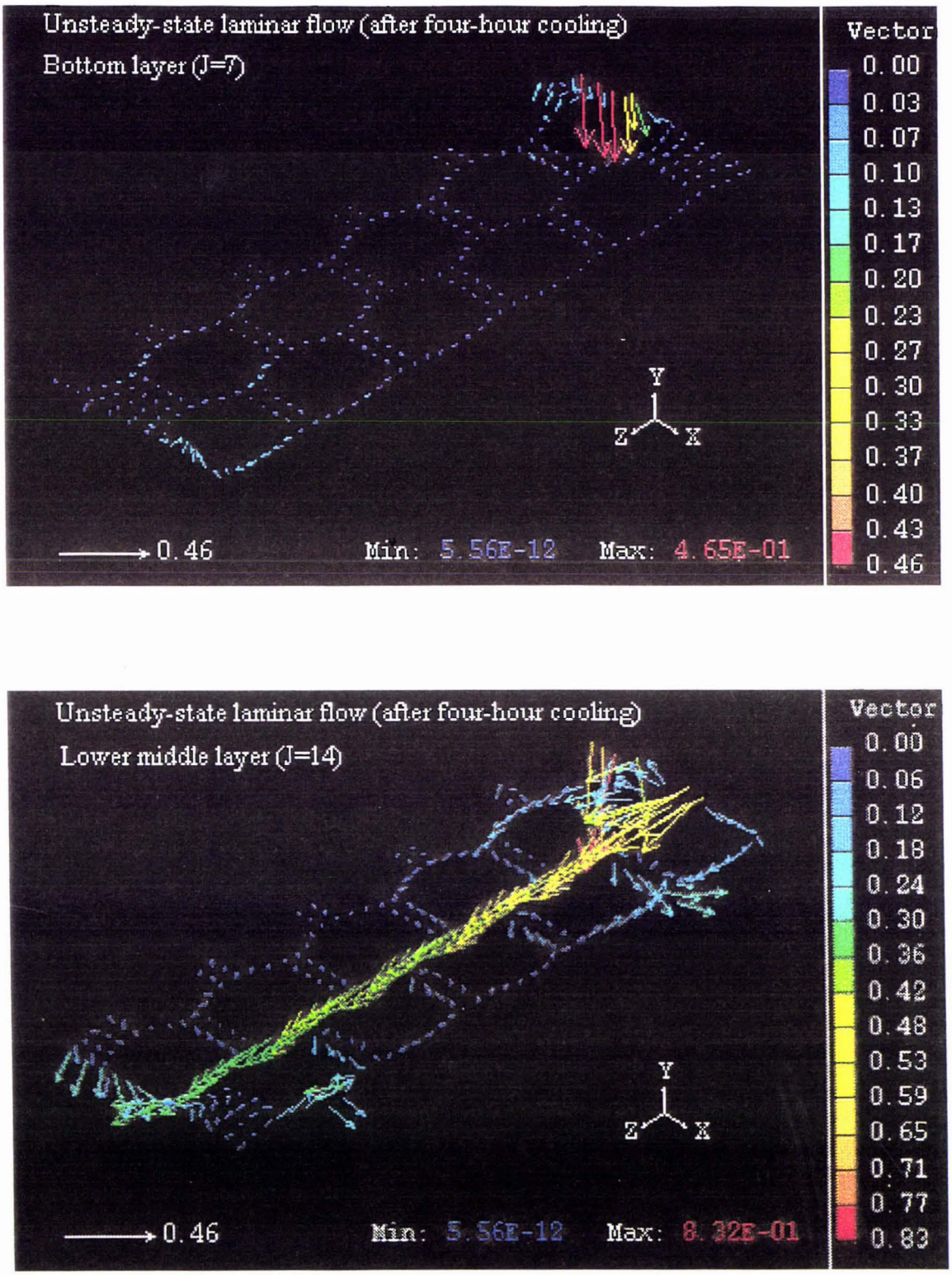

Figure 6.5 Predicted unsteady-state laminar air flow pattern after four-hour cooling

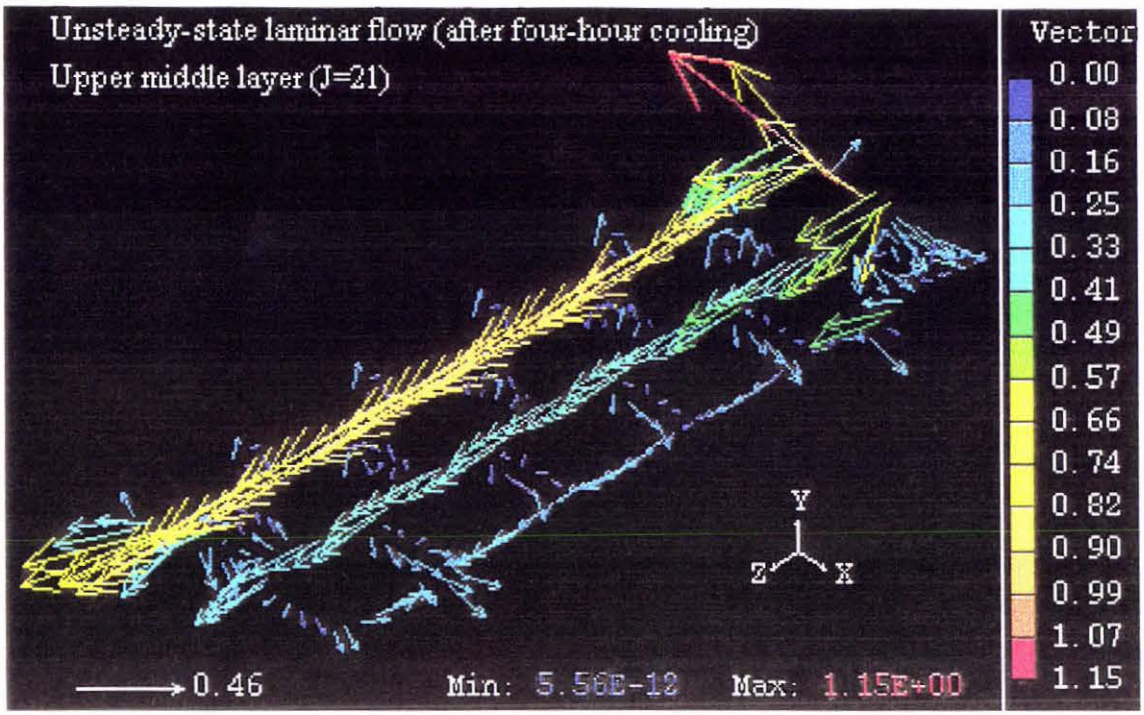

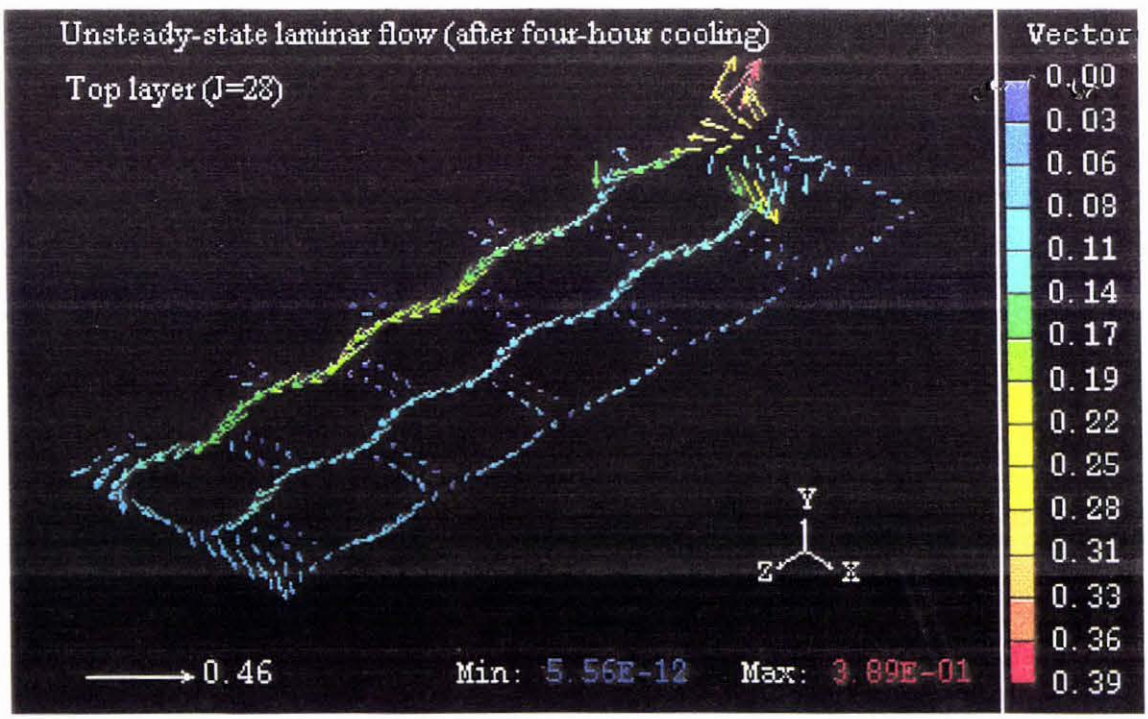

Figure 6.5 (continued) Predicted unsteady-state laminar air flow pattern after four-hour cooling

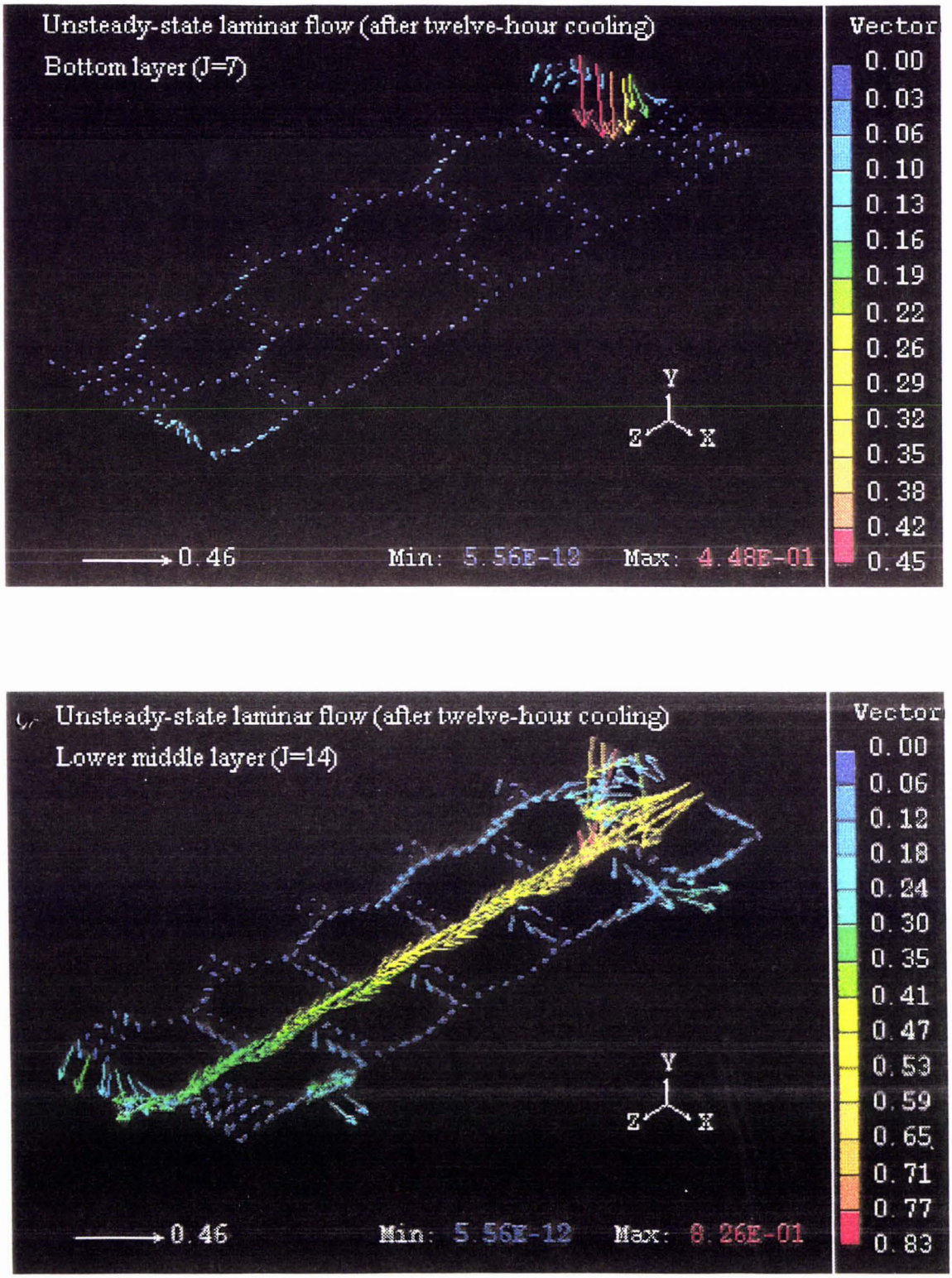

Figure 6.6 Predicted unsteady-state laminar air flow pattern after twelve-hour cooling

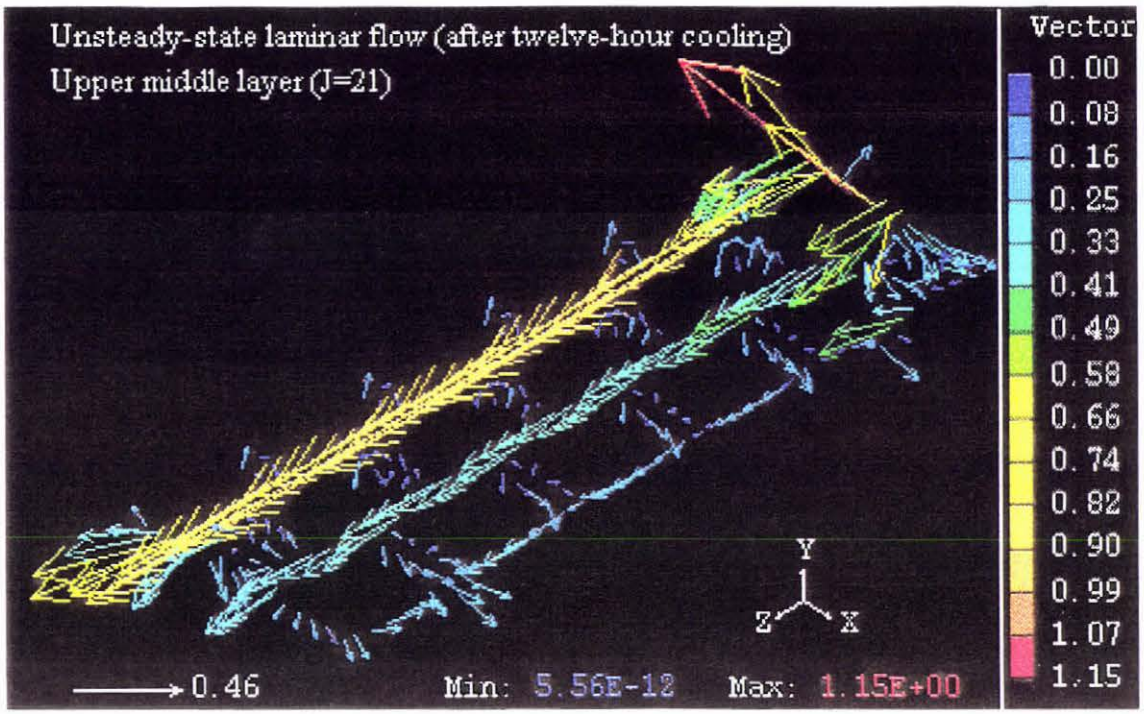

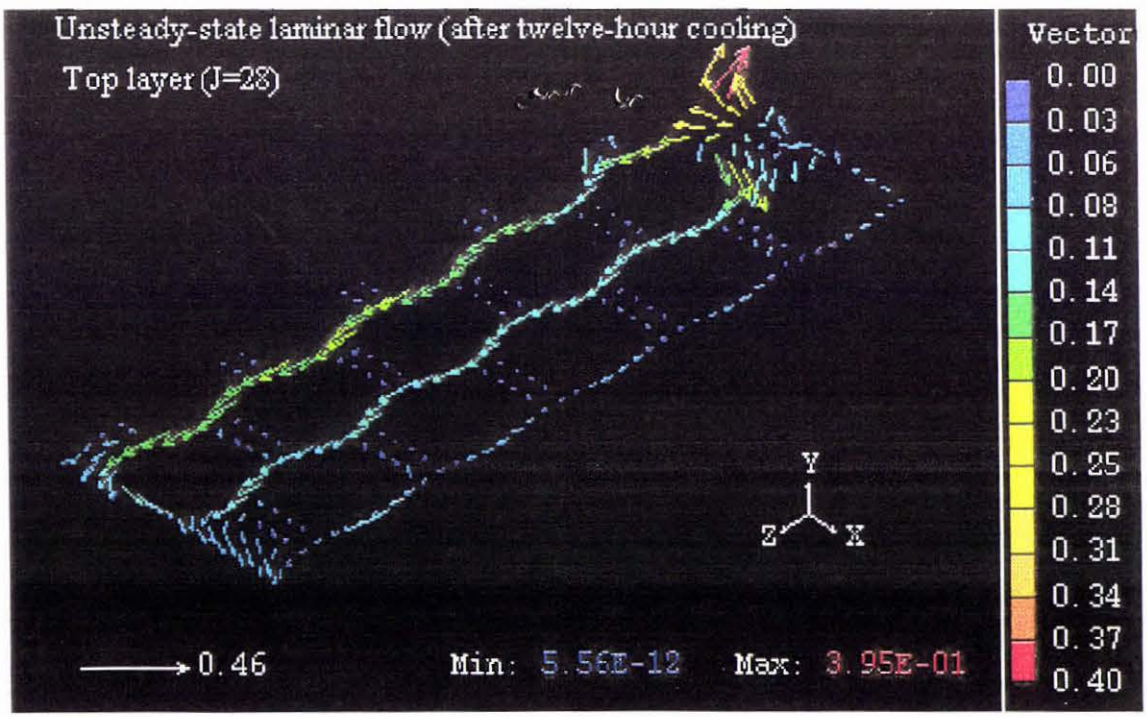

Figure 6.6 (continued) Predicted unsteady-state laminar air flow pattern after twelve-hour cooling

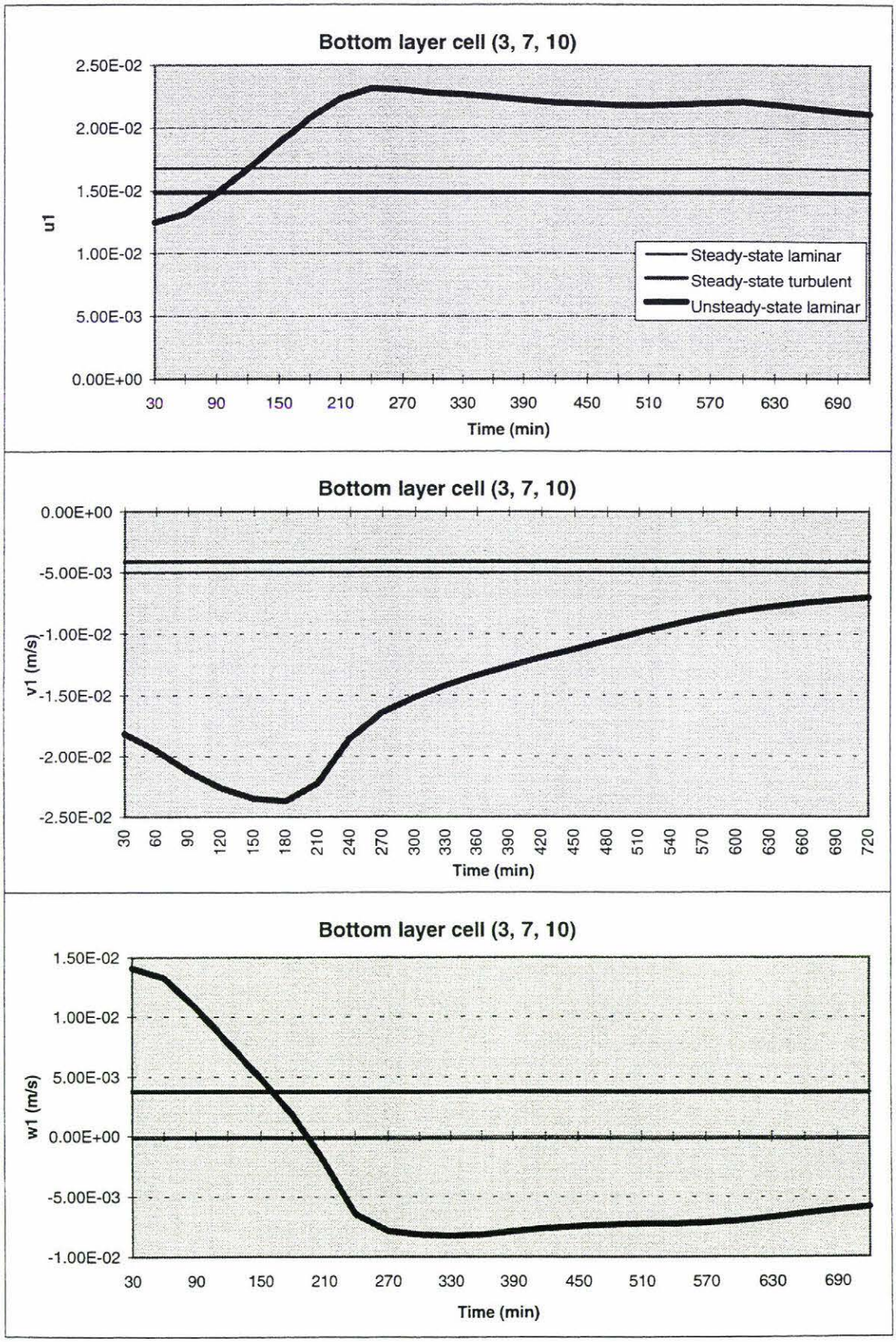

Figure 6-7a Predicted air velocity components in the cell (3, 7, 10)

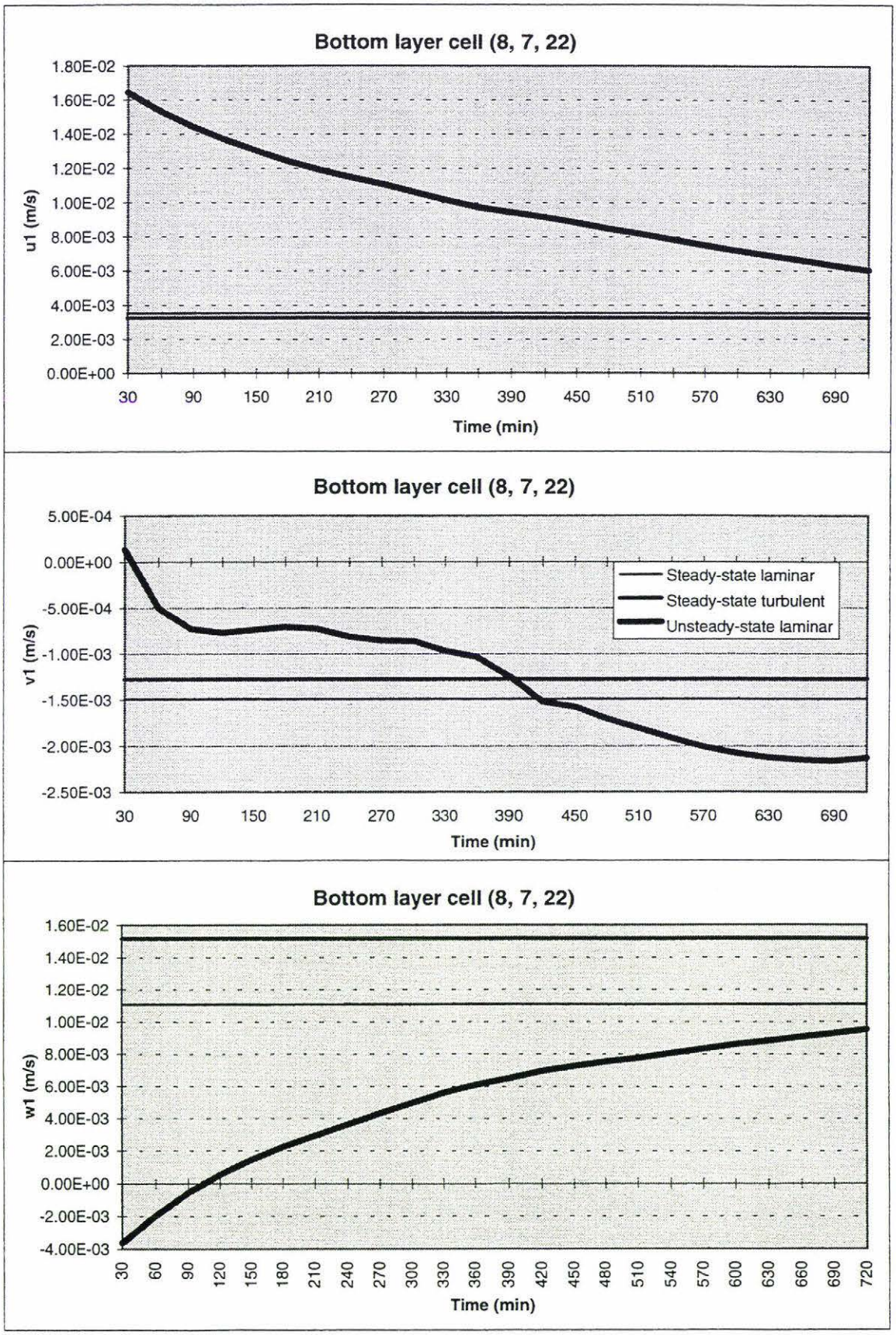

Figure 6-7b Predicted air velocity components in the cell (8, 7, 22)

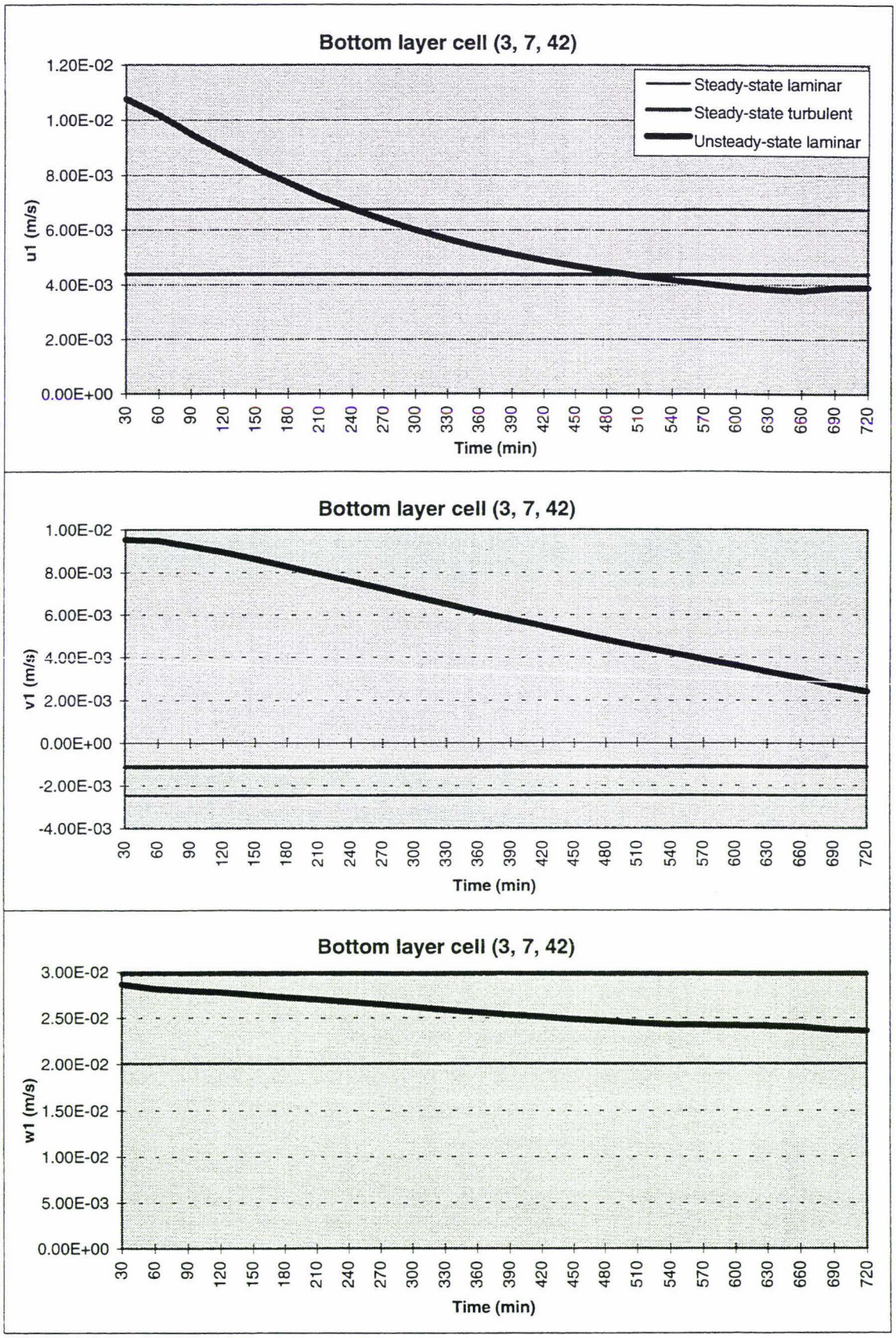

Figure 6-7c Predicted air velocity components in the cell (3, 7, 42)

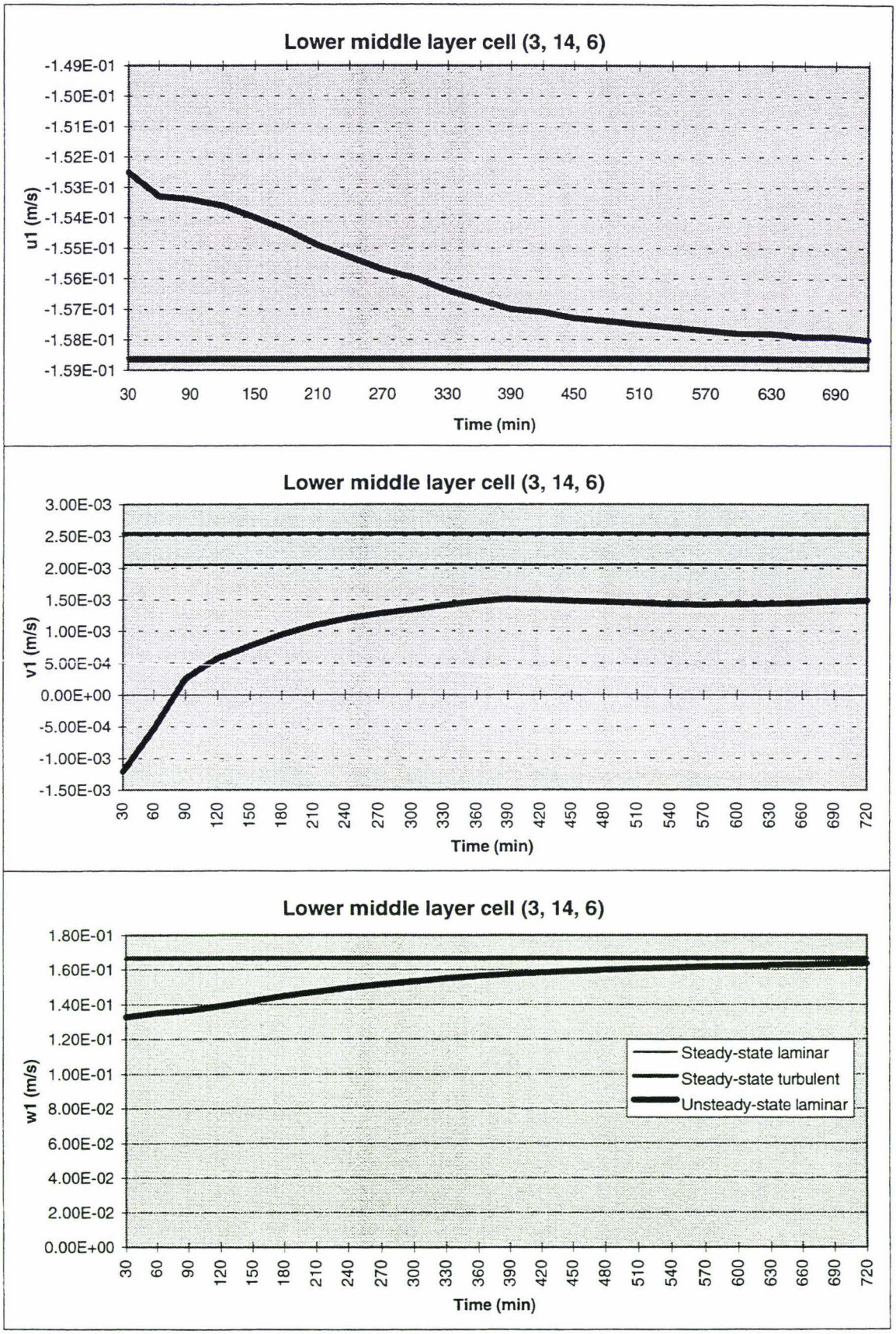

Figure 6-7d Predicted air velocity components in the cell (3, 14, 6)

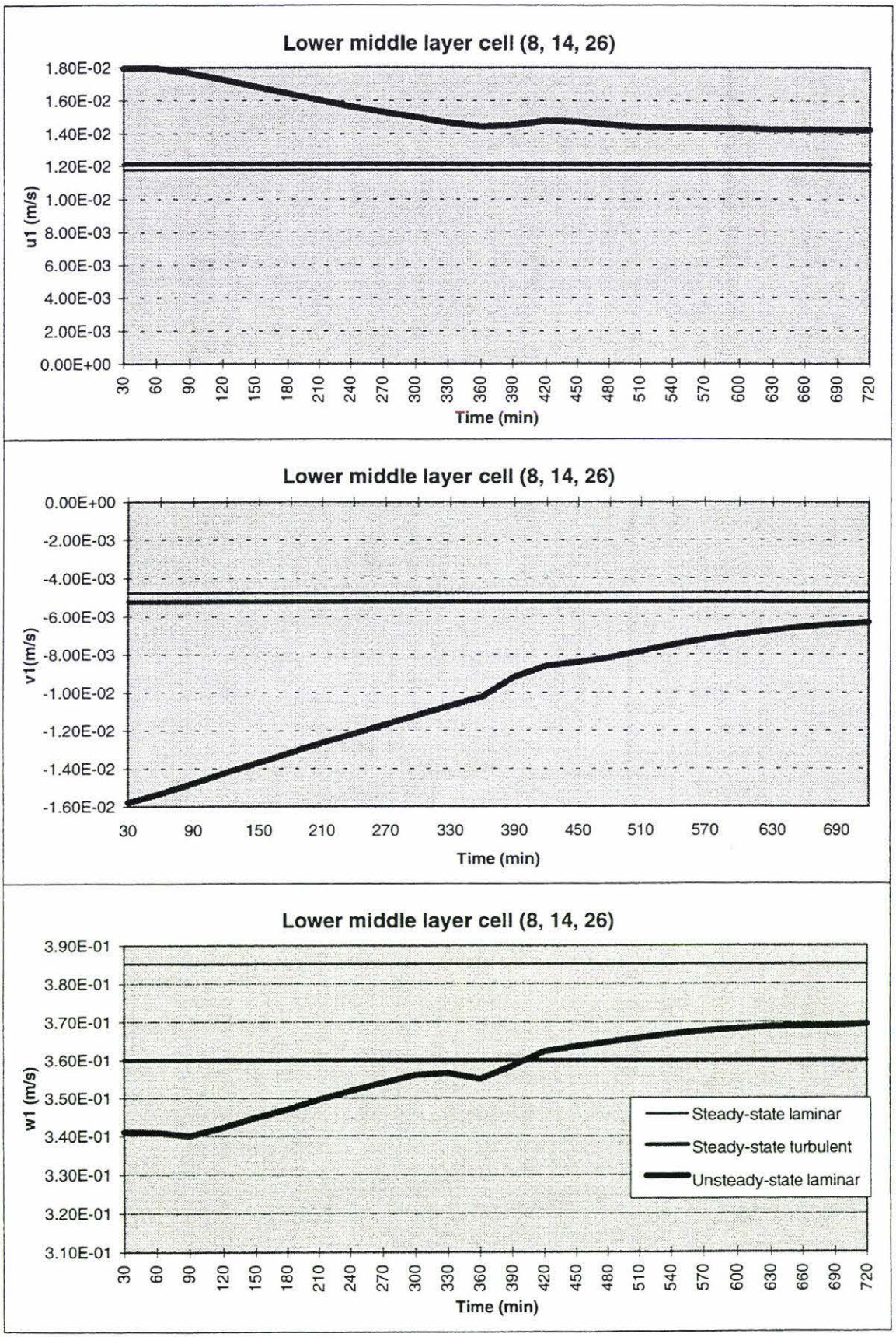

Figure 6-7e Predicted air velocity components in the cell (8, 14, 26)

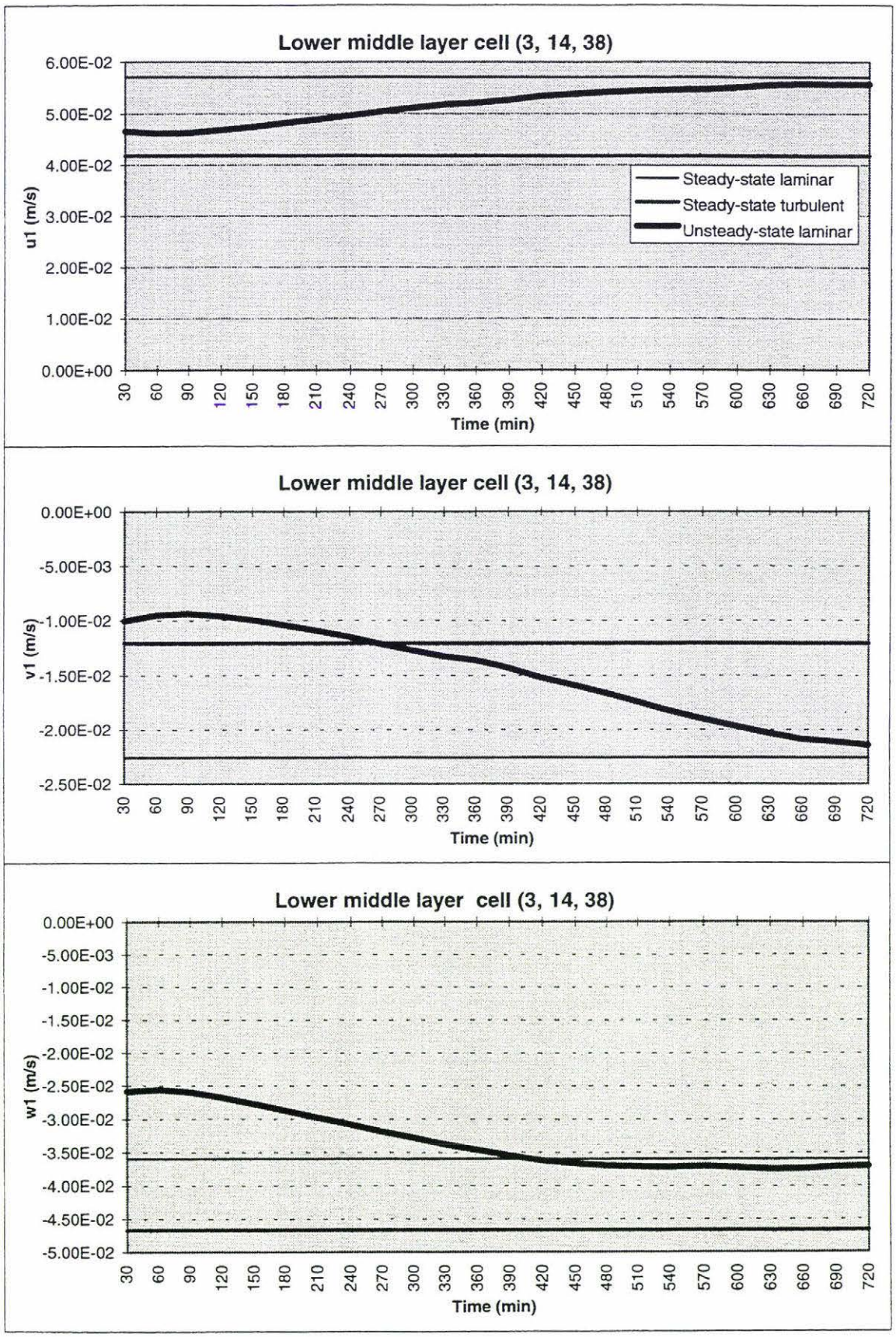

Figure 6-7f Predicted air velocity components in the cell (3, 14, 38)

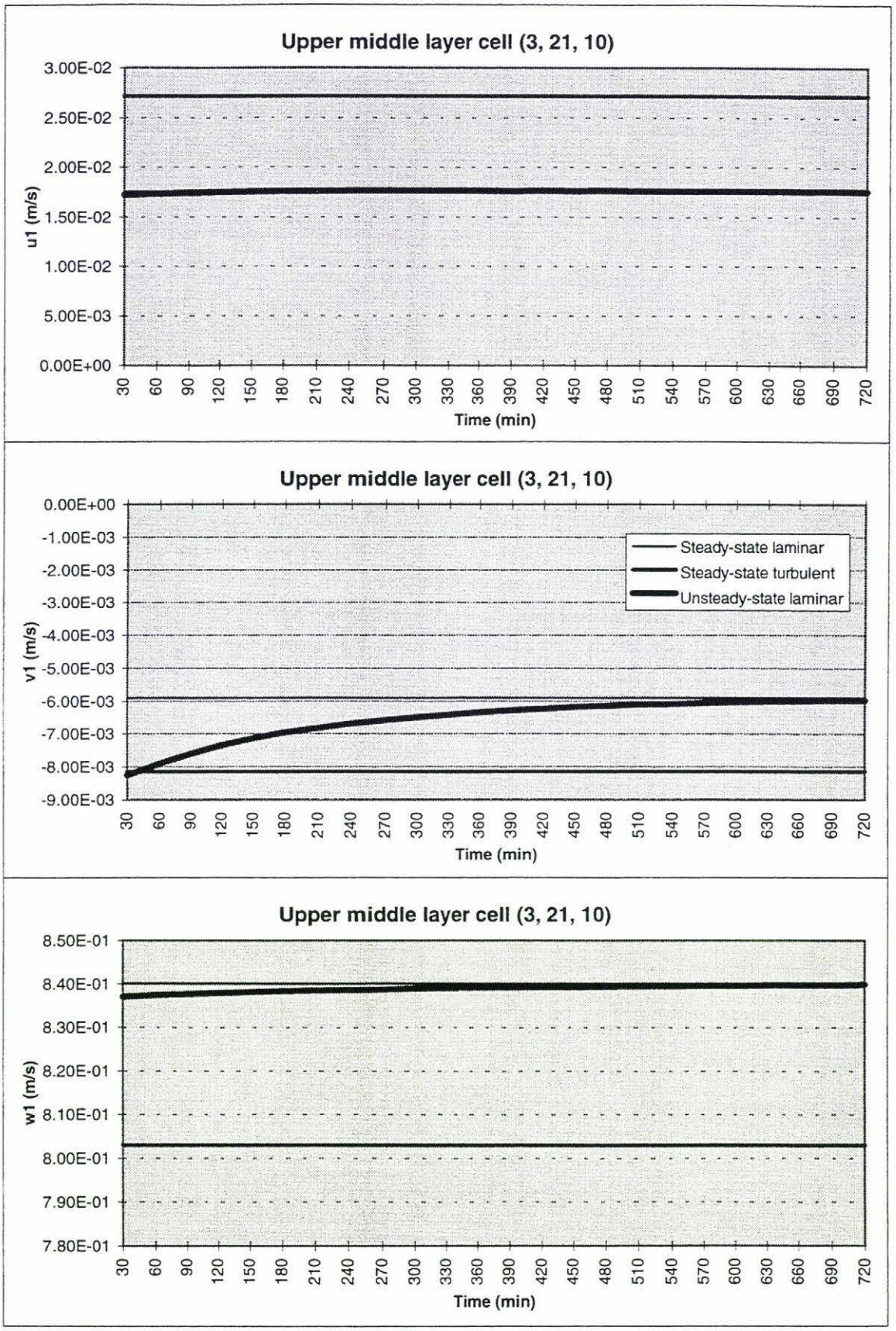

Figure 6-7g Predicted air velocity components in the cell (3, 21, 10)

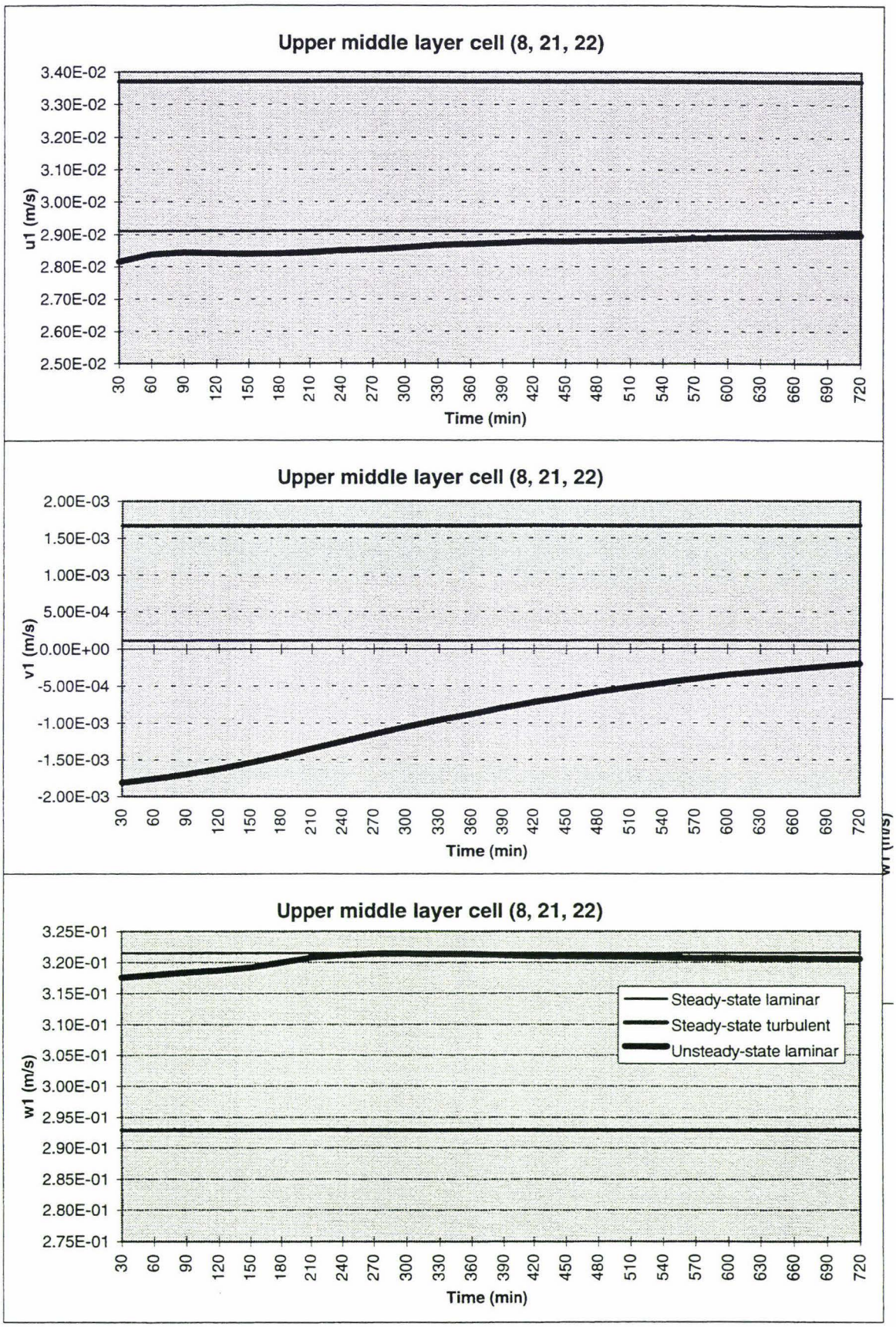

Figure 6-7h Predicted air velocity components in the cell (8, 21, 22)

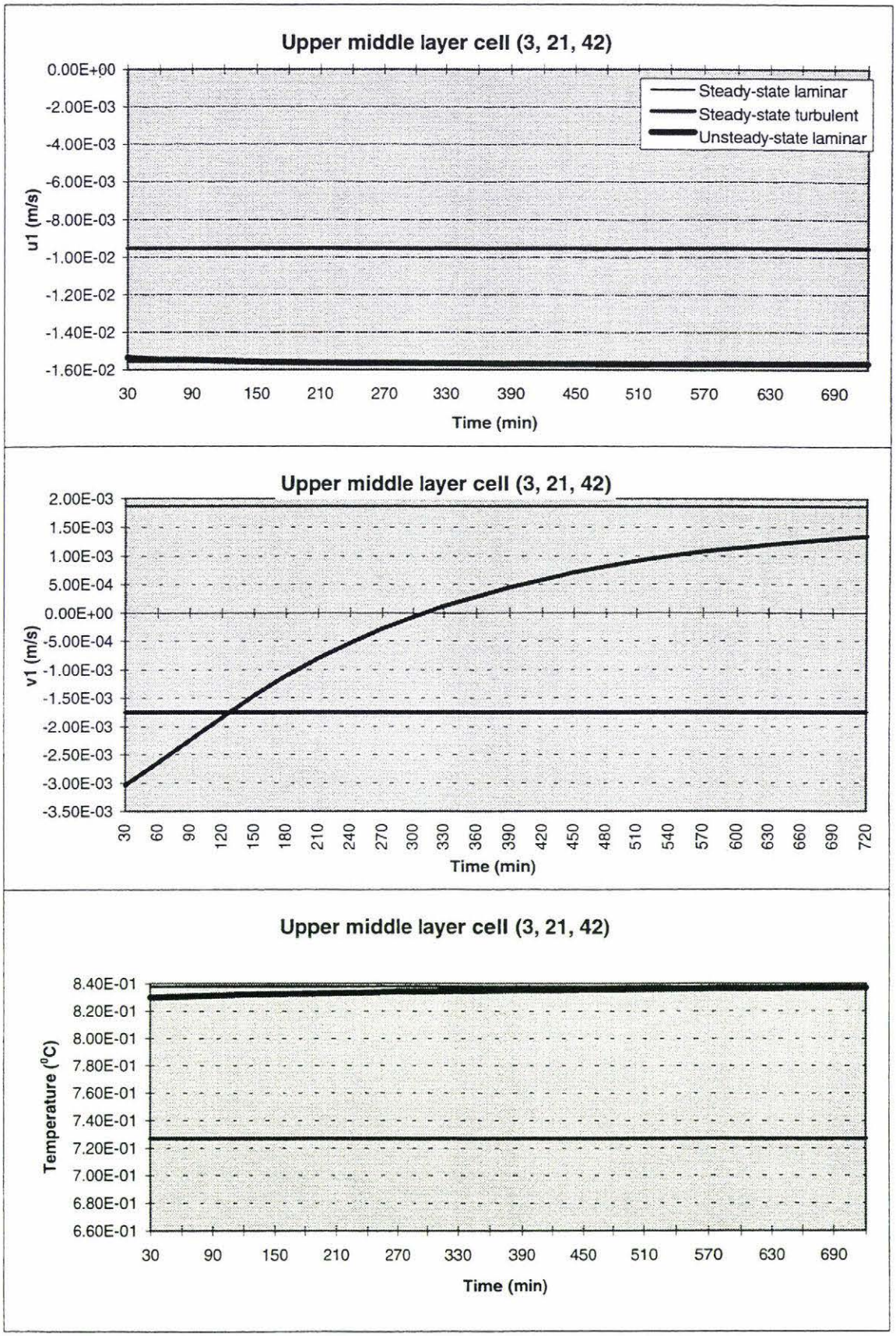

Figure 6-7i Predicted air velocity components in the cell (3, 21, 42)

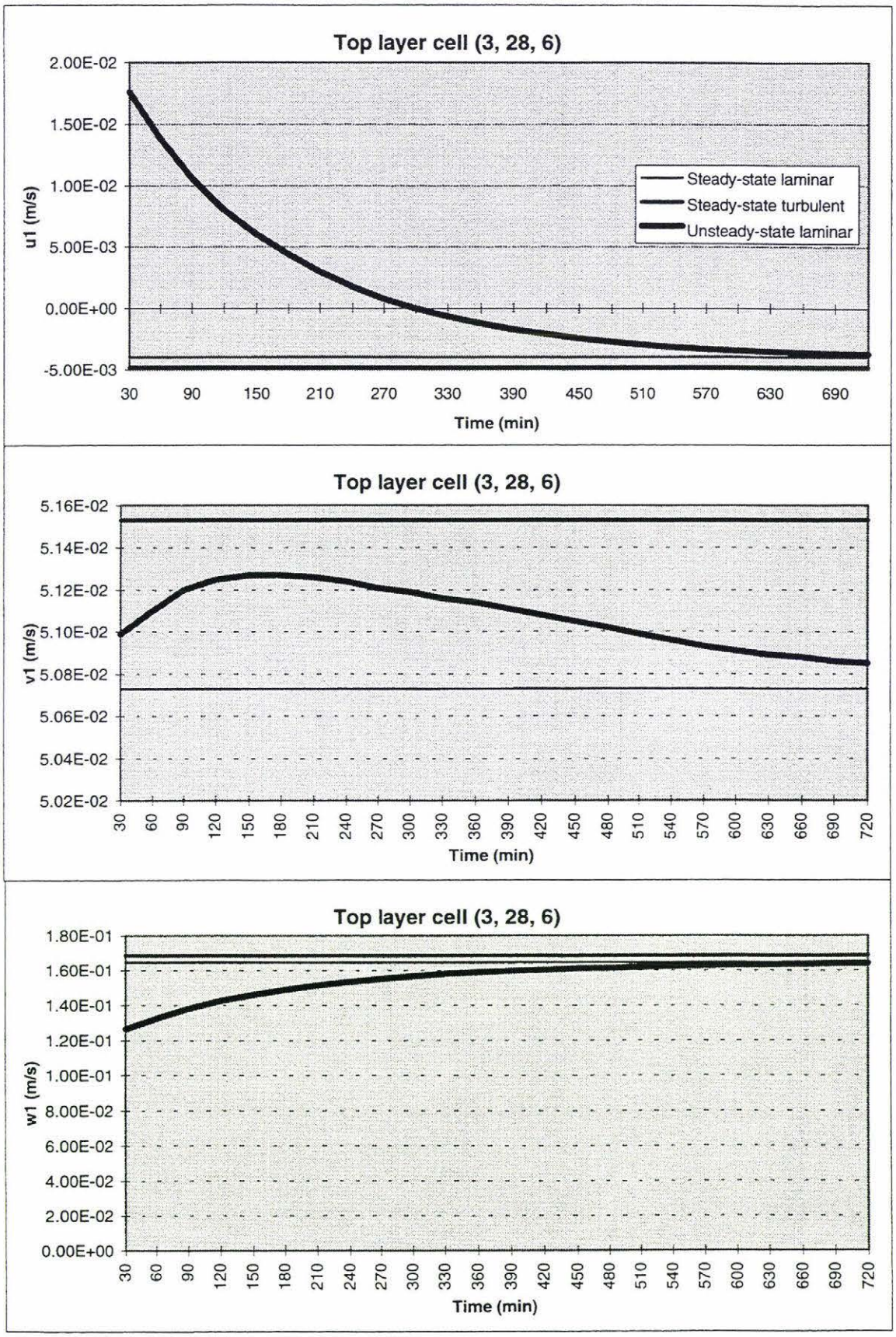

Figure 6-7j Predicted air velocity components in the cell (3, 28, 6)

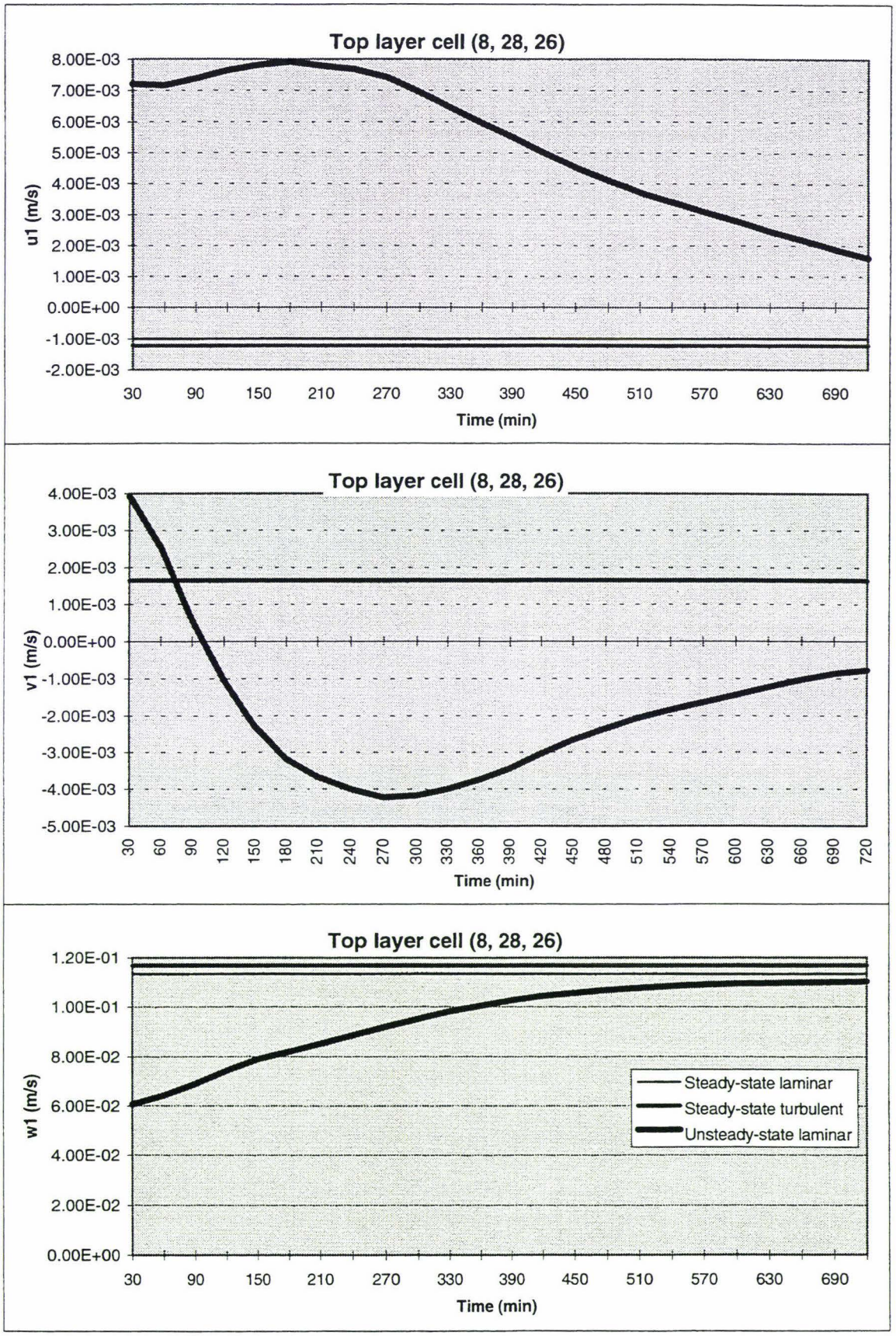

Figure 6-7k Predicted air velocity components in the cell (8, 28, 26)

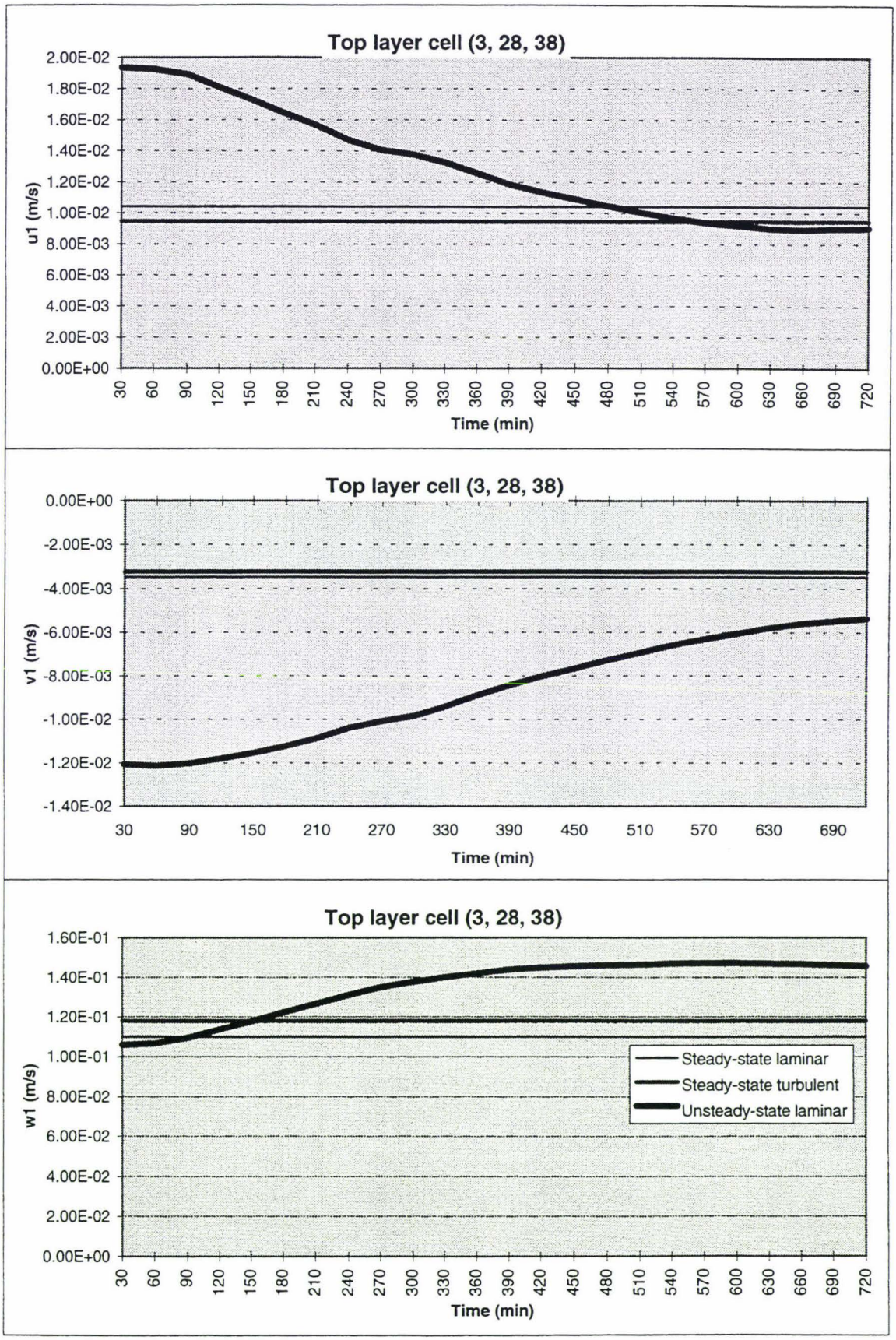

Figure 6-71 Predicted air velocity components in the cell (3, 28, 38)

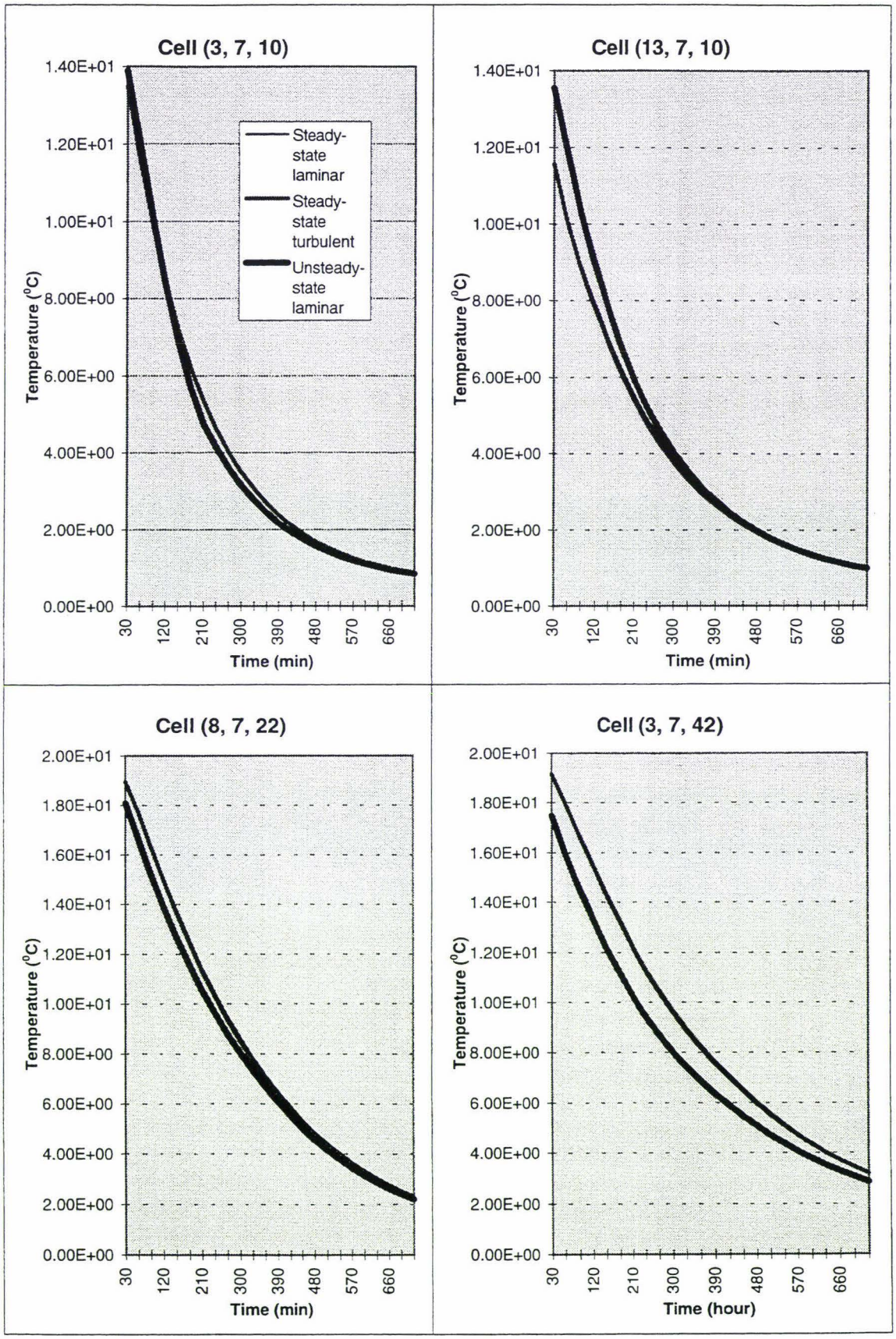

Figure 6-8a Predicted air temperature in the cells of bottom layer

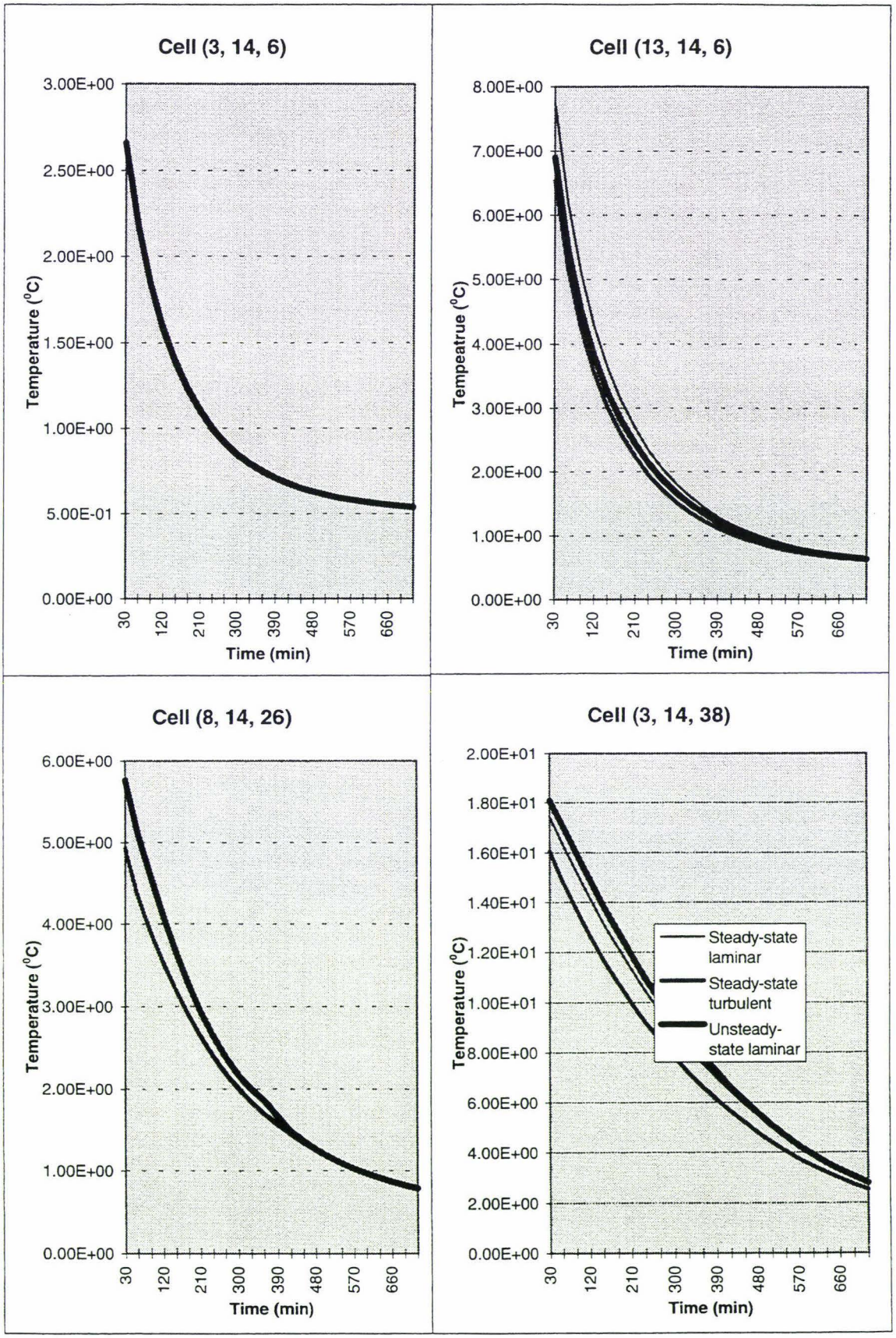

Figure 6-8b Predicted air temperature in the cells of lower middle layer

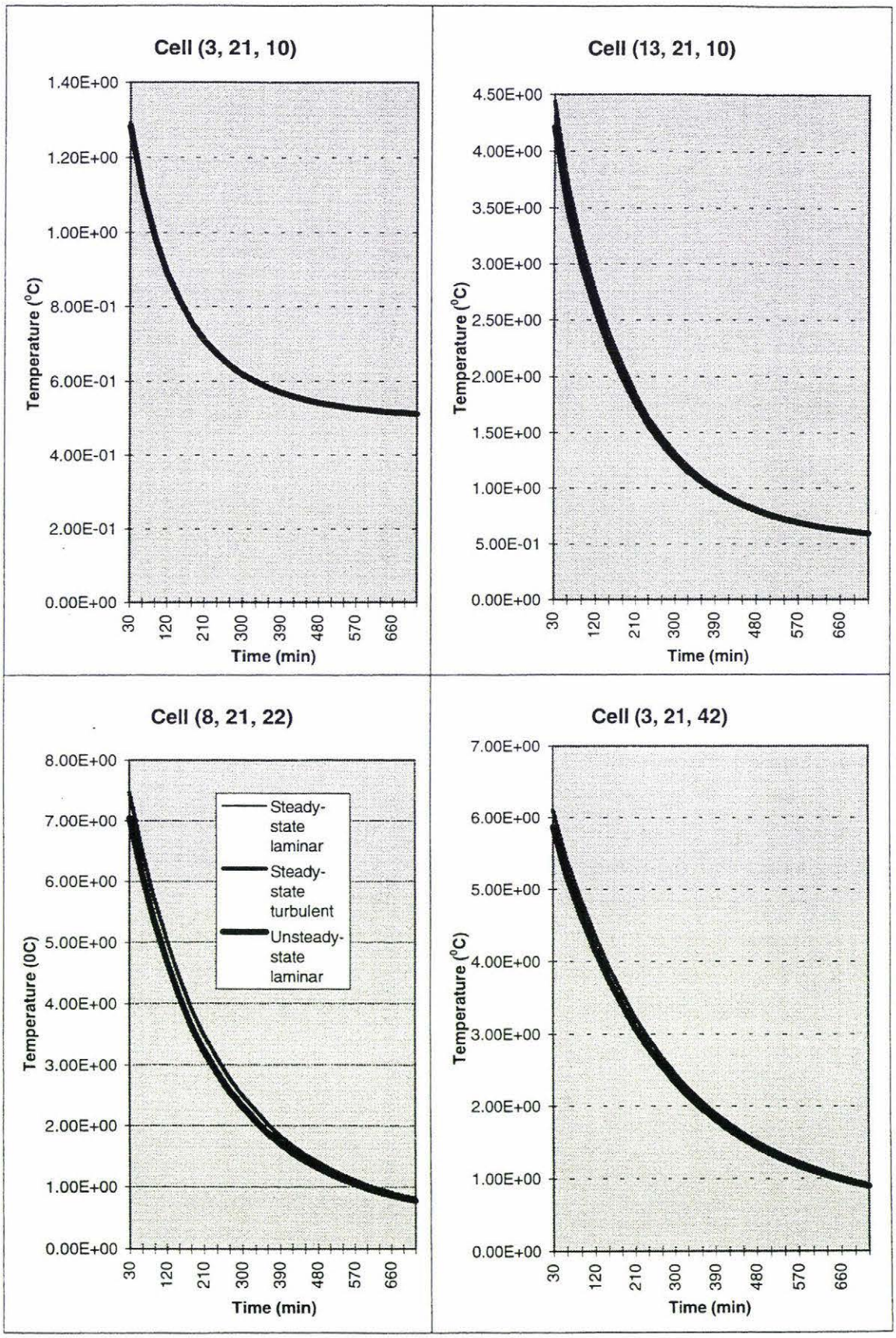

Figure 6-8c Predicted air temperature in the cells of upper middle layer

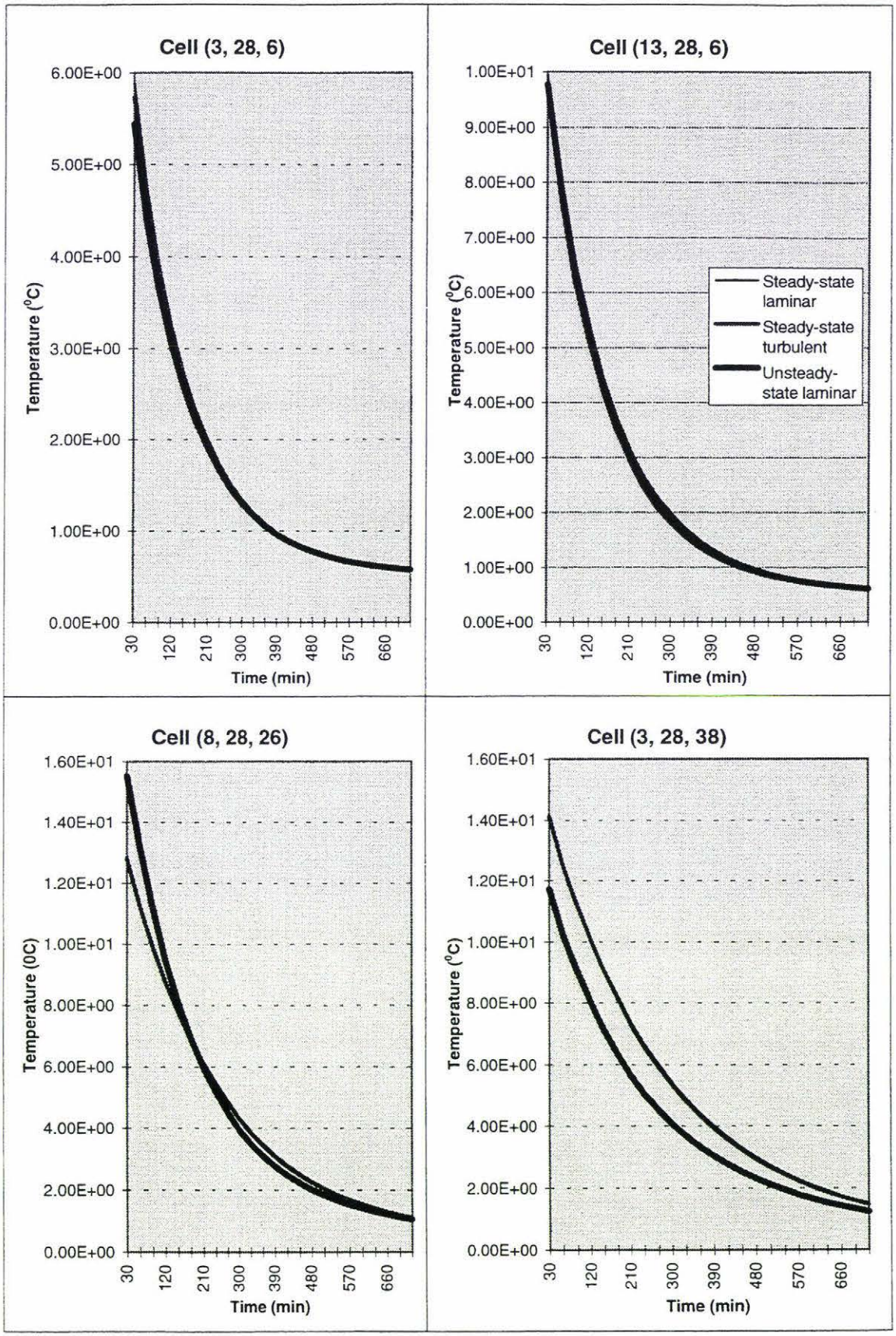

Figure 6-8d Predicted air temperature in the cells of top layer

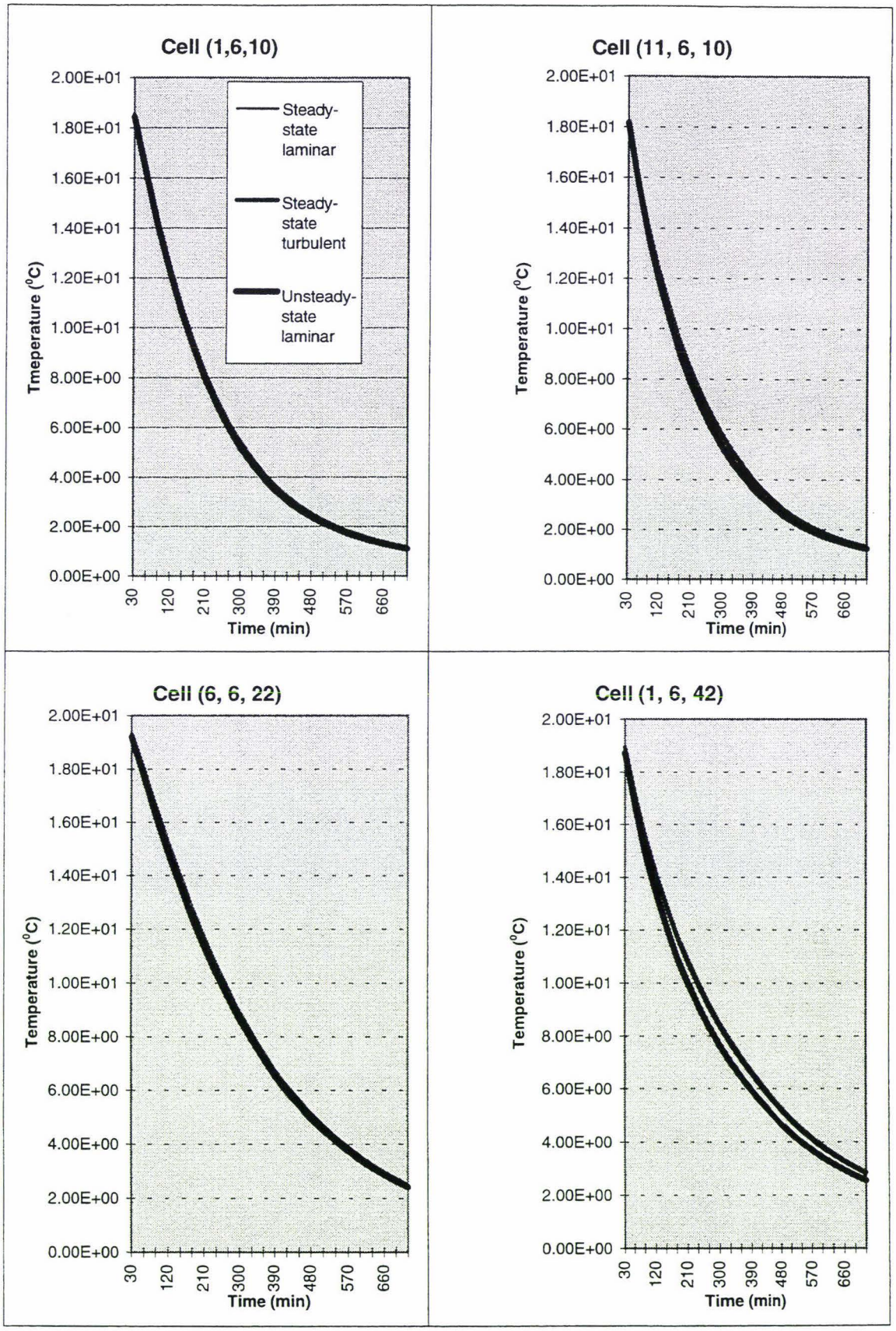

Figure 6-9a Predicted apple centre temperature in the cells of bottom layer

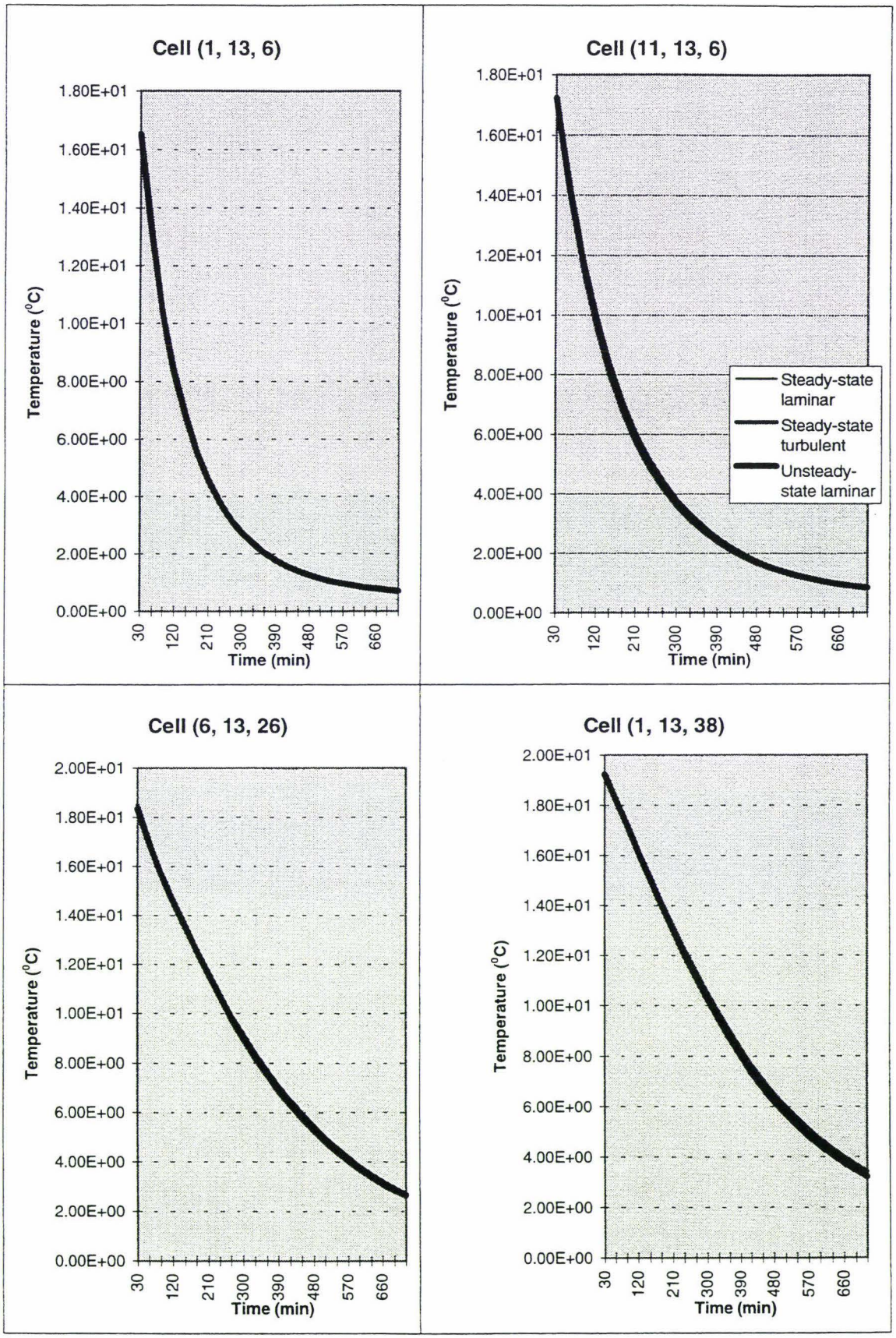

Figure 6-9b Predicted apple centre temperature in the cells of lower middle layer

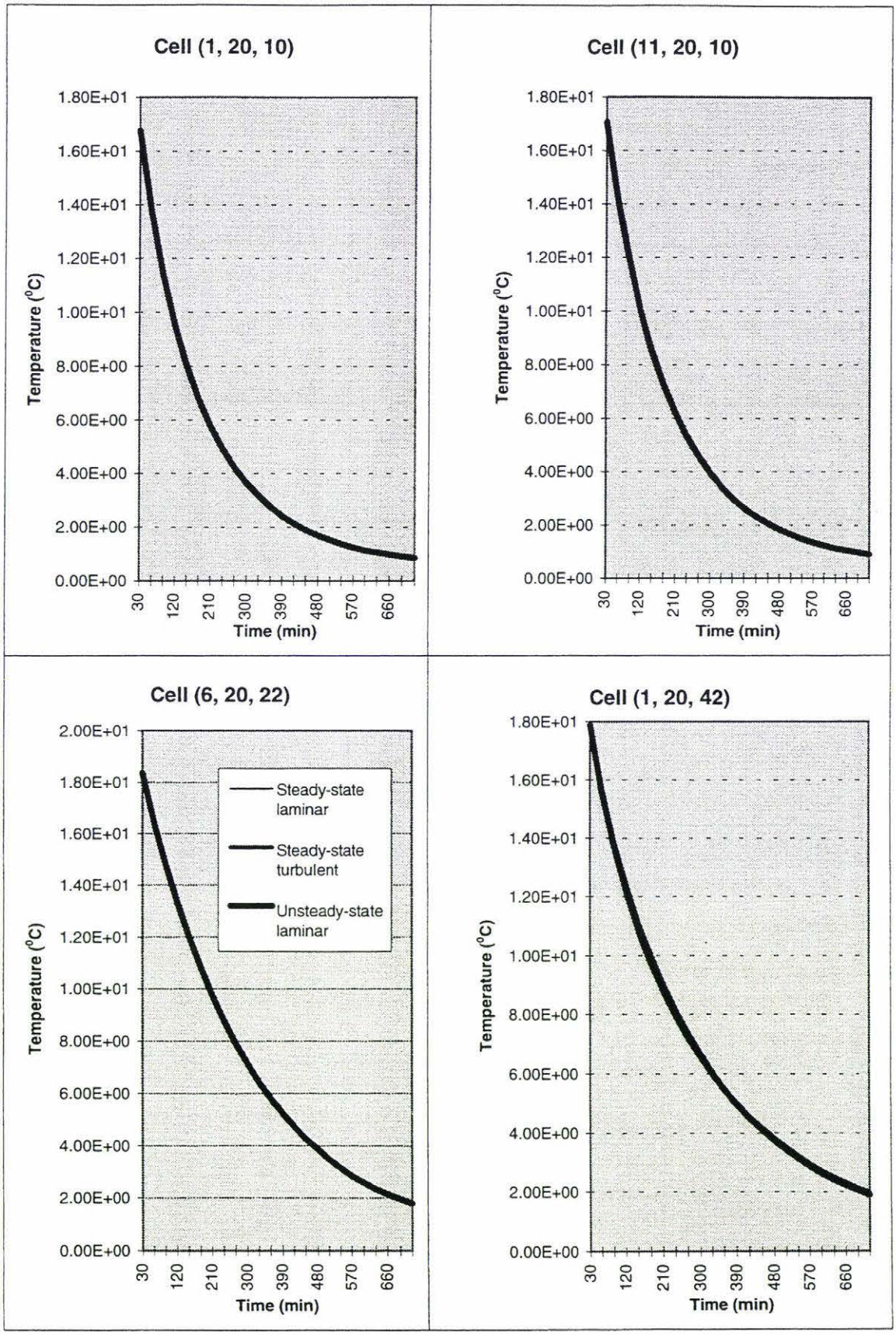

Figure 6-9c Predicted apple centre temperature in the cells of upper middle layer

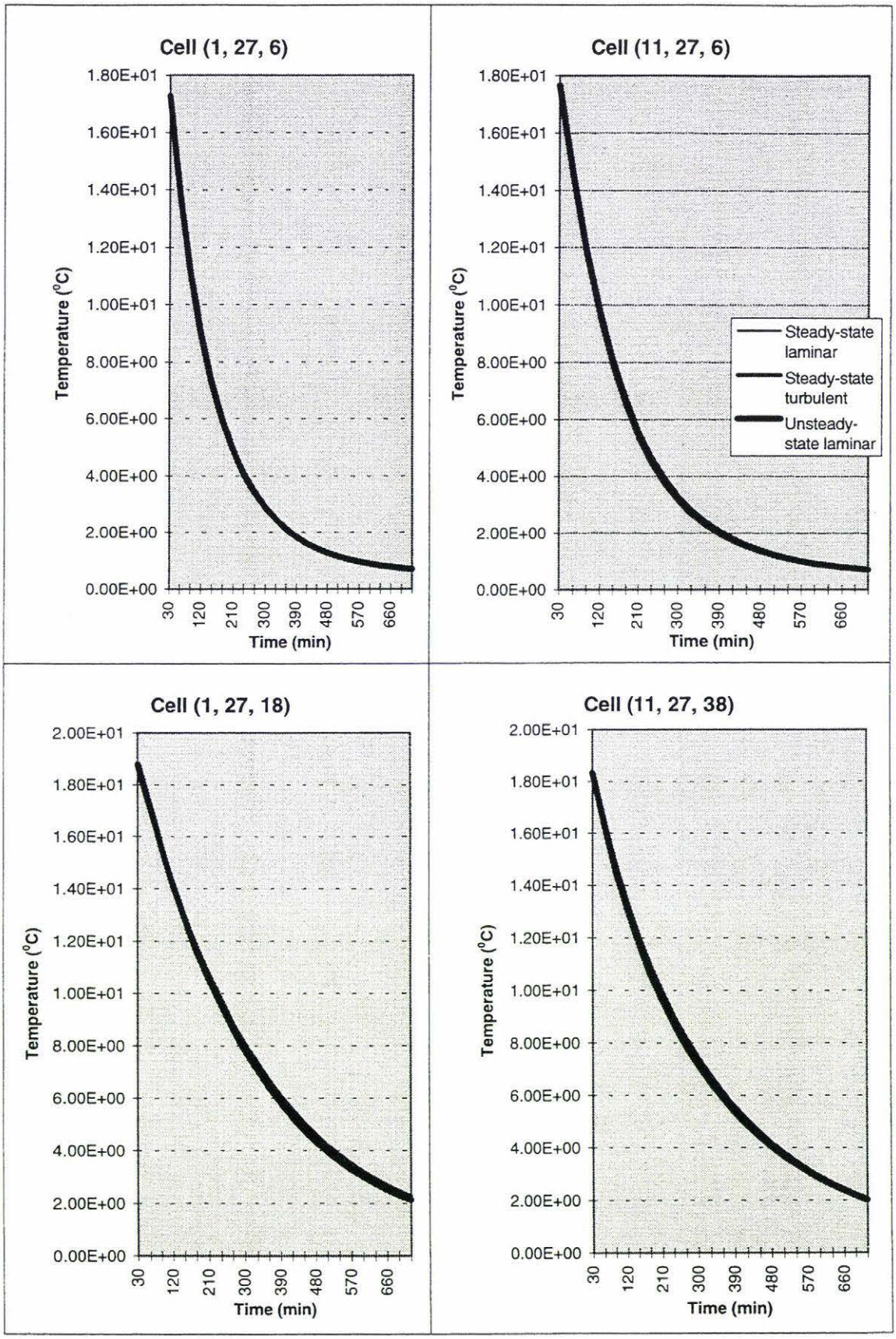

Figure 6-9d Predicted apple centre temperature in the cells of top layer

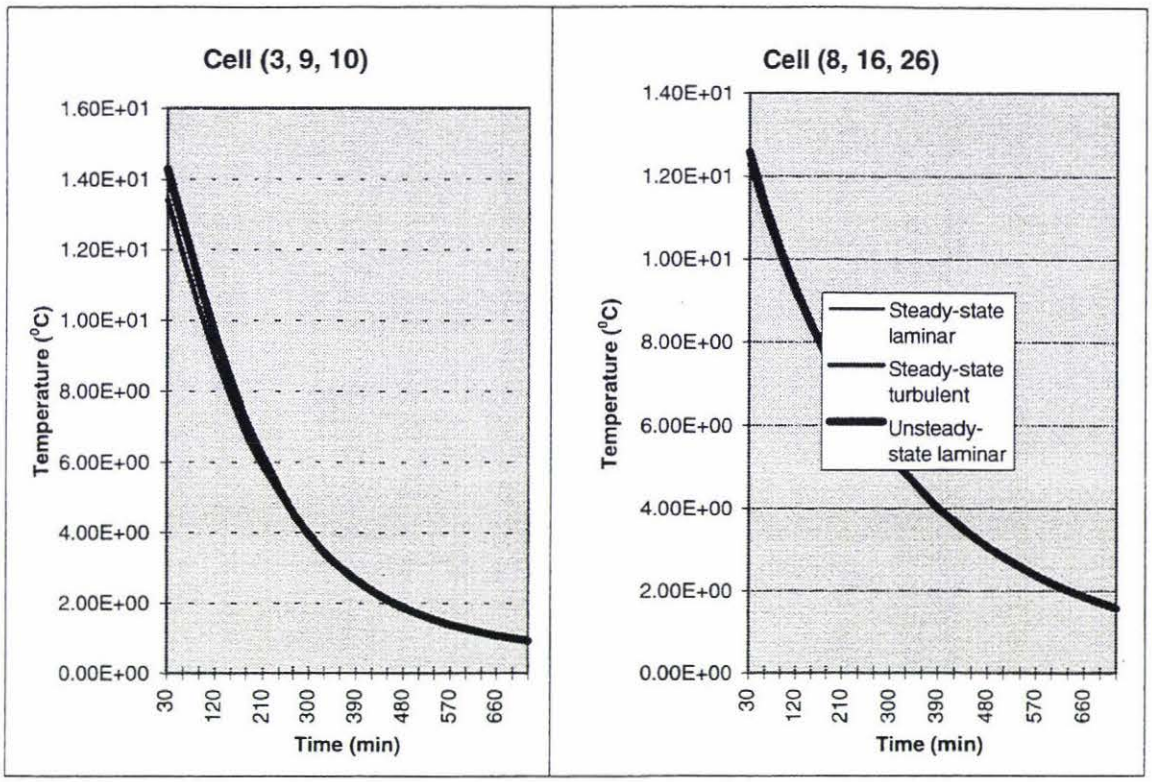

Figure 6-10 Predicted tray temperature in two cells

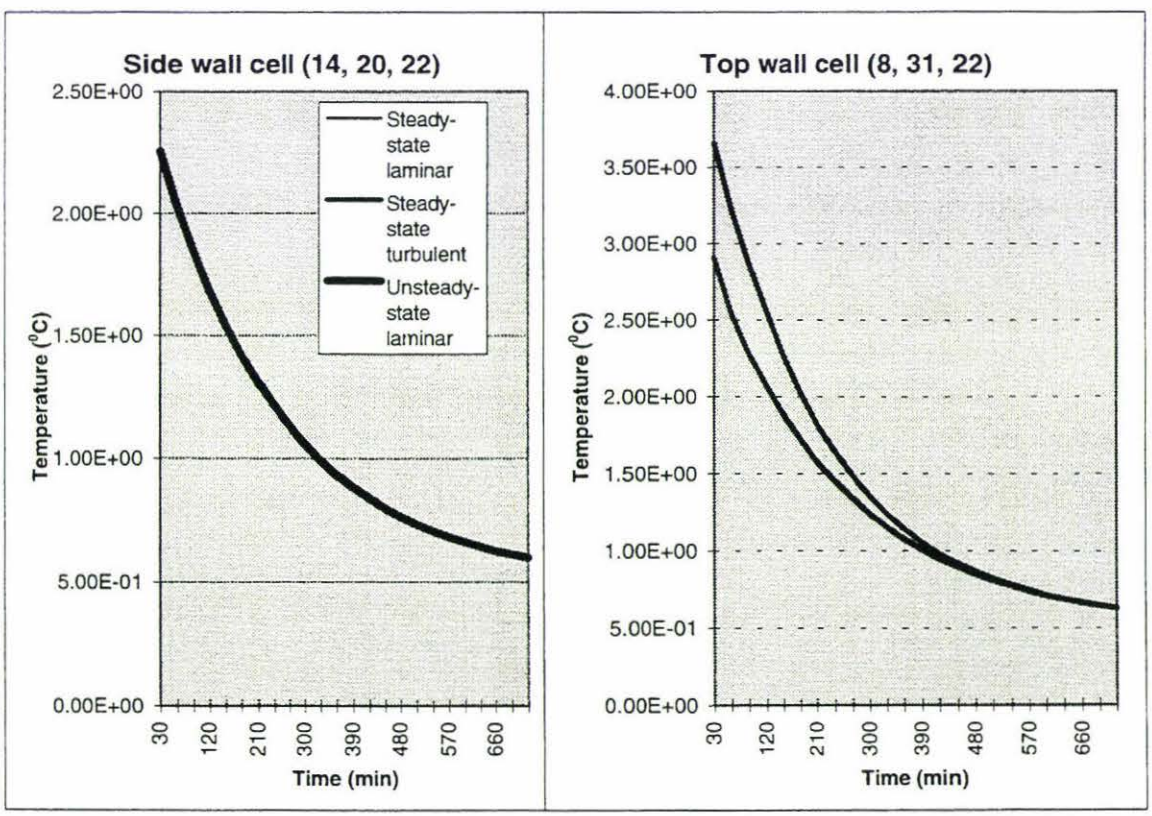

Figure 6-11 Predicted carton temperature in two cells

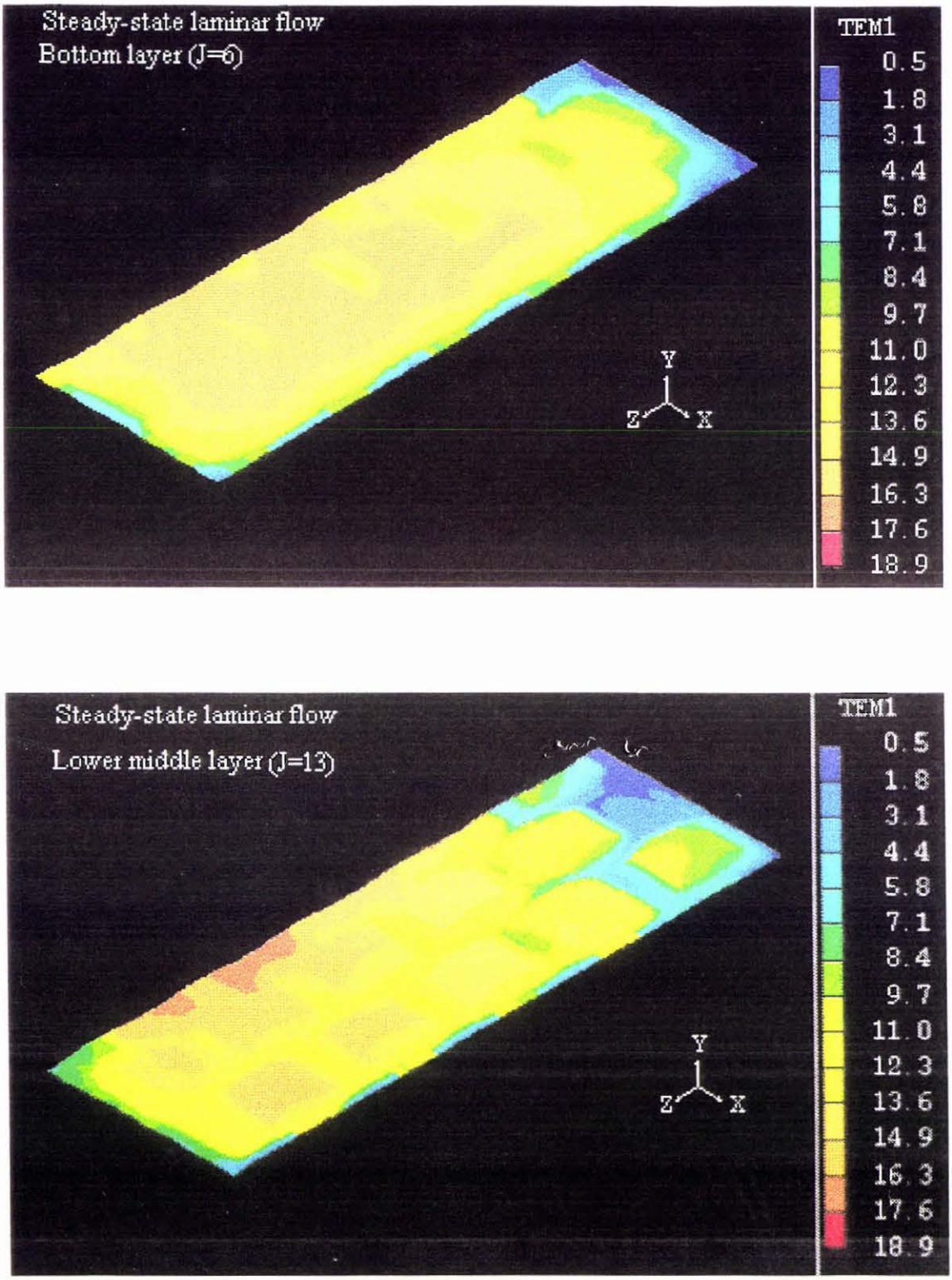

Figure 6.12 Predicted temperature contours after two-hour cooling for steady-state laminar flow

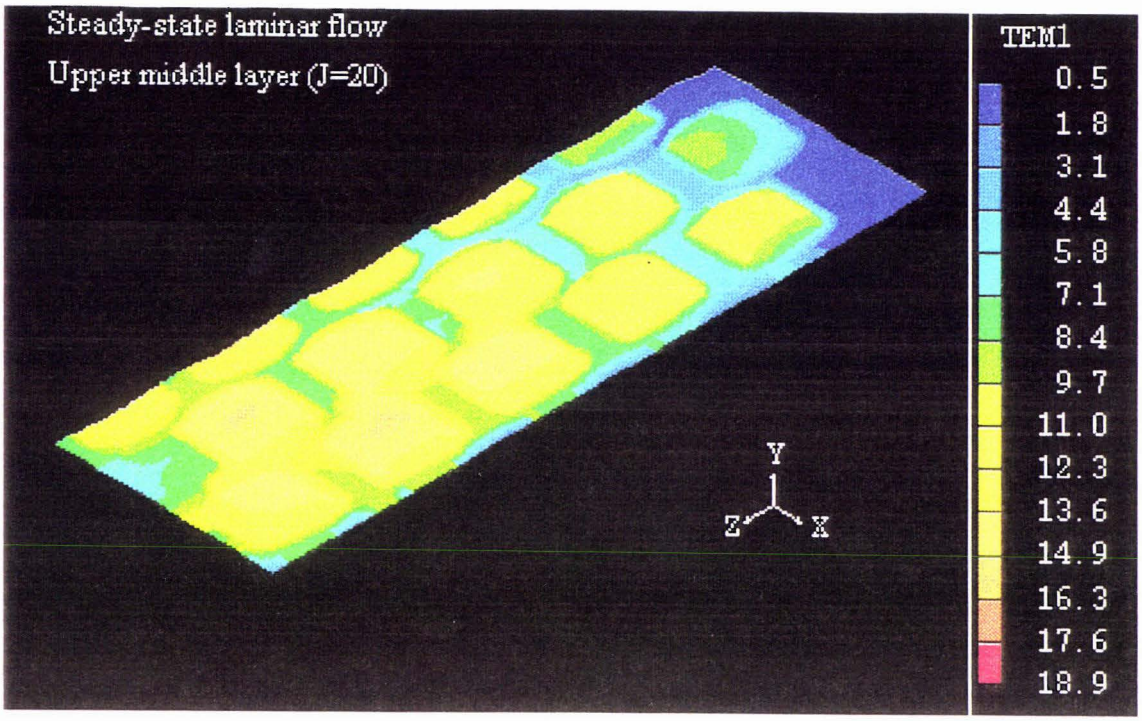

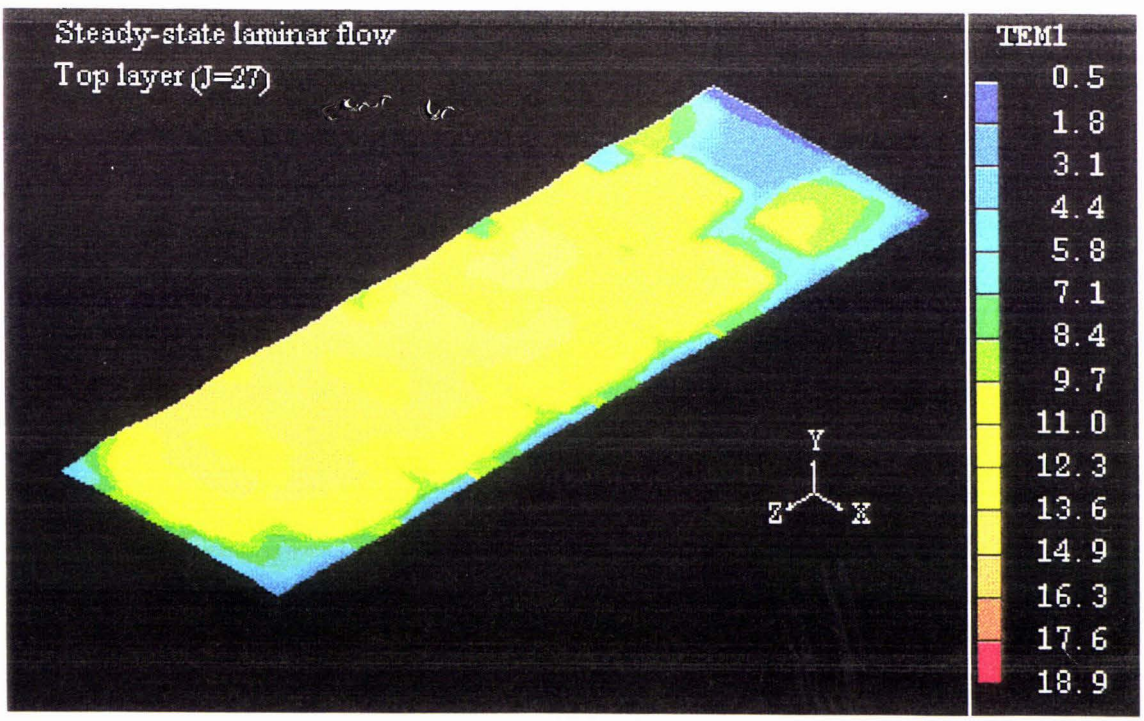

Figure 6.12 (continued) Predicted temperature contours after two-hour cooling for steady-state laminar flow

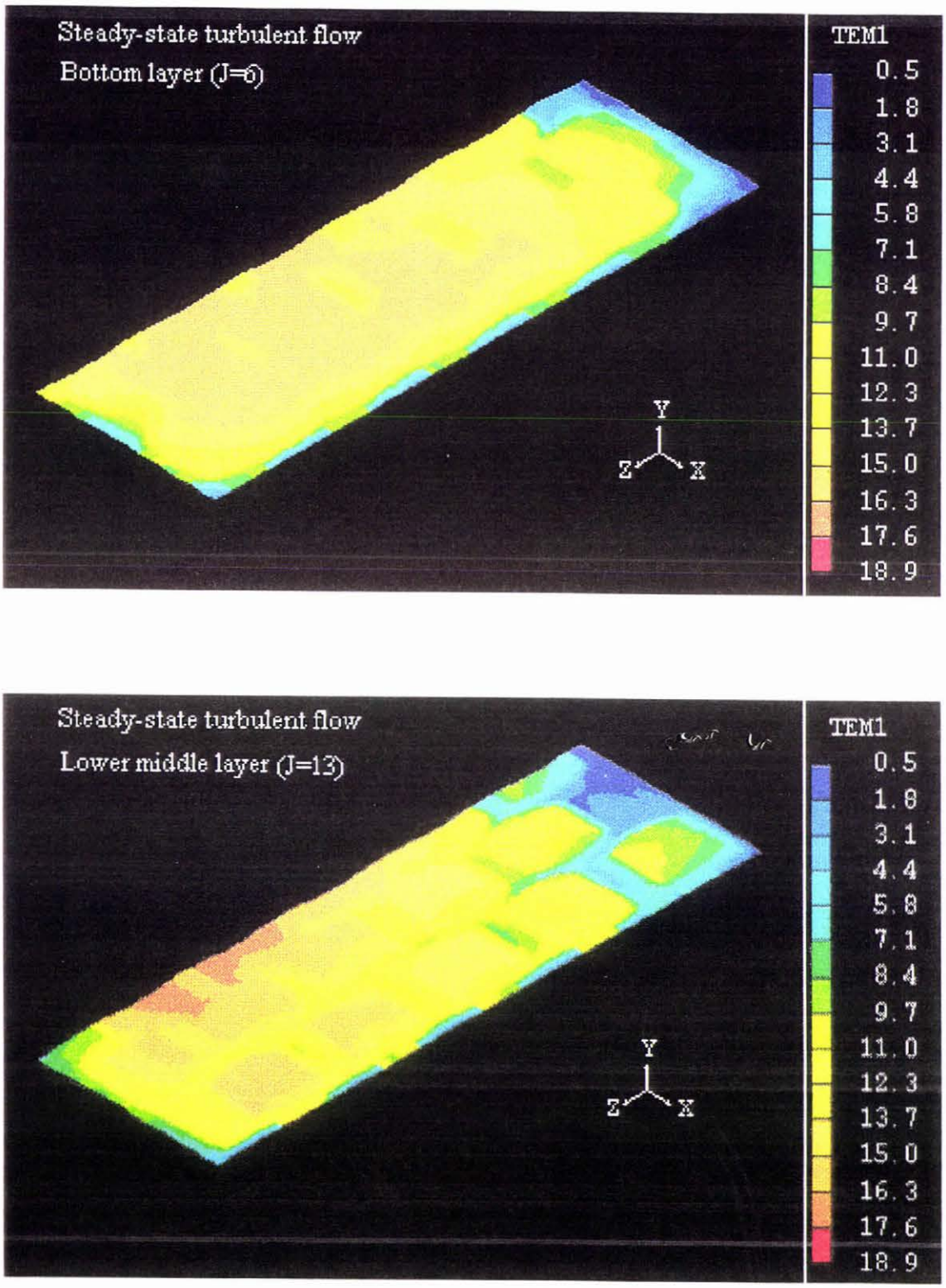

Figure 6.13 Predicted temperature contours after two-hour cooling for steady-state turbulent flow

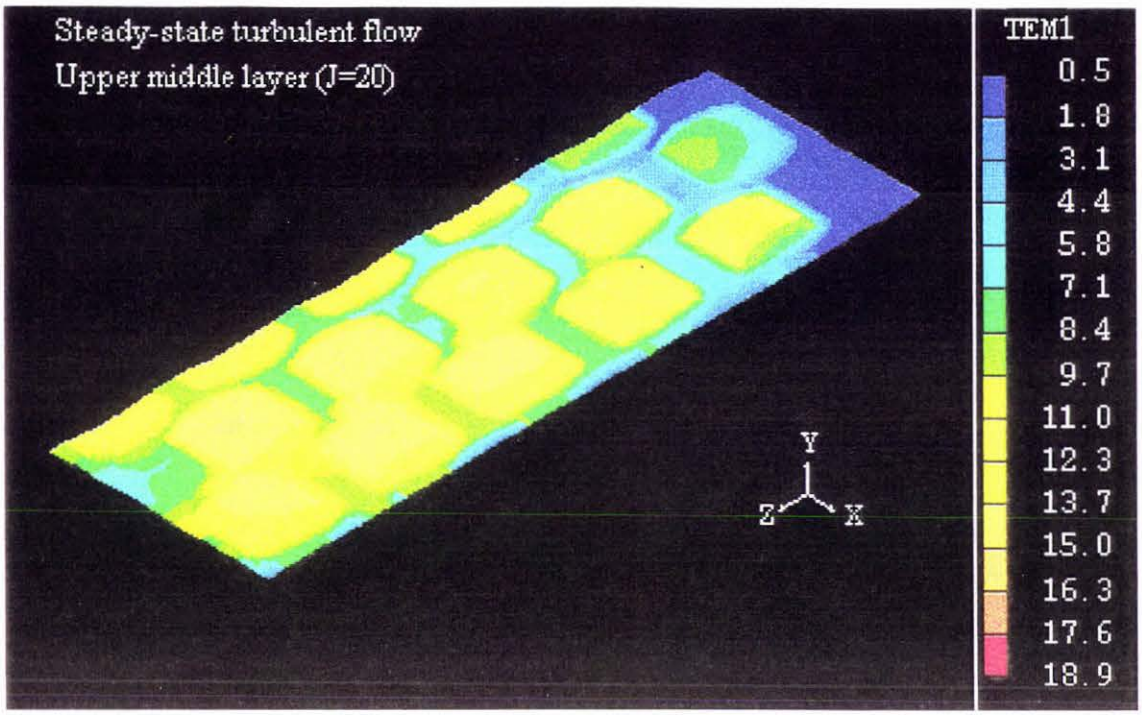

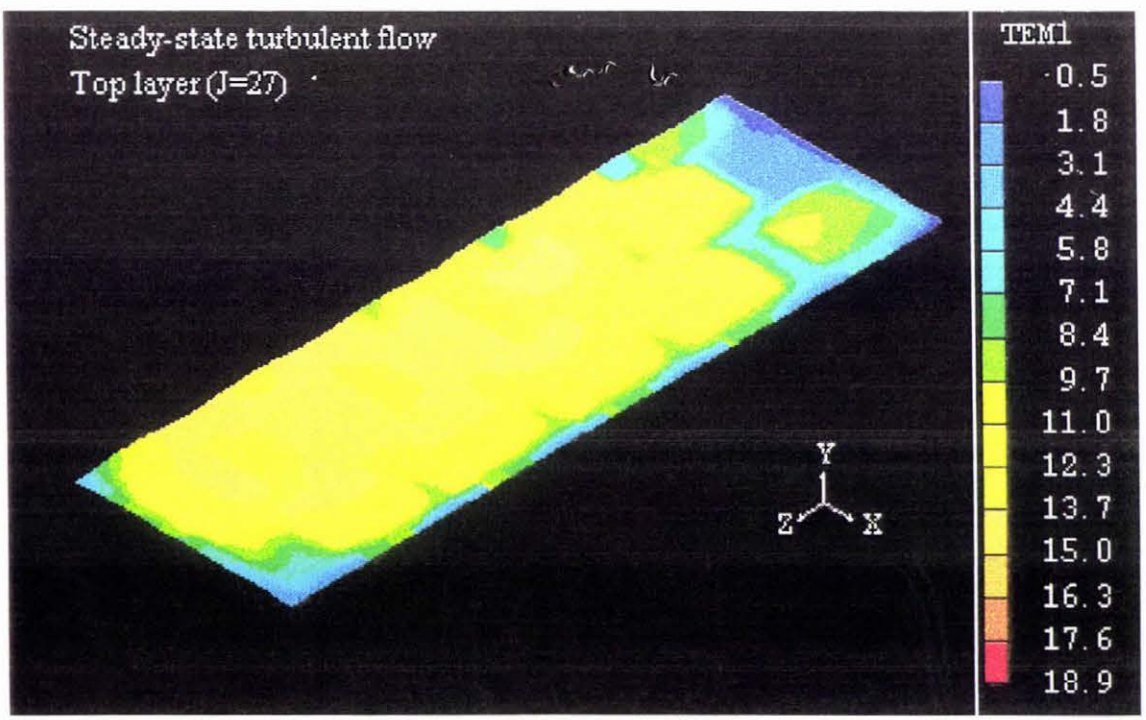

Figure 6.13 (continued) Predicted temperature contours after two-hour cooling for steady-state turbulent flow

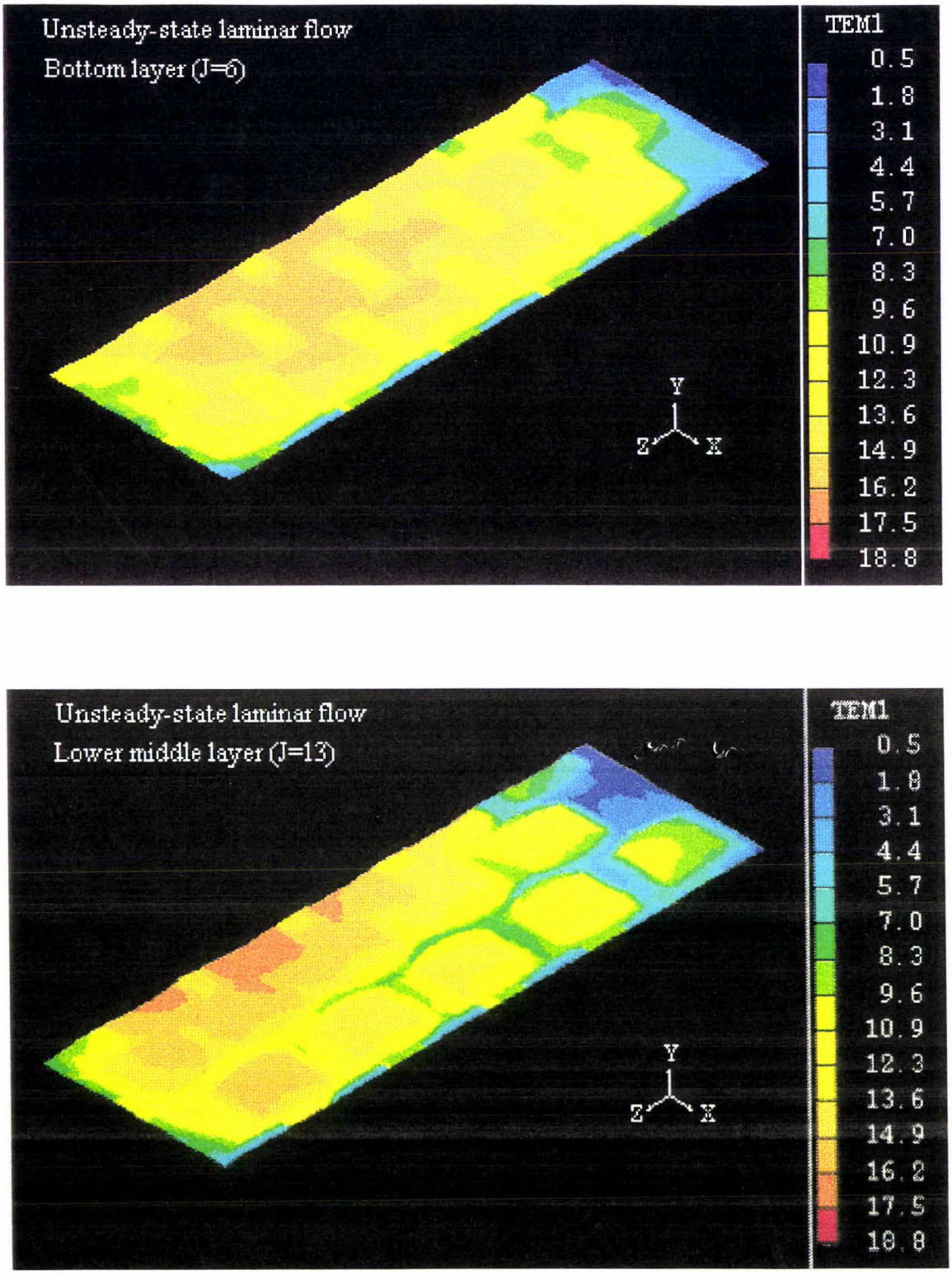

Figure 6.14 Predicted temperature contours after two-hour cooling for unsteady-state laminar flow

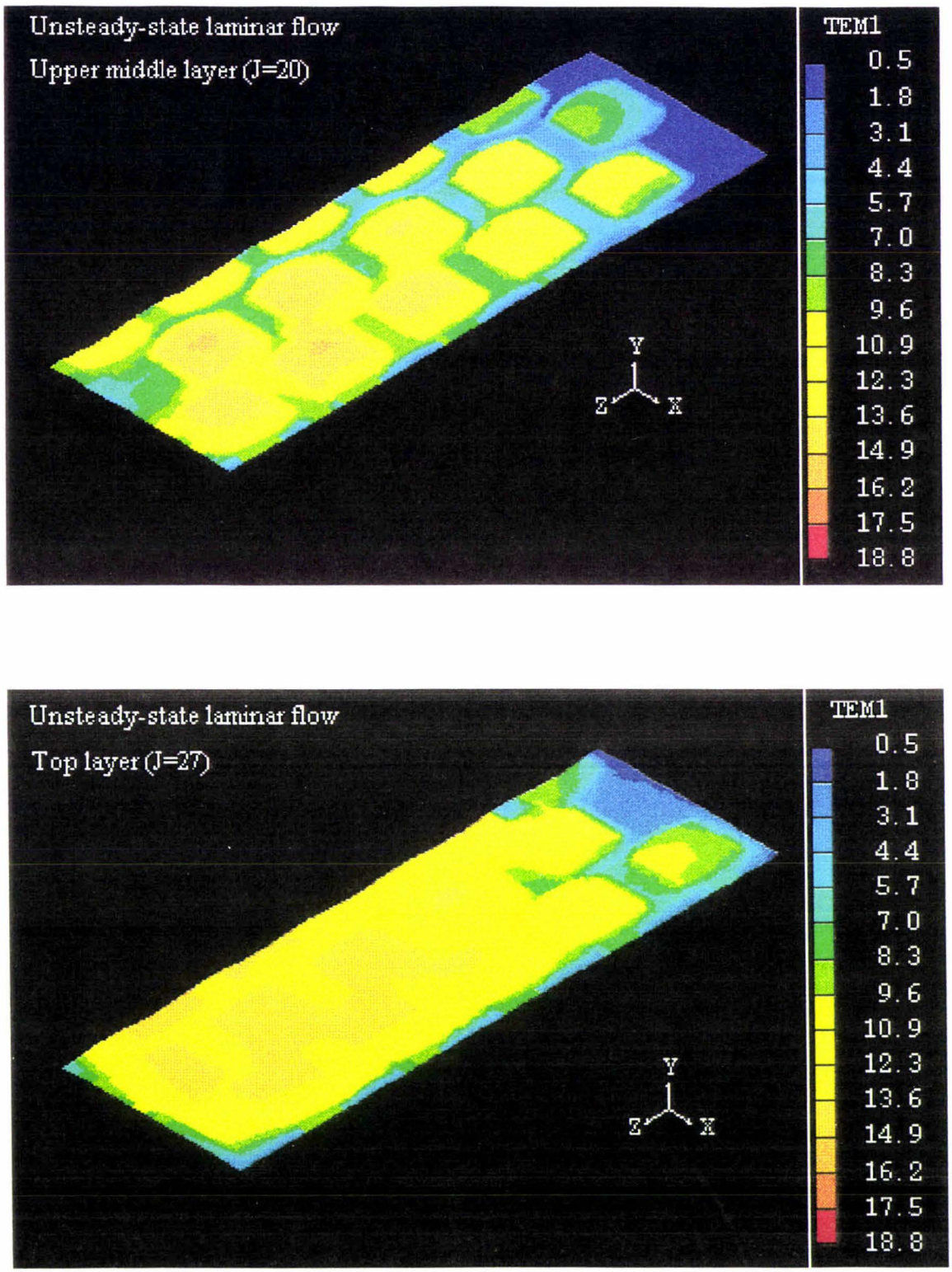

Figure 6.14 (continued) Predicted temperature contours after two-hour cooling for unsteady-state laminar flow

CHAPTER 7: MODEL VALIDATION

The CFD models presented in the previous chapters were used to predict air velocity inside the package and temperature profiles of air, fruit and packaging material using the PHOENICS code. PHOENICS also can be used to visualise air flow patterns according to the calculated velocities. In order to justify the mode for the real world application for product cooling, an experimental scheme was needed for visualisation of real air flow patterns within the cartons, and measuring relevant velocity and temperature. The measured data should be compared with the model predictions. The model prediction is accepted if the satisfactory agreement between the experimental data and model results is achieved. However due to time restriction and limited availability of facilities, only temperature in fruit centres was measured.

7.1 TRIAL OF APPLE PRECOOLING

In the experiment, a TAI Z PACK, 100-count carton was placed in an environmental tunnel at Massey University (Figure 7.1), in which controlled temperature and uniform air velocity were achieved. Before being placed in the tunnel, the apple carton was left outside until a uniform temperature of air, apple, and packaging materials was achieved.

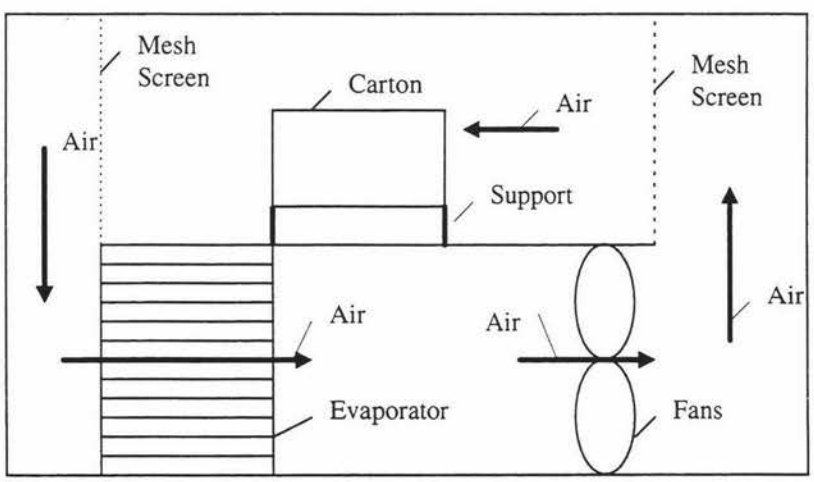

Figure 7.1 Controlled environmental tunnel (adapted from Amos, 1995).

A "testo 452" Vane anemometer was used to measure air velocity in the carton inlets and in the tunnel. Its accuracy was 1% of measured value. The mean velocities over three inlets were recorded. Air velocity inside the carton was not measured due to unavailability of appropriate miniature anemometers.

T-type thermocouples were used to measure temperature of apple centres, carton, trays and inlet air flow. A Campbell Scientific data logger CR10X was employed to record the measured temperature. Analog Devices ADS90 reference junction was used to measure temperature of wiring panel of CR10X datalogger. Due to limited availability of the environmental tunnel, air temperature inside the carton was not measured.

7.2 COMPARISON OF MODEL PREDICTIONS AND MEASURED DATA

According to measured initial temperature, air velocities in the carton inlets and environmental tunnel, PHOENICS programmes for steady-state laminar and turbulent flow were run under the set of input data (Table 7.1). Other input data are the same as specified in section 6.1.

Figure 7.2 compares the measured temperature of apple centres with the model predictions for steady-state laminar and turbulent flows. Cooling rate was expressed as 7/8-cooling time which is the time required to reduce the temperature difference between the product and its surroundings by 7/8 (ASHRAE, 1994). Table 7.3 shows the measured and predicted 7/8-cooling times.

The errors in measured temperature were obvious in the beginning of cooling, and that was due to the time needed for the temperature of wiring panel of CR10X to reach uniform point after being placed in the environmental tunnel.

Predictions for laminar and turbulent flows were almost identical. By comparing measured and predicted data, it can be seen that the largest errors occurred in the apples near air inlets in the upper middle and top layers. The cooling rates at these locations were underestimated by about 50%-100%. Fairly large errors were also found in the apples

close to the rear outlets in the bottom and middle layers, where the cooling rates were overestimated by about 35%. The errors may be attributed to the complex air flow patterns in these regions which may not be modelled accurately. Possible errors in measuring devices could also partly account for the error between measured and predicted results.

Overall, fairly good agreement between measured and predicted temperature of apple centres, especially in the bottom, lower middle and top layers, was obtained.

Table 7.1 Input data for model validation

Boundary	Variable	Value	Note
Initial conditions	Temperature of air and solid materials (^{0}C)	19.0	
Inlet boundary 1	Fixed mass flow rate (kg·s^{-1})	1.164	
	air velocity component w (m·s^{-1})	0.9	
	air temperature T (^{0}C)	0.8	
	turbulence kinetic energy k (J·kg^{-1})	0.004050	Turbulence flow only
	dissipation rate of k ε (J·kg^{-1}·s^{-1})	0.007059	Turbulence flow only
Inlet boundary 2	Fixed mass flow rate (kg·s^{-1})	1.228	
	air velocity component w (m·s^{-1})	0.95	
	air temperature T (^{0}C)	0.8	
	turbulence kinetic energy k (J·kg^{-1})	0.004513	Turbulence flow only
	dissipation rate of k ε (J·kg^{-1}·s^{-1})	0.008301	Turbulence flow only
Carton external surfaces	Heat transfer coefficient for front surface (W·m^{-2}·K^{-1})	7.9	measured air velocity in the tunnel was 2.8 m·s^{-1}
	Heat transfer coefficient for side surfaces (W·m^{-2}·K^{-1})	13.8	
	Heat transfer coefficient for rear surface (W·m^{-2}·K^{-1})	3.6	

Table 7.3 Measured and predicted 7/8-cooling times

Position		7/8-cooling Time (min)			Error*	
Layer	Cell	Measured data	Laminar model	Turbulent model	Laminar model	Turbulent model
Bottom layer	1, 6, 10	420	365	395	13.10%	5.95%
	5, 6, 6	295	340	345	15.25%	16.95%
	1, 6, 26	675	585	580	13.33%	14.07%
	5, 6, 22	650	560	555	13.85%	14.62%
	10, 6, 26	625	620	610	0.80%	2.40%
	1, 6, 42	780	490	480	37.18%	38.46%
Lower middle layer	1, 13, 6	225	245	245	8.89%	8.89%
	5, 13, 10	330	370	370	12.12%	12.12%
	1, 13, 22	565	520	535	7.96%	5.31%
	10, 13, 22	490	545	530	11.22%	8.16%
	1, 13, 38	745	560	550	24.83%	26.17%
	5, 13, 42	760	495	480	34.87%	36.84%
Upper middle layer	1, 20, 10	155	295	295	90.32%	90.32%
	5, 20, 6	130	270	265	107.69%	103.85%
	1, 20, 26	375	425	455	13.33%	21.33%
	10, 20, 26	390	470	465	20.51%	19.23%
	1, 20, 42	610	390	405	36.07%	33.61%
	5, 20, 38	550	515	520	6.36%	5.45%
Top layer	1, 27, 6	170	270	260	58.82%	52.94%
	5, 27, 10	240	375	365	56.25%	52.08%
	1, 27, 22	395	455	475	15.19%	20.25%
	10, 27, 22	390	460	460	17.95%	17.95%
	1, 27, 38	490	510	505	4.08%	3.06%
	10, 27, 38	465	510	505	9.68%	8.60%
Average					26.24%	25.78%

* Error = |model prediction - measured data| / measured data.

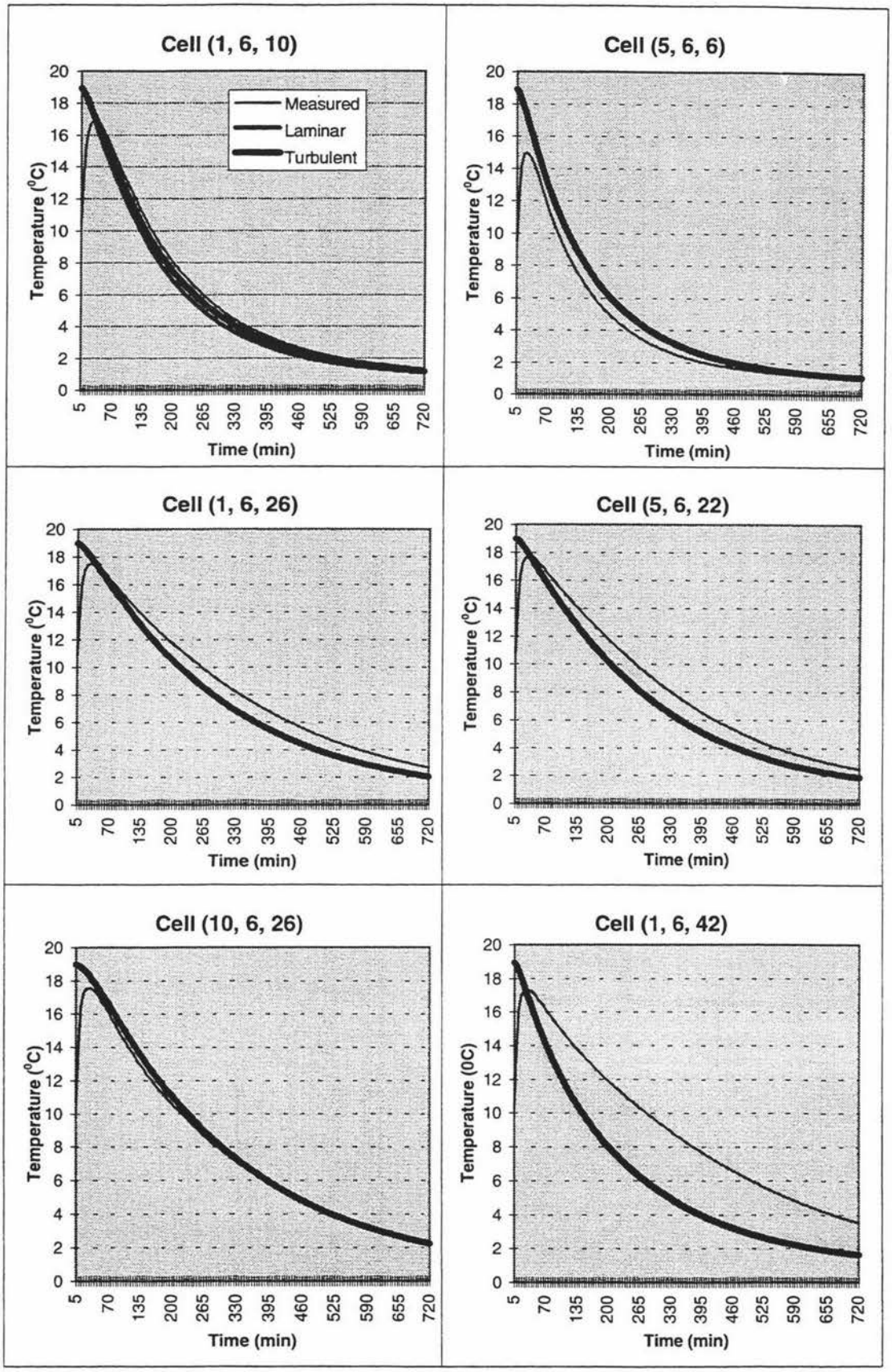

Figure 7-2a Measured and predicted apple centre temperature in the cells of bottom layer

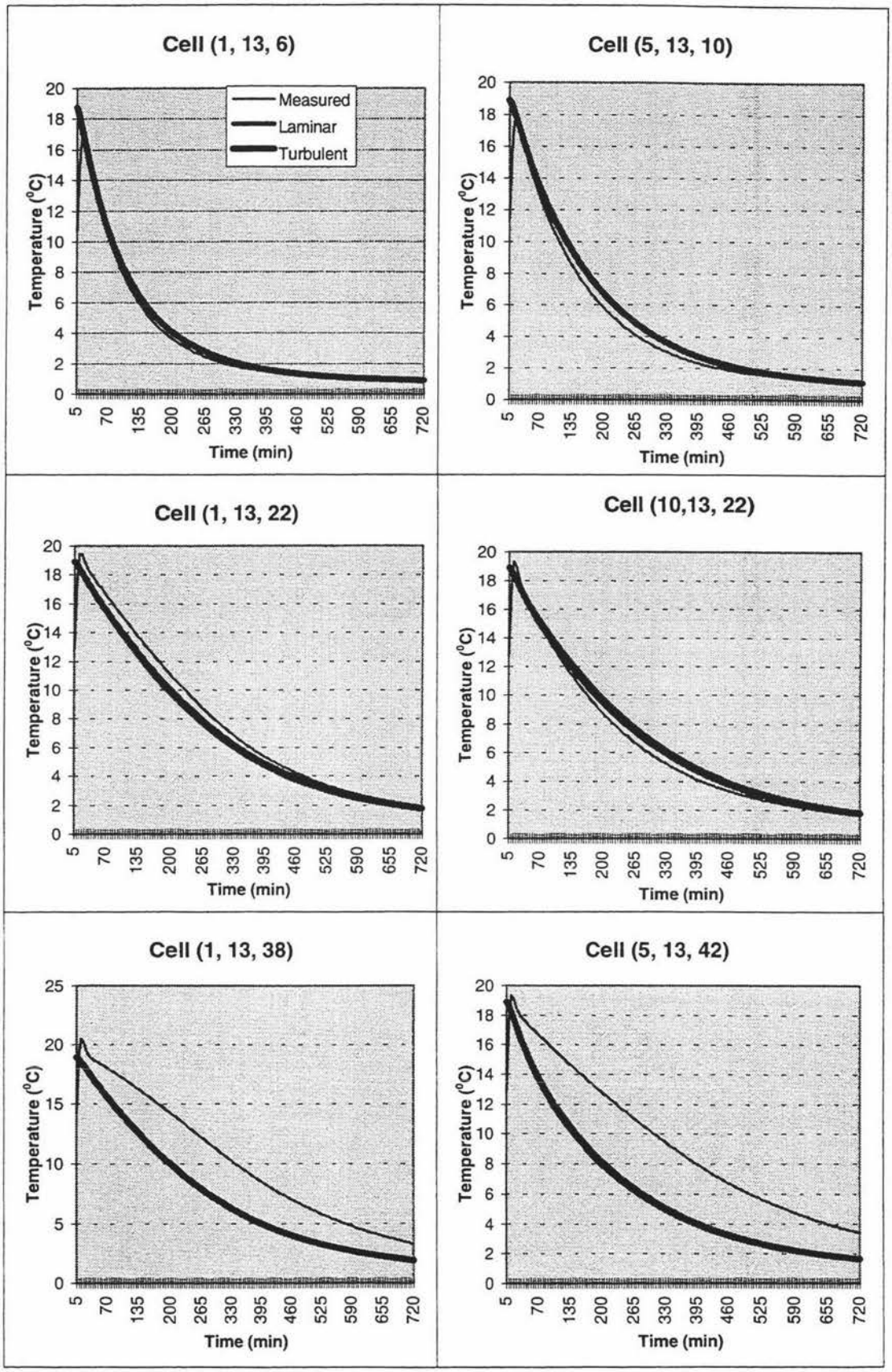

Figure 7-2b Measured and predicted apple centre temperature in the cells of lower middle layer

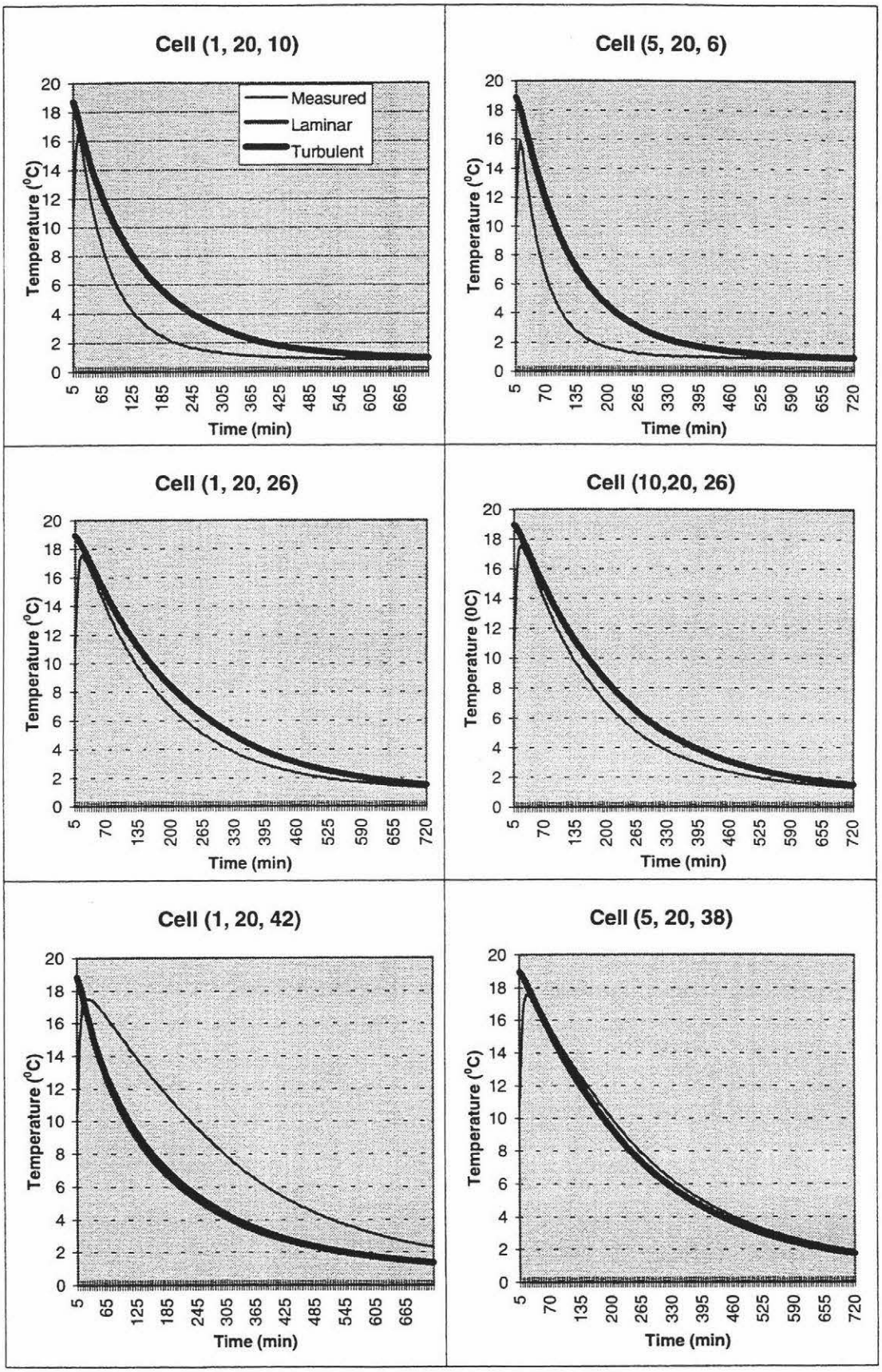

Figure 7-2c Measured and predicted apple centre temperature in the cells of upper middle layer

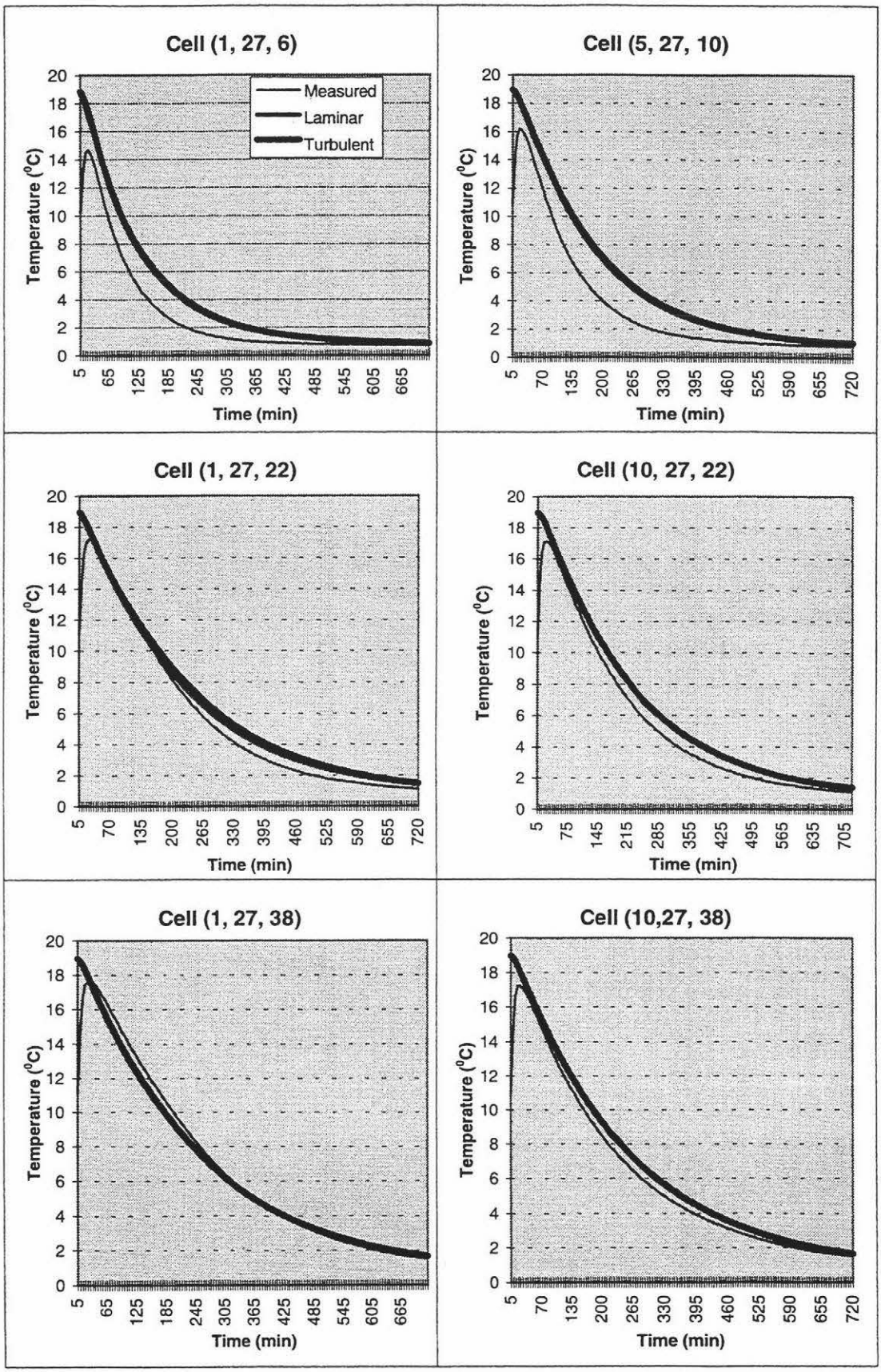

Figure 7-2d Measured and predicted apple centre temperature in the cells of top layer

CHAPTER 8: CONCLUSION

8.1 CONCLUSION

A survey of the literature showed that most of CFD-based air flow models were steady-state and were used for flow fields with relative simple geometry. Turbulence was usually modelled by standard k-ε model or its modified forms. Several commercial CFD packages have been successfully applied to solve practical flow problems. Very few models were developed to simulate the cooling of bulk produce in packages. Air flow in these models was treated by either defining an flow pathway or by solving steady-state Navier-Stokes equations.

In the model developed in this project, steady-state laminar and turbulent flows as well as unsteady-state laminar flow were formulated; the standard k-ε and Low-Reynolds-Number k-ε models were employed for turbulence modelling. After implementing the model in the PHOENICS code, the standard k-ε model was found unsuitable because the wall functions could not be applied in the calculation region. Very small relaxation factors and false time steps were used to obtain convergent solutions for steady-state laminar and turbulent flow as well as unsteady-state laminar flow. A huge amount of computing time was needed for solving unsteady-state laminar flow.

The predicted flow patterns and temperature profiles were very similar for steady-state laminar and turbulent flows under 0.5 m/s inlet velocity, though the velocities and cooling rates under turbulence conditions were slightly higher. By comparing predictions for steady-state and unsteady-state flows, effects of natural convection were considered negligible, and it was considered reasonable to adopt the programme for steady-state laminar flow instead unsteady-state laminar flow.

Comparison of measured and predicted temperature of apple centres gave fairly good agreement in most locations within the cartons, but large errors existed in the regions close to carton inlets and rear outlets. Overall, CFD modelling proved to be a useful tool for analysing the air flow patterns and heat transfer in ventilated packaging.

8.2 FURTHER RESEARCH

Further studies are needed to determine a convergent solution under higher inlet velocity, especially for steady-state and unsteady-state turbulent flows. The grids in the area near carton inlets and outlets need further refinement to represent the detailed configuration. It may be necessary to modify the fixed-pressure boundary in the carton outlets in order to make the boundary conditions closer to real situations. Sensitivity analysis is needed to estimate the effects of possible errors in input data on model accuracy.

Experiments should be conducted for further model validation using air velocity and temperature inside the carton, and for visualisation of combined flow patterns inside and outside the carton. Velocity and temperature sensors should be designed and selected so that air flows are not disturbed significantly.

Further research is also needed to determine the application of CFD modelling to simultaneous heat and water vapour transfer modelling in fresh fruit packaging.

NOMENCLATURE

A	apple surface area (m^2).
A_μ	constant ($A_\mu = 0.0165$).
A_{C1}	constant ($A_{C1} = 0.05$).
a_E	coefficient for the grid point E in the discretisation equations.
A_e	east surface area of the control volume(m^2).
a_e	parameter for the east surface.
a_H	coefficient for the grid point H in the discretisation equations.
A_h	high surface area of the control volume(m^2).
a_h	parameter for the high surface.
a_L	coefficient for the grid point L in the discretisation equations.
A_l	low surface area of the control volume(m^2).
a_l	parameter for the low surface.
a_N	coefficient for the grid point N in the discretisation equations.
A_n	north surface area of the control volume(m^2).
a_n	parameter for the north surface.
a_{nb}	a_E, a_W, a_N, a_S, a_H, a_L, a_T.
a_P	coefficient for the grid point P in the discretisation equations.
a_S	coefficient for the grid point S in the discretisation equations.
a_s	parameter for the south surface.
A_s	south surface area of the control volume(m^2).
A_t	constant ($A_t = 20.5$).
a_T	time coefficient in the discretisation equations.
a_{ue}	coefficient for u_e in the discretisation equation.
a_{unb}	coefficient for u_{nb} in the discretisation equation.
a_{uw}	coefficient for u_w in the discretisation equation.
a_{vn}	coefficient for v_n in the discretisation equation.
a_{vnb}	coefficient for v_{nb} in the discretisation equation.
a_{vs}	coefficient for v_s in the discretisation equation.
a_W	coefficient for the grid point W in the discretisation equations.
a_w	parameter for the west surface.
A_w	west surface area of the control volume(m^2).
a_{wh}	coefficient for w_h in the discretisation equation.

a_{wl}	coefficient for w_l in the discretisation equation.
a_{wnb}	coefficient for w_{nb} in the discretisation equation.
b_P	coefficient for the source term in the discretisation equations.
b_{ue}	coefficient for the source term in the discretisation equations for u.
b_{vn}	coefficient for the source term in the discretisation equations for v.
b_{wh}	coefficient for the source term in the discretisation equations for w.
C	constant.
c, d, e, f	parameters.
C_1	constant (C_1 =1.44).
C_2	constant (C_2 =1.92).
C_3	constant (C_3 = 1.44).
C_a	apple specific heat ($J \cdot kg^{-1} \cdot K^{-1}$).
C_c	carton specific heat ($J \cdot kg^{-1} \cdot K^{-1}$).
C_p	air specific heat at constant pressure ($J \cdot kg^{-1} \cdot K^{-1}$).
C_{tr}	tray specific heat ($J \cdot kg^{-1} \cdot K^{-1}$).
C_μ	constant (C_μ =0.09).
E	roughness parameter (E = 8.6).
Er	normalised whole field residual.
f_1	viscous dissipation auxiliary relation.
f_2	viscous dissipation auxiliary relation.
f_e	ratio of $(\delta x)_{e+}$ to $(\delta x)_e$.
f_h	ratio of $(\delta z)_{h+}$ to $(\delta z)_h$.
f_l	ratio of $(\delta z)_{l+}$ to $(\delta z)_l$.
f_n	ratio of $(\delta y)_{n+}$ to $(\delta y)_n$.
f_s	ratio of $(\delta y)_{s+}$ to $(\delta y)_s$.
f_w	ratio of $(\delta x)_{w+}$ to $(\delta x)_w$.
f_μ	dumping function for eddy viscosity.
g	universal gravitational constant ($m \cdot s^{-2}$).
H	characteristic inlet dimension (m).
h	heat transfer coefficient for an area of external solid surface ($W \cdot K^{-1} \cdot m^{-2}$).
h_e	surface heat transfer coefficient for carton external surface ($W \cdot K^{-1} \cdot m^{-2}$).
i	index of axes in Cartesian coordinates.

J_e	flux of ϕ per unit area due to convection and diffusion out of the east surface.
J_h	flux of ϕ per unit area due to convection and diffusion out of the high surface.
J_l	flux of ϕ per unit area due to convection and diffusion out of the low surface.
J_n	flux of ϕ per unit area due to convection and diffusion out of the north surface.
J_s	flux of ϕ per unit area due to convection and diffusion out of the south surface.
J_w	flux of ϕ per unit area due to convection and diffusion out of the west surface.
K	air thermal conductivity ($W \cdot m^{-1} \cdot K^{-1}$).
k	turbulent kinetic energy ($J \cdot kg^{-1}$).
K_a	apple thermal conductivity ($W \cdot m^{-1} \cdot K^{-1}$).
K_c	carton thermal conductivity ($W \cdot m^{-1} \cdot K^{-1}$).
K_{tr}	tray thermal conductivity ($W \cdot m^{-1} \cdot K^{-1}$).
L_s	typical turbulence length scale (m)
M	apple mass (kg).
p	air pressure ($N \cdot m^{-2}$).
$\overline{p}$	mean value of pressure ($N \cdot m^{-2}$).
p'	turbulent fluctuation of pressure ($N \cdot m^{-2}$).
p_0	relative air pressure (air pressure - hydrostatic pressure at reference position) ($N \cdot m^{-2}$).
P_e	Peclet number between grid point P and its neighbouring point E.
p_E	pressure at grid point E of the east neighbouring scalar cell ($N \cdot m^{-2}$).
P_E^*	estimated pressure at the grid point E ($N \cdot m^{-2}$).
p_{fixed}	value of air pressure at the opening ($N \cdot m^{-2}$).
P_h	Peclet number between grid point P and its neighbouring point H.
P_H	pressure at grid point E of the high neighbouring scalar cell ($N \cdot m^{-2}$).
P_H^*	estimated pressure at the grid point H ($N \cdot m^{-2}$).
p_i	value of air initial pressure ($N \cdot m^{-2}$).

P_l	Peclet number between grid point P and its neighbouring point L.
P_n	Peclet number between grid point P and its neighbouring point N.
P_N	pressure at grid point E of the east neighbouring scalar cell ($N \cdot m^{-2}$).
P_N^*	estimated pressure at the grid point N ($N \cdot m^{-2}$).
P_P	pressure at grid point P of the scalar cell ($N \cdot m^{-2}$).
P_P^*	estimated pressure at the grid point P ($N \cdot m^{-2}$).
Pr_t	turbulent Prandtl number.
P_s	Peclet number between grid point P and its neighbouring point S.
P_w	Peclet number between grid point P and its neighbouring point W.
RESREF(ϕ)	user-set reference value for ϕ.
R_k	turbulence Reynolds number.
R_t	turbulence Reynolds number.
S	source term.
$\overline{S}$	average value of S over the control volume.
S^*	S value calculated from ϕ_p^* .
S_1	assumed constant part of source term.
S_2	coefficient of ϕ_P in source term.
S_c	total surface area of the control volume (m^2).
S_E	source term of energy equations ($W \cdot m^{-3}$).
$\overline{S_E}$	time-average source term of energy equations ($W \cdot m^{-3}$).
S_k	buoyancy force production term in k equation ($J \cdot m^{-3} \cdot s^{-1}$).
S_t	Stanton number at the first grid node.
S_ε	buoyancy force production term in ε equation ($J \cdot m^{-3} \cdot s^{-2}$).
T	air temperature (K).
$\overline{T}$	time-average air temperature (K).
t	time (s).
T′	turbulent fluctuation of temperature (K).
T_a	apple temperature (K).
T_{ai}	value of apple initial temperature (K).
T_{am}	ambient temperature (K).
T_c	carton temperature (K).
T_{ci}	value of carton initial temperature (K).

T_e temperature of external air flow (K).

T_i value of air initial temperature (K).

T_{in} value of air temperature at the opening (K).

T_{ref} air reference temperature (K).

$\overline{T}_{ref}$ reference time-average air temperature (K).

T_{tr} tray temperature (K).

T_{tri} value of tray initial temperature (K).

$T_{x=0}$ surface temperature (K).

$\mathbf{u}$ air velocity vector ($m \cdot s^{-1}$).

u_* friction velocity ($m \cdot s^{-1}$).

u_e x direction velocity component at centre point of east surface of scalar cell ($m \cdot s^{-1}$).

u_e^* x direction velocity component u_e calculated based on the estimated pressure field ($m \cdot s^{-1}$).

u_i component of velocity in x_i direction ($m \cdot s^{-1}$).

$\overline{u}_i$ mean values of air velocity component u_i ($m \cdot s^{-1}$).

u_i' turbulent fluctuation of air velocity component u_i($m \cdot s^{-1}$).

$u_{i\text{-}in}$ value of air velocity at the opening ($m \cdot s^{-1}$).

u_j component of velocity in x_j direction ($m \cdot s^{-1}$).

u_j' turbulent fluctuation of velocity components u_j ($m \cdot s^{-1}$).

u_{nb} x direction velocity components at centre points of east surfaces of neighbouring scalar cells ($m \cdot s^{-1}$).

u_{nb}^* x direction velocity components u_{nb} calculated based on the estimated pressure field ($m \cdot s^{-1}$).

u_r resultant velocity parallel to the surface at the first grid node ($m \cdot s^{-1}$).

u_R resultant velocity parallel to the wall ($m \cdot s^{-1}$).

u_w x direction velocity component at centre point of west surface of scalar cell ($m \cdot s^{-1}$).

u_w^* x direction velocity component u_w calculated based on the estimated pressure field ($m \cdot s^{-1}$).

V volume of the control volume (m^3).

V_a apple volume (m^3).

v_n y direction velocity component at centre point of north surface of scalar cell ($m \cdot s^{-1}$).

v_n^* y direction velocity component v_n calculated based on the estimated pressure field ($m \cdot s^{-1}$).

v_{nb} y direction velocity components at centre points of north surfaces of neighbouring scalar cells ($m \cdot s^{-1}$).

v_{nb}^* y direction velocity components v_{nb} calculated based on the estimated pressure field ($m \cdot s^{-1}$).

V_P cell volume (m^3).

V_s typical turbulence velocity scale ($m \cdot s^{-1}$).

v_s y direction velocity component at centre point of south surface of scalar cell ($m \cdot s^{-1}$).

v_s^* y direction velocity component v_s calculated based on the estimated pressure field ($m \cdot s^{-1}$).

w_h z direction velocity component at centre point of high surface of scalar cell ($m \cdot s^{-1}$).

w_h^* z direction velocity component w_h calculated based on the estimated pressure field ($m \cdot s^{-1}$).

w_l z direction velocity component at centre point of low surface of scalar cell ($m \cdot s^{-1}$).

w_l^* z direction velocity component w_l calculated based on the estimated pressure field ($m \cdot s^{-1}$).

w_{nb} z direction velocity components at centre points of high surfaces of neighbouring scalar cells ($m \cdot s^{-1}$).

w_{nb}^* z direction velocity components w_{nb} calculated based on the estimated pressure field ($m \cdot s^{-1}$).

X_i components of body force per unit air volume along x_i direction ($N \cdot m^{-3}$).

x_i spatial position in Cartesian coordinates (m).

x_j spatial position in Cartesian coordinates (m).

y^+ dimensionless distance from the wall.

y_p generalised normal distance from a solid boundary (m).

α	relaxation factor ($0 < \alpha \leq 1$).
β	air thermal expansion coefficient (K^{-1}).
ε	rate of dissipation of the turbulent energy ($J \cdot kg^{-1} \cdot s^{-1}$).
ε_p	residual of ϕ in the cell P.
ϕ	dependent variable.
ϕ^*	value of ϕ resulting from the current iteration.
ϕ_e	value of variable ϕ in the east surface.
ϕ_h	value of variable ϕ in the high surface.
ϕ_l	value of variable ϕ in the low surface.
ϕ_n	value of variable ϕ in the north surface.
ϕ_{new}	new in-store value of ϕ.
ϕ_{old}	current in-store value of ϕ.
ϕ_p	cell value of ϕ to be computed.
ϕ_p^*	guess value or the previous iteration value of ϕ_P.
ϕ_p^0	value of ϕ_P at previous time step.
ϕ_s	value of variable ϕ in the south surface.
ϕ_w	value of variable ϕ in the west surface.
Γ	diffusion coefficient.
Γ_E	Γ value at the grid point E.
Γ_e	value of Γ in the east surface.
Γ_h	value of Γ in the high surface.
Γ_l	value of Γ in the low surface.
Γ_n	value of Γ in the north surface.
Γ_P	Γ value at the grid point P.
Γ_s	value of Γ in the south surface.
Γ_t	turbulent diffusion coefficient ($W \cdot m^{-1} \cdot K^{-1}$).
Γ_w	value of Γ in the west surface.
κ	van Karman's constant ($\kappa = 0.41$).
σ_ε	constant ($\sigma_\varepsilon = 1.3$).
σ_k	constant ($\sigma_k = 1.0$).
ρ	air density ($kg \cdot m^{-3}$).
ρ_a	apple density ($kg \cdot m^{-3}$).

ρ_c carton density ($kg \cdot m^{-3}$).

ρ_{ref} air density at reference positions ($kg \cdot m^{-3}$).

ρ_{tr} tray density ($kg \cdot m^{-3}$).

μ air dynamic viscosity ($N \cdot s \cdot m^{-2}$).

μ_t turbulent eddy viscosity ($N \cdot s \cdot m^{-2}$).

δ_{ij} Kronecker delta (δ_{ij} =1 if i=j, and 0 otherwise).

τ_w wall shear stress ($N \cdot m^{-2}$).

Δp_E pressure correction at the neighbouring grid point E ($N \cdot m^{-2}$).

Δp_H pressure correction at the neighbouring grid point N ($N \cdot m^{-2}$).

Δp_L pressure correction at the neighbouring grid point L ($N \cdot m^{-2}$).

Δp_N pressure correction at the neighbouring grid point N ($N \cdot m^{-2}$).

Δp_P pressure correction at grid point P ($N \cdot m^{-2}$).

Δp_S pressure correction at the neighbouring grid point S ($N \cdot m^{-2}$).

Δp_W pressure correction at the neighbouring grid point W ($N \cdot m^{-2}$).

Δt time interval (s).

Δt_f false time step (s).

Δu_e velocity correction for u_e ($m \cdot s^{-1}$).

Δv_n velocity correction for v_n ($m \cdot s^{-1}$).

Δw_h velocity correction for w_h ($m \cdot s^{-1}$).

$(\delta x)_e$ displacement between grid-point P and its neighbouring point E (m).

$(\delta x)_{e+}$ displacement between the grid point P and the east surface (m).

$(\delta x)_w$ displacement between grid point P and its neighbouring point W(m).

$(\delta x)_{w+}$ displacement between the grid point P and the west surface (m).

$(\delta y)_n$ displacement between grid point P and its neighbouring point N (m).

$(\delta y)_{n+}$ displacement between the grid point P and the north surface (m).

$(\delta y)_s$ displacement between grid point P and its neighbouring point S (m).

$(\delta y)_{s+}$ displacement between the grid point P and the south surface (m).

$(\delta z)_h$ displacement between grid point P and its neighbouring point H (m).

$(\delta z)_{h+}$ displacement between the grid point P and the high surface (m).

$(\delta z)_l$ displacement between grid point P and its neighbouring point L (m).

$(\delta z)_{l+}$ displacement between the grid point P and the low surface (m).

REFERENCES

ASHRAE. (1993). *ASHRAE handbook - fundamentals*. American Society of Refrigeration and Air Conditioning Engineers Publishers, Atlanta Ga.

ASHRAE. (1994). *ASHRAE handbook - Refrigeration*. American Society of Refrigeration and Air Conditioning Engineers Publishers, Atlanta Ga.

Amos, N.D. (1995). *Mathematical modelling of heat transfer and water vapour transport in apple coolstores,* PhD Thesis, Massey University, Palmerston North, New Zealand.

Ansari, F.A., Charan, V., & Varma, H.K. (1984). Heat and mass transfer analysis in air-cooling of spherical food products. *International Journal of Refrigeration*, **7:** 194-197.

Awbi, H.B. (1989). Application of computational fluid dynamics in room ventilation, *Building and Environment*, **24:** 73-84.

Baird, C.D., Chau, K.V., Gaffney, J.J. (1985). Engineering/economic model for evaluating forced-air cooling systems for fruit and vegetables, *Refrig. Sci. & Technol.*, **1985-5:** 259-266.

Baird, C.D. & Gaffney, J.J. (1976). A numerical procedure for calculating heat transfer in bulk loads of fruits and vegetables. *ASHRAE Transactions,* **82:** 525-540.

Bazan, T., Chau, K.V. & Baird, C.D. (1989). Heat transfer simulation of the bulk cooling of fruits, ASAE Paper No. 89559.

Bradshaw, P. (1970). *Experimental Fluid Mechanics (2nd Edition).* Pergaman Press, Inc., Oxford.

Brook, D.B. (1969). Computing air pressure and velocity distribution when air flows through a porous medium and nonlinear velocity-pressure realationships exist. *Transactions of the ASAE*, **12:** 118-120.

CHAM. (1995). *PHOENICS On-line Information System. PHOENICS 2.2.1,* CHAM Ltd. London.

Chapman, J.E., Vance Morey, R., Cloud, H.A., & J.L., Nieber. (1989). Airflow patterns in flat storage aeration systems. *Transactions of the ASAE,* **32:** 1368-1376.

Chau, K.V. & Gaffney, J.J. (1990). A finite-difference model for heat and mass transfer in products with internal heat generation and transpiration. *Transactions of the ASAE*, **33:** 484-487.

Chen, Q., Moser, A., & Huber, A. (1990). Prediction of bounce, turbulent flow by a low-Reynolds-number k-ε model, *ASHRAE Transactions*, **96:** 564-573.

Cheremisinoff, N.P & Cheremissionoff, P.N. (1988). *Flow Measurement for Engineers and Scientists*. Marcel Dekker, Inc., New York.

Choi, H.L., Albright, L.D., Timmons, M.B., & Warhaft, Z. (1988). An application of the K-Epsilon turbulence model to predict air distibution in a slot-ventilated enclosure. *Transactions of the ASAE*, **31(6):** 1804-1814.

Choi, H.L., Albright, L.D., Timmons, M.B. (1990). An application of the K-ε turbulence model to predict how a rectangular obstacle in a slot-ventilated enclosure affects air flow. *Transactions of the ASAE*, **33:** 274-281.

Clary, B.L., Nelson, G.L., & Smith, R.E. (1968). Heat transfer from hams during freezing by low temperature air. *Transactions of ASAE,* **11:** 496-499.

Clary, B.L., Nelson, G.L., & Smith, R.E. (1971). Application of geometry analysis technique in determining the heat transfer rate from biological materials. *Transactions of ASAE,* **14:** 586-589.

Clayton, M., Amos, N.D., Banks, N.H., and Morton, R.H. (1995). Estimation of apple fruit area. *New Zealand Journal of Crop and Horticultural Science*. **23**: 345-349.

Cleland, A.C. (1983). Simulation of industrial refrigeration plants under variable load conditions, *Int. J. Refrig.*, **6:** 11-19.

Cleland, A.C. (1985a). Experimental verification of a mathematical model for simulation of industrial refrigeration plants, *Int. J. Refrig.*, **8:** 275-282.

Cleland, A.C. (1985b). RADS- a computer package for refrigeration analysis, design and simulation, *Int. J. Refrig.*, **8:** 372-374.

Cleland, A.C. (1990). *Food Refrigeration Processes - Analysis, Design and Simulation,* Elsevier Science Publishers, London.

Cleland, D.J., Boyd, N.S. & Cleland, A.C. (1982). A model for fish freezing and storage aboard small New Zealand fishing vessels, *Refrig. Sci. & Technol.*, **1982-1:** 147-156.

Cleland, D.J. & Cleland, A.C. (1989). Appropriate level of model complexity in dynamic simulation of refrigeration systems, *Refrig. Sci. & Technol.*, **1989-1:** 261-268.

Cleland, A.C., & Earle, R.L. (1982). A simple method for prediction of heating and cooling rates in solids of various shapes. *International Journal of Refrigeration*. **5:** 98-106.

Collins, M.W. & Ciofalo, M. (1991). Computational fluid dynamics and its application to transport processes, Journal of Chemical Technology and Biotechnology, **52**: 5-47.

Comini, G., Cortella, G., Saro, O. (1995). Finite element analysis of coupled conduction and convection in refrigerated transport. *International Journal of Refrigeration*, **18:** 123-131.

Dossat, R.J. (1980). *Principles of refrigeration.* 2 ed. Wiley, New York.

The Enterprise New Zealand Trust. (1993). *The New Zealand Apple and Pear Industry.* Wellington, New Zealand.

ENZA New Zealand (International). (1996). *Palletised Packaging System Information Pack.* Wellington, New Zealand.

Feustel, H.E. & Dieris, J. (1992). A survey of airflow models for multizone structures, *Energy and Buildings,* **18:** 79-100.

Fingerson, L.M. & Freymuth, P. (1983). Thermal anemometer. In *Fluid Mechanics measurement* (edited by Goldstein, R.J.), Hemisphere Publishing Corporation, Washington.

Fletcher, C.A. (1988a). *Computational Techniques for Fluid Dynamics. Volume I, Fundamental and General Techniques.* Springer-Verlag Berlin Heidelberg, New York.

Fletcher, C.A. (1988b). *Computational Techniques for Fluid Dynamics. Volume II, Specific Techniques for Different Flow Categories.* Springer-Verlag Berlin Heidelberg, New York.

Goldstein, R.J. (1983). Optical systems for flow measurement: shadowgraph, schlieren, and interferometric techniques. In *Fluid Mechanics measurement* (edited by Goldstein, R.J.), Hemisphere Publishing Corporation, Washington.

Gosman, A.D., Nielsen, P.V., Restivo, A., & Whitelaw, J.H. (1980). The flow properties of rooms with small ventilation openings. *Journal of Fluid Engineering,* **102**: 316-323.

Green, S.R. (1992). Modelling turbulent air flow in a stand of widely-spaced trees. *The PHOENICS Journal,* **5:** 294-312.

Haghighi, K. & Sergerlind, L.J. (1988). Modelling simultaneous heat and mass transfer in an isotropic sphere-a finite element approach. *Transaction of ASAE*, **31:** 629-637.

Harper, J.M. & Wanninger, L.A. (1969). Process modelling and optimisation 1. experimental design, *Food Technology*, **23**: 1153-1155.

Harper, J.M. & Wanninger, L.A. (1970a). Process modelling and optimisation 2. modelling, *Food Technology*, **24**: 267-268.

Harper, J.M. & Wanninger, L.A. (1970b). Process modelling and optimisation 3. optimisation, *Food Technology*, **24**: 590-595.

Hayakawa, K. (1978). Computerised simulation for heat transfer and moisture loss from an idealised fresh produce. *Transactions of ASAE,* **21:** 1015-1024.

Hoff, S.J. (1995). A simplified turbulence model for describing airflow in ceiling slot-ventilated enclosures. *Transactions of ASAE*, **38:** 1853-1862.

Hoff, S.J., Janni, K.A., & Jacobson, L.D. (1992). Three dimensional buoyant turbulent flows in a scaled model, slot-ventilated livestock confinement facility. *Transactions of ASAE*, **35:** 671-686.

Hoff, S.J., Janni, K.A., & Jacobson, L.D. (1995). Evaluating the performance of a low Reynolds number turbulence model for describing mixed-flow airspace and temperature distributions. *Transactions of ASAE*, **38:** 1533-1541.

Hoff, S.J., & Bundy, D.S. (1996). Comparison of contaminant dispersion modelling approaches for swine housing. *Transactions of ASAE*, **39:** 1151-1157.

James, R.W. (1980). Refrigeration and air conditioning systems, *Modelling of Dynamic Systems,* **Vol.1**, pp 62-69, Peter Peregrinus Ltd., Stevenage, UK.

Jiang, H., Thompson, D.R., & Morey, R.V. (1987). Finite element model of temperature distribution in broccoli stalks during forced-air precooling. *Transactions of ASAE*, **30:** 1473-1477.

Jones, W.P., & Launder, B.E. (1972). The prediction of laminarization with a 2-equation model of turbulence, *International Journal of Heat and Mass Transfer*, **15:** 301-314.

Jones, P.J. & Whittle, G.E. (1992). Computational fluid dynamics for building air flow prediction-current status and capabilities. *Building and Environment*, **27:** 321-338.

Kays, S.J. (1993). *Postharvest physiology of perishable plant products.* Van Norstrand Reinhold. New York.

Khelifi, M., Robert, J. L., & Lague, C. (1996a). Modelling airflow inside and around hoods used for pneumatic control of pest insects. Part I: development of a finite element model. *Canadian Agricultural Engineering*, **38:** 265-271.

Khelifi, M., Robert, J. L., & Lague, C. (1996b). Modelling airflow inside and around hoods used for pneumatic control of pest insects. Part II: application and validation of the model. *Canadian Agricultural Engineering*, **38 :** 272-281.

Kieviet, F.G., Van Raaij, J., De Moor, P.P.E., & Kerkhof, P.J.A.M. (1997). Measurement and modelling of the air flow patterns in a pilot-plant spray dryer. *Transaction of Institution of Chemical Engineers,* **75(A):** 321-329.

Kotake. S, Hijikata. K, & Fusegi, T. (1993). *Numerical Simulation of Heat Transfer and Fluid Flow on a Personal Computer.* ELSEVIER Science Publishers. Netherlands.

Kothandranaman C.P. & Subramanyan, S. (1977). *Heat and Mass Transfer Data Book.* John Wiley & Sons. New York.

Lam, C.K.G.,& Bremhorst, K. (1981). A modified form of the k-ε model for predicting wall turbulence. *Transaction of the ASME, Journal of Fluids Engineering*, **103:** 456-460.

Launder, B.E. & Spalding, D.B. (1972). *Mathematical Models of Turbulence*. Academic Press. London.

Launder, B.E. & Spalding, D.B. (1974). The numerical computation of turbulent flows. *Computational Methods in Applied Mechanics and Engineering*, **3**: 269-289.

Leschziner, M.A. (1990). Modelling engineering flows with Reynolds stress turbulence closure. *Journal of Wind Engineering and Industrial Aerodynamics*, **35**: 21-47

Levine, L. (1997). Food process development and scale up using modelling and simulation. *Chemistry and Industry*, **5**: 346-349.

Liao, C.M., & Feddes, J.J.R. (1992). A lumped-parameter model for describing the airborne dust concentration in a ventilated airspace. *Transaction of ASAE*, **35:** 1973-1978.

Lin, Z. (1994). *Prediction of Chilling Times of Foods,* PhD Thesis, Massey University, Palmerston North, New Zealand.

Lin, Z., Cleland, A.C., Cleland, D.J., & Serrallach, G.F. (1996a). A simple method for prediction of chilling times for objects of two-dimensional irregular shapes. *International Journal of Refrigeration,* **19:** 95-106.

Lin, Z., Cleland, A.C., Cleland, D.J., & Serrallach, G.F. (1996b). A simple method for prediction of chilling times for objects of three-dimensional irregular shapes. *International Journal of Refrigeration,* **19:** 107-114.

Liu, Q., Hoff, S.J., Maxwell, G.M., & Bundy, D.S. (1996). Comparison of three k-ε turbulence models for predicting ventilated air jets. *Transactions of ASAE*, **39:** 689-698.

Lovatt,S.J. (1992). *A Dynamic Modelling Methodology for the Simulation of Industrial Refrigeration Systems,* PhD Thesis, Massey University, Palmerston North, New Zealand.

Maghirang, R.G., & Manbeck, H.B. (1993). Modelling particle transport in slot-inlet ventilated airspaces. *Transactions of the ASAE*, **36:** 1449-1459.

Maghirang, R.G., Manbeck, H.B., Puri, V.M. (1994). Numerical simulation of particle transport in slot-inlet ventilated airspaces. *Transactions of the ASAE*, **37:** 1607-1612.

Marchant, J.A. (1976). The prediction of air flows in crop drying systems by finite element method. *Journal of Agricultural Engineering Research*, **21:** 417-429.

Mariotti, M., Rech, G., & Romagnoni, P. (1995). Numerical study of air distribution in a refrigerated room. *19th International Congress of Refrigeration 1995*, **2:** 98-105.

Markatos, N.C., & Malin, M.R. (1982). Mathematical modelling of buoyancy-induced smoke flow in enclosures. *International Journal of Heat and Mass Transfer*, **25:** 63-75.

Markatos, N.C., & Pericleous, K.A. (1984). Laminar and turbulent natural convection in an enclosed cavity. *International Journal of Heat and Mass Transfer*, **27:** 755-722.

Mueller, T.J. (1983). Recent developments in smoke flow visualisation. *The Third International Symposium on Flow Visualisation*, University of Michagan, Michigan, USA.

NZAPMB (New Zealand Apple and Pear Marketing Board). (1996). *1996 Annual Report*. Wellington, New Zealand.

Opara, L.U. & Zou, Q. (1998). Computational fluid dynamics: applications and potentials in agricultural and food engineering research. Paper written for presentation at congress on Agricultural Engineering, *AgEng Oslo 98*, Oslo, Norway, 24-27 August.

Pala, M. & Devers, Y.O. (1988). Computer simulated model for power consumption and weight loss in a cold store, *Refrig. Sci. & Technol.*, **1988-1:** 233-241.

Pan, J.C. & Bhowmik, S.R. (1991). The finite element analysis of transient heat transfer in fresh tomatoes during cooling. *Transactions of ASAE*, **34:** 972-976.

Parson, D.J. (1991). Modelling gas flow in a silage clamp after opening. Journal of Agricultural Engineering Research, **50:** 209-218.

Patankar, S.V. (1980). *Numerical Heat Transfer and Fluid Flow*. Hemisphere Publishing Co. Washington.

Patankar, S.V., & Spalding, D.B. (1972). A caculation procedure for heat, mass and momentum transfer in three-dimensional parabolic flows, *International Journal of Heat and Mass Transfer,* **15:** 1787-1806.

Peyret, R. & Taylor, T.D. (1983). *Computational Methods for Fluid Flow*. Springer-Verlag New York Inc. New York.

Reinartz, A., & Renz, U. (1984). Calculations of the temperature and flow field in a room ventilated by a radial air distributor, International Journal of Refrigeration, **7:** 308-312.

Reynolds, A.M. (1997). A model for predicting airborne dust concentrations within a ventilated airspace. *Journal of Agricultural Engineering Research*, **66:** 103-109.

Reynoso, R.O. & de Michelis, A. (1988). Simulation of batch cryogenic freezers, *Int. J. Refrig.*, **11:** 6-10.

Rodi, W. (1979*). Turbulence Models and Their Application in Hydraulics - A State of the Art Review.* Internation Association for Hydraulic Research, Delft, the Netherlands.

Romero, R.A & Chau, K.V. (1987). A mathematical simulation for transpiration from fruits and vegetables in bulk storage. ASAE Paper No. 87-6007.

Scott, G. & Richardson, P. (1997). The application of computational fluid dynamics in the food industry. *Trends in Food Science & Technology*, **8:** 119-124.

Smith, E.A. (1982). Three-dimensional analysis of air velocity and pressure in beds of grain and hay. *Journal of Agricultural Engineering Research*, 27: 101-117.

Smith, R.E, & Nelson, G.L. (1969). Transient heat transfer in solids: theory versus experimental. *Transactions of ASAE*, **12:** 833-836, 844.

Smith, R.E., Nelson, G.L., & Henrichson, R.L. (1967). Analysis on transient heat transfer from anomalous shapes. *Transactions of ASAE,* **10:** 236-245.

Smith, R.E., Nelson, G.L., & Henrichson, R.L. (1968). Application of geometry analysis of anomalous shapes to problems in transient heat transfer. *Transactions of ASAE,* **11:** 296-302.

Somerscales, E.F.C. (1981). Tracer methods. In *Measurement of Velocity. Methods of Experimental Physics, Vol. 18A*. Academic Press, Inc., New York.

Szczechowiak, E. & Rainczak, J. (1987). The cooling chamber and the air-cooler operation in unsteady states, *Proc. 17th Int. Congr. Refrig.*, **2:** 864-869.

Tennekes, H. & Lumley, J.L. (1973). *A First Course in Turbulence*. The MIT Press, Cambridge, USA.

Timmons, M.B., Albright, L.D., Furry, R.B., & Torrance, K.E. (1980). Experimental and numerical study of air movement in slot-ventilated enclosures. *ASHRAE Transactions*, **86:** 221-240.

Touber,S. (1984). Principles and methods for mathematical modelling the steady-state and dynamics behaviour of refrigeration components and installations, *Refrig. Sci. & Technol.*, **1984-2**: 163-175.

Van Gerwen, R.J.M., Van der Sluis, S.M., & Van Oort, H. (1991). Computer modelling of carcass chilling models, *Proc. 18th Int. Congr. Refrig.*, **4:** 1893-1897.

Wang, H. & Touber, S. (1990). Distributed dynamic modelling of a refrigerated room, *Int. J. Refrig.*, **13:** 214-222.

Wang, H. & Touber, S. (1991). Distributed and non-steady-state modelling of an air cooler, *Int. J. Refrig.*, **14:** 98-111.

Wells, C.M. (1992). *Modelling the Greenhouse Environment and the Growth of Cucumbers*, PhD Thesis, Massey University, Palmerston North, New Zealand.

Weiner, K.L., & Parkin, C.S. (1993). The use of computational fluid dymanic code for modelling spray from a mistblower. *Journal of Agricultural Engineering Research*, **55:** 313-324.

Woods, J.L. (1990). Moisture loss from fruits and vegetables. *Postharvest News and Information* **1:** 159-199.

Worley, M.S., & Manbeck, H.B. (1995). Modelling particle transport and air flow in ceiling inlet ventilation systems. *Transactions of the ASAE*, **38:** 231-239.

YUAN, S.W. (1967). *Foundations of Fluid Mechanics*. Prentice-Hall International, Inc. London.